Emergent Disorder: Nano-Domain Formation Near the First-Order Mott-Hubbard Transition

Dissertation
zur
Erlangung des Doktorgrades (Dr. rer. nat.)
der
Mathematisch-Naturwissenschaftlichen Fakultät
der
Rheinischen Friedrich-Wilhelms-Universität Bonn

vorgelegt von
Qinyong Liu
aus
Henan

Bonn 2012

Angefertigt mit Genehmigung der Mathematisch-Naturwissenschaftlichen Fakultät der Rheinischen Friedrich-Wilhelms-Universität Bonn

1. Gutachter:	Prof. Dr. J. Kroha
2. Gutachter:	Prof. Dr. R. Flume
Tag der Promotion:	17.07.2012
Tag der Abgabe:	23.04.2012
Erscheinungsjahr:	2012

Dieser Forschungsbericht wurde als Dissertation von der Mathematisch-Naturwissenschaftlichen Fakultät der Universität Bonn angenommen und ist auf der ULB Bonn `http://hss.ulb.uni-bonn.de/diss_online` elektronisch publiziert.

Contents

Chapter 1.

Introduction to the Metal-Insulator Transition

After quantum mechanics was introduced to explain the difference of metals and insulators by Wilson (1931), scientists began to notice that some materials cannot be explained by this model. For example, NiO is an insulator, even though Wilson's theory would predict a metallic behavior because the out most electrons of Ni^{2+} fill only partly of the d-band (de Boer and Verwey, 1937). Mott (1949) compared the Heisenberg approximation and the Bloch methods in metal theory and proposed a model which contains a crystalline array of atoms to explain the metal-insulator transition. He found that this model changes from an itinerant system to a localized system abruptly when $n^{1/3}a = 0.2$ (Mott, 1968), where n is the number of electron density and a is the lattice constant. In a review paper, Mott (1961) explained that, as the Coulomb interaction between charge carriers increases at some critical point, the system will undergo a metal-insulator phase transition (MIT), which is a first-order phase transition.

Another important step was made by Hubbard later (1963; 1964a; 1964b). He considered a model which contains both the hopping t and the repulsive onsite interaction U between electrons on the same atom. This model has an anti-ferromagnetic ground state at zero temperature and the interaction U splits the band into two bands: the lower Hubbard band and the upper Hubbard band. When this system is exactly half-filled, the lower Hubbard band is full while the upper Hubbard band is empty, and the ground state is the anti-ferromagnetic insulator. Hubbard concluded that the MIT will happen when U_c is close to the bandwidth. Although his conclusion sounds reasonable, his calculation which is based on the large U approximation, does not yield the correct result in the metallic phase, because the Fermi-liquid quasiparticles are absent (Edwards and Hewson, 1968). Another approach was made by Brinkman and Rice (1970) by applying Gutzwiller's method (Gutzwiller, 1965) to the Hubbard model. They obtained a reasonable Fermi liquid description, but no insulating solution. The question about how to resolve both the metallic and the insulating phase of the Hubbard model is difficult, because none of the perturbative methods can be used to solve this problem. This reflects the competing physical mechanisms of the Hubbard model: the on-site interaction U tends to make the electrons localized and the hopping t tends to make the electrons itinerant.

This problem troubled physicists for a long time until Metzner (1989) found that the self-energy diagrams in infinite-d (d is the dimensionality) Hubbard model can be strongly simplified, and the self-energy becomes independent of momentum in infinite dimensions. Utilizing this feature, the Dynamical Mean Field Theory (DMFT) was developed. In DMFT, the full lattice of atoms is replaced by an impurity interacting with a bath of electrons. This approximation captures the dynamics of the electrons on a central atom as it fluctuates among different configurations: unoccupied, singly occupied, and doubly occupied. Müller-Hartmann (1989c,a,b) proved that the momentum conservation can be disregarded when the number of internal lines in the free energy diagram is greater than twice the number of relevant vertices, which is in accordance with Metzner and Vollhardt. Following Müller-Hartmann's work, Brandt and Mielsch (1989, 1990, 1991) derived self-consistent functional equations for the Falicov-Kimball model and solved them. This tells us that *a lattice model can be mapped onto an impurity model within the DMFT theory*. One year later, Georges and Kotliar (1992) made a big progress by showing that the an infinite-d Hubbard model can be mapped to an Anderson impurity model (AIM) (Anderson, 1961) subject to a self-consistent bath with the help of the functional equations. This is the key point of dynamical mean-field theory (DMFT). Rozenberg et al. (1992) used Quantum Monte Carlo (QMC) (Hirsch and Fye, 1986) as an impurity solver. They showed that the infinite-d Hubbard model at half-filling undergoes a MIT between the Fermi-liquid and the insulating regime as U/t increases at finite temperature. They also demonstrated that the Mott-Hubbard MIT at finite temperature is a first order phase transition, and they could produce the phase diagram of the fully frustrated Hubbard model at half-filling(Rozenberg et al., 1994b).

Since the Mott-Hubbard MIT at finite temperature is a first order phase transition, and, as it is shown by Rozenberg et al. (1994b), there is a phase coexistence region in the phase diagram, see Fig. 1.3, we believe that in this coexistence region, insulator domains can be thermally excited from the metallic phase and metallic domains can also be thermally excited from the insulating phase. At high temperatures, this phenomenon becomes fundamental because these thermal excitations occur more often. This domain structure was already observed by Wu et al. (2006) in VO_2 nanobeams. One would expect that the domain structure changes the transport property of the system, because on one side, when the domains are very small, the electron wavelength can have the same order of magnitude as the domain size, which makes the electron and domain scattering very important; on the other side, as the domain grows, the percolation phenomena becomes important. We would like to investigate how the domain phenomena affects the conductance of a system, and this results may be used to explain the linear resistivity in High-T_c superconductors when $T > T_c$.

1.1. Hubbard Model and Its Primitive Solutions

The Hubbard model describes a system which contains both the electrons hopping between sites and the electron-electron Coulomb interaction on each lattice site. The

hopping term is easily formulated in second quantization as:

$$T = \sum_{i,j,\sigma} t_{ij}\, c^{\dagger}_{i,\sigma} c_{j,\sigma}, \tag{1.1}$$

in which $t_{ij} = N^{-1}\sum_k e^{i\mathbf{k}\cdot(\mathbf{R_i}-\mathbf{R_j})}E_k$ is the energy to pay when an electron hops from one site j to another site i. The nearest neighbor hopping term $t_{ij} = t$ when $|\mathbf{R_i} - \mathbf{R_j}| = a$, where a is the lattice constant. But the calculation of the Coulomb interaction

$$V[(i,\sigma);(j,\sigma')|(k,\sigma');(l,\sigma)] = e^2 \int dr\, dr' \frac{\Phi^*_{i,\sigma}(r)\Phi^*_{j,\sigma'}(r')\Phi_{k,\sigma'}(r')\Phi_{l,\sigma}(r)}{|r-r'|} \tag{1.2}$$

is not easy, because this interaction depends on the overlap of the electron wave functions. It can be simplified if we keep only the important term in this interaction. Hubbard (1963, 1964b) used weakly overlapping hydrogen wave functions to show that the on-site repulsion $U = V((i,\sigma);(i,\sigma')|(i,\sigma');(i,\sigma))$ dominates in this interaction:

$$\begin{aligned}
V((i,\sigma);(i,\sigma')|(i,\sigma');(i,\sigma)) &\simeq 20\mathrm{eV},\\
V((i,\sigma);(i+\delta,\sigma')|(i+\delta,\sigma');(i,\sigma)) &\simeq 6\mathrm{eV},\\
V((i,\sigma);(i,\sigma')|(i+\delta,\sigma');(i,\sigma)) &\simeq 0.5\mathrm{eV},\\
V((i,\sigma);(i,\sigma')|(i+\delta,\sigma');(i+\delta,\sigma)) &\simeq 0.025\mathrm{eV}.
\end{aligned}$$

If we keep the most important term $V(i;i|i;i)$, we have formulated the Hubbard model

$$H = \sum_{i,j,\sigma} t_{ij}\, c^{\dagger}_{i,\sigma} c_{j,\sigma} + U\sum_i \hat{n}_{i,\uparrow}\hat{n}_{i,\downarrow} \tag{1.3}$$

in position space. Until now, we can not get the exact solution of the 3-d Hubbard model at nonzero finite U/t, but we can get the exact solution of the Hubbard model in the atomic limit $t_{ij} = 0$, and in the non-interacting limit $U = 0$.

In the Fermi-Gas limit, $U = 0$, the Hubbard Hamiltonian is diagonal in the momentum space

$$H = \sum_{\mathbf{k}\sigma} E_{\mathbf{k}} c^{\dagger}_{\mathbf{k}\sigma} c_{\mathbf{k}\sigma}.$$

There is only one band and we know that the density of states reads

$$\rho_\sigma(\omega) = \frac{1}{N}\sum_{\mathbf{k}} \delta(\omega - E_{\mathbf{k}}).$$

When the number of free electrons equals to the number lattice sites, the band is half-filled and this model describes a metallic behavior.

In the atomic limit, we have $t_{ij} = 0$, $i \neq j$, and $t_{ii} = N^{-1}\sum_{\mathbf{k}} E_{\mathbf{k}} \equiv \varepsilon_0$ is the average

onsite electron energy. The Hamiltonian is diagonal in position space,

$$H = \varepsilon_0 \sum_{i,\sigma} \hat{n}_{i,\sigma} + U \sum_i \hat{n}_{i,\uparrow}\hat{n}_{i,\downarrow}. \tag{1.4}$$

We define the Green's function in position space as

$$G_{ij,\sigma}(\omega) = -i\frac{1}{2\pi}\int_{-\infty}^{\infty} dt\, e^{i\omega t}\theta(t)\langle\left[c_{i,\sigma}(t),\, c^{+}_{j,\sigma}(0)\right]_{+}\rangle,$$

and use the equation of motion to get the exact solution

$$G_{ij,\sigma}(\omega) = \frac{\delta_{ij}}{2\pi}\left\{\frac{1-n/2}{\omega-\varepsilon_0} + \frac{n/2}{\omega-\varepsilon_0-U}\right\}. \tag{1.5}$$

The density of states is given by

$$\rho_\sigma(\omega) = (1-\frac{n}{2})\delta(\omega-\varepsilon_0) + \frac{n}{2}\delta(\omega-\varepsilon_0-U). \tag{1.6}$$

From Eq. (1.6), it can be seen that the "band" (there are actually only atomic energy levels here instead of energy bands , because we set $t_{ij} = 0$.) splits into two bands, where one band centers at ε_0 and the other band centers at $\varepsilon_0 + U$. Each band has a bandwidth of 0. If this model is half-filled, the lower Hubbard band is full and the upper Hubbard band is empty. This model is then an insulator.

The average occupation number $\langle n\rangle$ can also be used to show this so-called Hubbard gap. In the atomic limit, we have only four possible states: $|0\rangle, |\uparrow\rangle, |\downarrow\rangle, |\uparrow\downarrow\rangle$. Since ε_0 is the energy shift, we can set it to 0. The grand canonical partition function is defined as

$$\begin{aligned} Z &= \mathrm{Tr}\langle\phi|e^{-\beta(H-\mu\hat{n})}|\phi\rangle \\ &= 1 + e^{\beta\mu} + e^{\beta\mu} + e^{-\beta(U-2\mu)}. \end{aligned}$$

The average occupation number is then given by

$$\begin{aligned} \langle n\rangle &= \frac{\mathrm{Tr}\langle\phi|\hat{n}\, e^{-\beta(H-\mu\hat{n})}|\phi\rangle}{Z} \\ &= \frac{0 + e^{\beta\mu} + e^{\beta\mu} + 2e^{-\beta(U-2\mu)}}{Z} \\ &= 2\frac{e^{\beta\mu} + e^{-\beta(U-2\mu)}}{1 + 2e^{\beta\mu} + e^{-\beta(U-2\mu)}}. \end{aligned} \tag{1.7}$$

If we set $U = 1$, we obtain $\langle n\rangle$ as shown in Fig. 1.1. μ is the chemical potential, which is the energy to pay when one electron is added to the system. When the occupation number $\langle n\rangle \leq 1$, the energy cost is very low, which means μ is very small. At low temperatures, this is very obvious and we find that the occupation number $\langle n\rangle$ grows

from 0 to 1 with only small change of μ. This is the case when electrons fill up the lower Hubbard band. When every lattice site is occupied by one electron, and we want to add one more electron to this system, we have to pay the energy U because of the on-site Coulomb repulsion energy. The chemical potential jumps from 0 to 1 (1 is the value of U) at low temperatures (e.g. $T \to 0$), and $\langle n \rangle$ grows quickly compared to a small change in μ. This is the case when electrons fill out the upper Hubbard band. At high temperatures (e.g. $T = 0.5U$), we can not find this step structure in $\langle n \rangle$ against μ curve. This shows that the lower and the upper Hubbard band have already merged together, there is no energy gap in between. Thus, we can not find the jump of μ. This is the metallic state. So, we can confidently conclude that at some temperature $0 < T_c/U < 0.5$, the system at atomic limit ($t_{ij}/U \ll 1$) changes from an insulator to a metal.

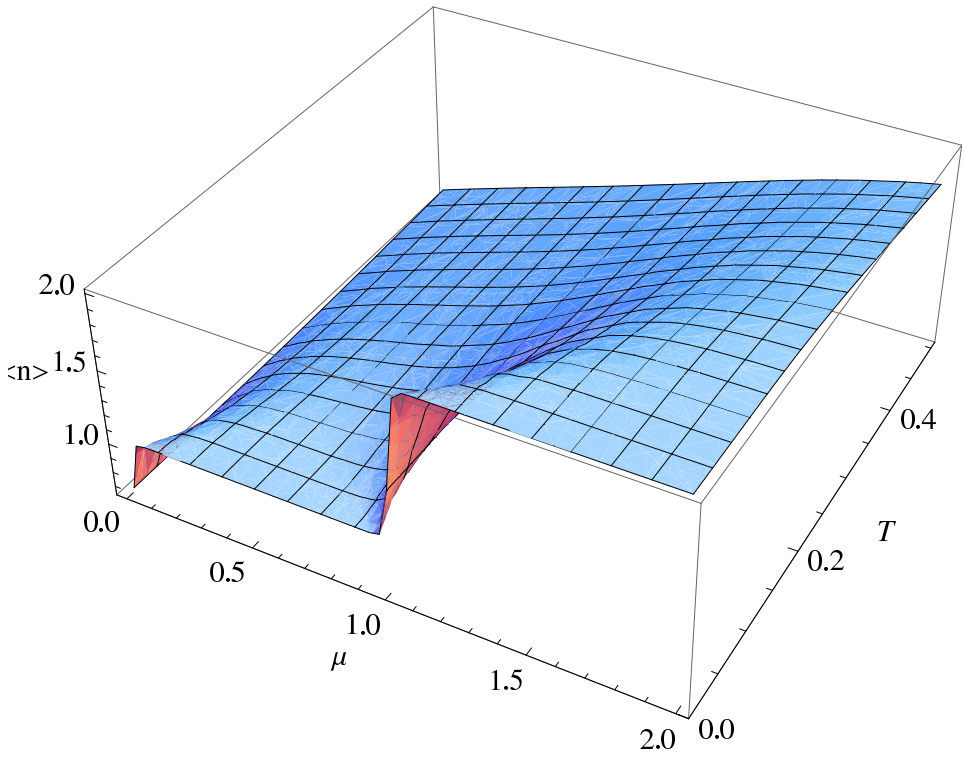

Figure 1.1.: Occupation Number depends on the chemical potential and the temperature.

The local moment $\langle M^2 \rangle = \langle (n_\uparrow - n_\downarrow)^2 \rangle$ is also an indicator which can be used to verify this MIT. The local moment can be calculated as follows

$$\begin{aligned} \langle M^2 \rangle &= \langle n_\uparrow^2 + n_\downarrow^2 - 2n_\uparrow n_\downarrow \rangle \\ &= \langle n \rangle - 2\langle n_\uparrow n_\downarrow \rangle \\ &= [2(e^{\beta\mu} + e^{-\beta(U-2\mu)}) - 2e^{-\beta(U-2\mu)}]/Z \\ &= \frac{2e^{\beta\mu}}{1 + 2e^{\beta\mu} + e^{-\beta(U-2\mu)}}. \end{aligned} \tag{1.8}$$

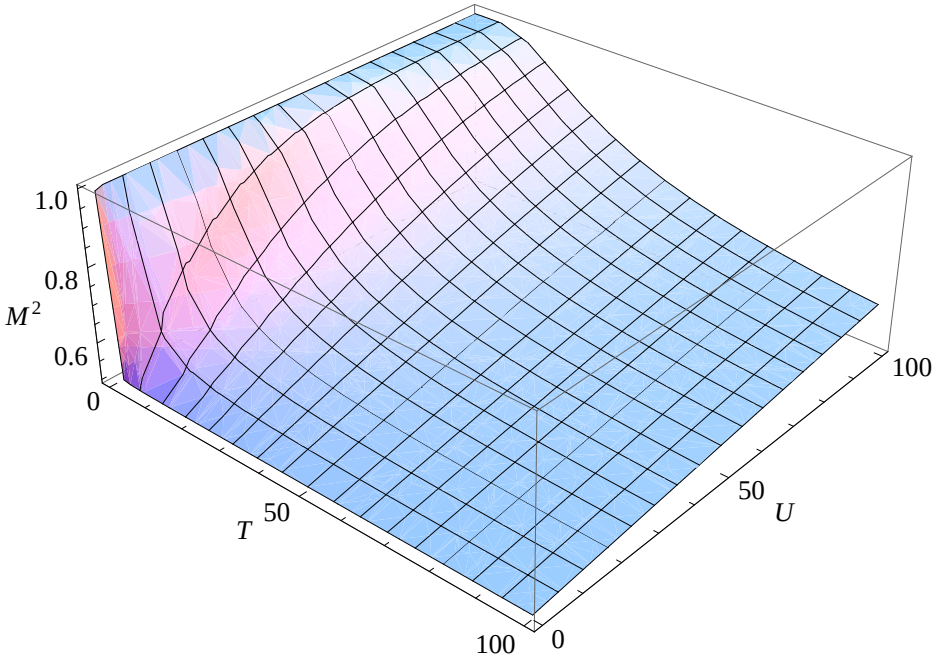

Figure 1.2.: The local moment as a function of U and T at half-filling.

Fig. 1.2 shows the local moment function. At low temperatures and strong interactions, $\langle M^2 \rangle = 1$, which means every site has only one electron whose spin is either up or down. This describes the anti-ferromagnetic insulating ground state. At high temperatures and weak interactions, Eq. (1.8) yields $\langle M^2 \rangle = 0.5$, which is the disordered state. At this state, each lattice site could be either singly occupied with $|\uparrow\rangle, |\downarrow\rangle$, doubly occupied with $|\uparrow\downarrow\rangle$, or empty $|0\rangle$. Each state has the same possibility of 0.25. Considering that the doubly occupied state $|\uparrow\downarrow\rangle$ and the empty state $|0\rangle$ have both a moment of 0, and the two singly occupied states $|\uparrow\rangle, |\downarrow\rangle$ has a moment of 1, the total moment is $\langle M^2 \rangle = 1 \times 0.25 + 1 \times 0.25 = 0.5$. This describes the metallic state, and it matches the result of Eq. (1.8).

In the narrow band limit $U \gg t \neq 0$, we can only get an approximate solution (Hubbard, 1964b) for $d > 1$. From the atomic limit results, we conclude that for $t > 0$ the system will have a lower and an upper Hubbard band with the bandwidth $D = 2dt$. The bandwidth is very small compared to U. Hence, the two bands have a large gap in between. As t increases and U is kept constant, the bandwidth D also increases and the gap between the two Hubbard bands becomes narrower until the lower and the upper Hubbard band merge into one band. The system then changes from an insulating state into a metallic state. Although this explanation of the MIT is not correct, because it fails to predict the Fermi liquid behavior in the metallic state, it shows us that the Hubbard model can be used to describe the metal-insulator phase transition.

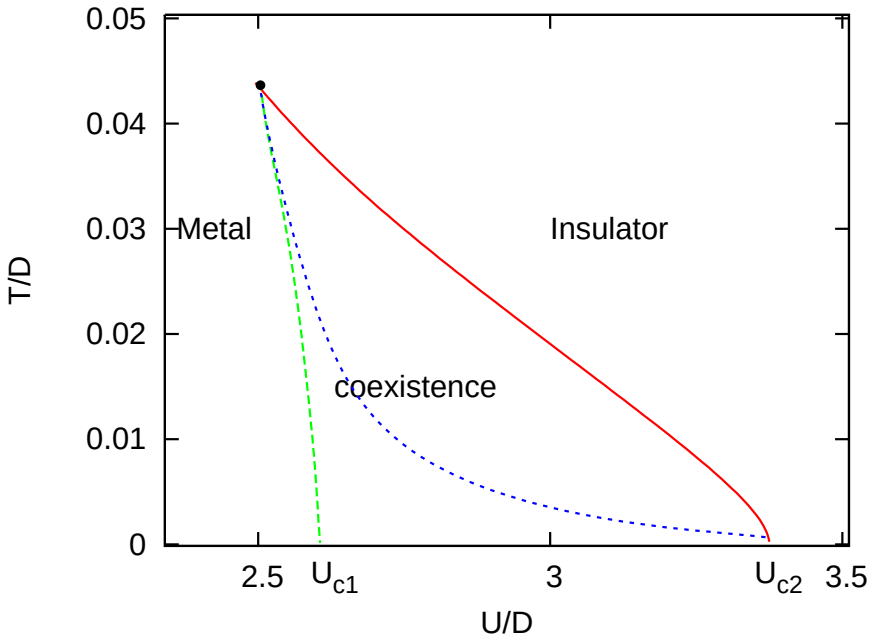

Figure 1.3.: Phase diagram of the fully frustrated model at half-filling (taken from Georges et al. (1996)). It is possible to move continuously from one phase to the other since at high temperature the transition becomes a crossover. Within the region delimited by the red and the green line, the metallic and insulating solutions coexist. The blue dotted line is the approximate location of the actual first-order transition line. Both ends of this line [at the black dot and at $U_{c2}(T) = 0$] are second-order points.

1.2. Micro-Domain Formation in MIT

As the Mott-Hubbard MIT at finite temperatures is a first order phase transition, there exists a phase coexistence region in the phase diagram. Rozenberg et al. (1992) showed that the effective field method (What is called DMFT now) used by Georges and Kotliar (1992) can be used to study the metal insulator phase transition. Two years later, Rozenberg et al. (1994a) extended their calculation to $T = 0$ and gave out the whole MIT phase diagram Fig. 1.3. They found that there exists a region of interaction strengths in which the self-consistency equations yield both metallic and insulating solutions. If we start with a metallic input, and we increase U, we will find these equations converges infallibly at a metallic solution until U/D goes across the red line in Fig. 1.3 to the Insulator side. If we start with an insulating input, and decrease U, we could only get an insulating solution until U/D goes across the green line, see Fig. 1.3. In the coexistence region, we compare the free energy of these two solutions at the same U and T, and find that $F_M < F_I$ on the left side of the blue line and $F_M > F_I$ on the right side of the blue line. The blue line indicates the first order phase transition line on which $F_M = F_I$. Since there are two possible states in the coexistence region, the low energy state could be thermally excited into the high energy

state. Thus, in a bulk material which is in the coexistence region with the parameter of U and T, there could be some domains which are in the high energy state. This kind of domain structure has also been observed in several experiments.

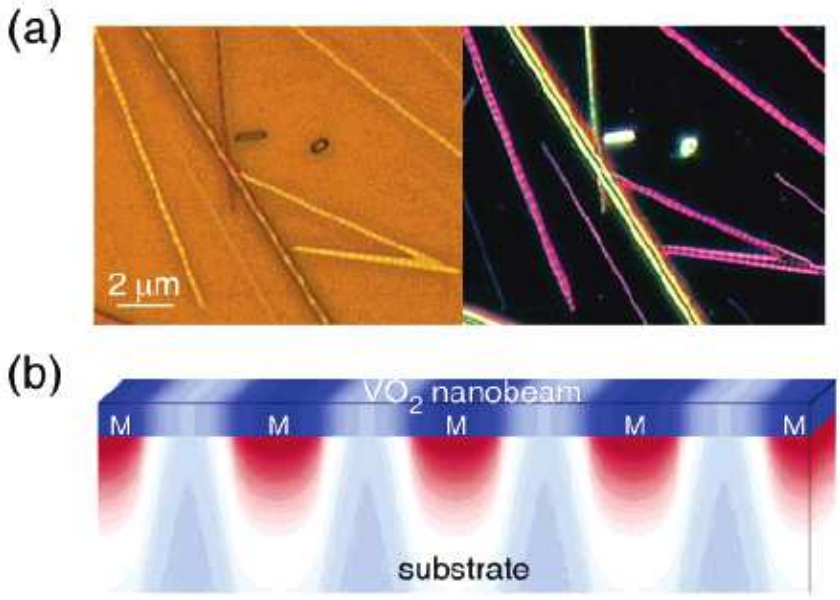

Figure 1.4.: (a) Optical images of VO_2 nanobeams at $T = 100℃$. (b) schematic diagram showing the periodic domain pattern of a VO_2 nanobeam on a SiO_2 substrate. Figures taken from (Wu et al., 2006).

Wu et al. (2006) investigated the substrate-induced strain on the MIT in single crystal VO_2. They observed that in the phase coexistence region insulating and metallic domains coexist in the single crystal VO_2 as shown in Fig. 1.4. Since the optical properties of VO_2 changed dramatically in the visible region when there is a MIT (Fisher, 1976; Lopez et al., 2004), the optical imaging of the nanobeam exhibited a color change from bright to dark, indicating the domain coexistence in the single crystal VO_2 nanobeam. This domain structure has a fundamental effect on the total resistivity. As shown in Fig. 1.5, they measured the resistivity along the nanobeam. Obviously, the insulating domains will increase the total resistivity. For the case in one dimensional system, the total resistivity equals the sum of insulating and metallic domain resistivity. In a 3-d system, the insulating and metallic domains will form a resistor network which will affect the total resistivity in a non-trivial way. This total resistivity could theoretically be calculated with Kirchhoff theory, if the computing power is strong enough for a given system size (Section 6.3).

When high energy domains are thermally excited from the low energy state, a domain wall is formed in between. Let us take the insulating domain inside a metallic bulk as an example. In the insulating state, there is an energy gap between the lower and upper Hubbard band, and this gap lowers the electrons' mobility. The resonant spin-flip opens a channel for this mobility, and this is the reason that we can observe a

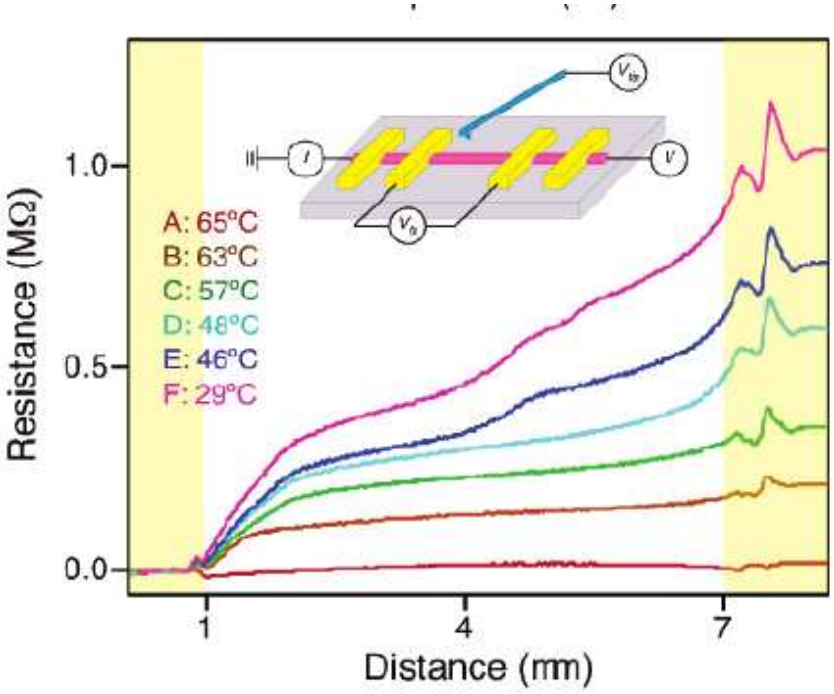

Figure 1.5.: Resistance profile along the nanobeam (The label of x-axis should have a unit of μm, the label of the original figure is miss-typed.). The resistivity $\rho = dR/dl$. Steeper gradient indicates higher resistivity density. This profile shows the position and size of insulating and metallic domains. Figure taken from (Wu et al., 2006).

Kondo resonance peak in the metallic state. A domain wall is formed which connects the metallic state to the insulating state. In our calculation, we find that the formation of domain walls cost energy, and the amount of this energy depends on the free energy difference $\Delta F \equiv F_M - F_I$. Furthermore, we show that the domain distribution function depends on U and T.

Since the domain distribution function depends on the temperature when the pressure remains unchanged (this is equivalent to a fixed U in the Hubbard model) , and the total resistivity depends on the domain distribution, we can derive the relation between resistivity R and temperature T. This is introduced in Chapter 6.

For example, the compound $Sr_2RuO_{4-\delta}$ shows the superconducting property when $T < T_c = 1\mathrm{K}$. Above T_c, the resistivity grows linearly as T increases (see Fig. 1.6). This linear resistivity persists up to $\sim 1000\mathrm{K}$ (Berger et al., 1998; Pavuna et al., 1999; Allen et al., 1996). The linear resistivity behavior exists also in copper compounds superconductors, $Bi_2Sr_2CuO_6$ has a linear resistivity up to $700\mathrm{K}$ (Martin et al., 1988), and $La_{2-x}Sr_xCuO_4$ exhibits linear resistivity up to $1100\mathrm{K}$ (Gurvitch and Fiory, 1987)(For a review, see Imada et al. (1998)).

This T-linear resistivity is interesting because it is contradiction to the usual behaviour $\rho \propto T^2$ (Eq. (B.21)) in the Fermi-liquid theory and $\rho \propto T^5$ (Eq. (B.27)) originating from the electron-phonon interaction. Many theories have been proposed to

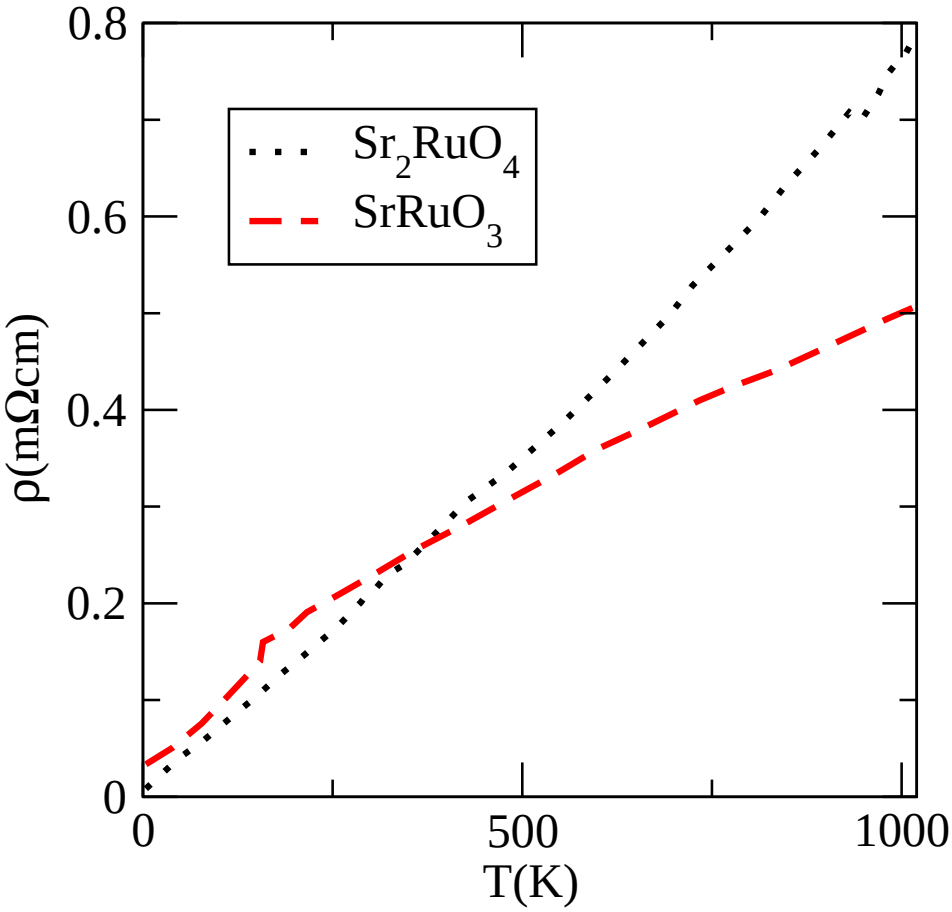

Figure 1.6.: Resistivity of $Sr_2RuO_{4-\delta}$ and $SrRuO_4$. Sr_2RuO_4 shows linear resistivity over three decades of temperature. Figure taken from (Pavuna et al., 1999).

investigate this linear resistivity. The spin-fluctuation theory ascribes this behavior to the scattering of carriers by paramagnetic excitations (Moriya et al., 1990). The slave-boson approximation with coupling between spinons and holons treated by gauge field leads also to this T-linear behavior (Ioffe and Kotliar, 1990; Ioffe and Wiegmann, 1990; Ioffe and Larkin, 1989). This T-linear behavior can also be obtained by marginal Fermi-liquid theory (Varma et al., 1990, 1989), where $\mathrm{Im}\Sigma$ is proportional to T. In Chapter 6, we will calculate the network resistivity ρ with domains distributed by a function $P(R)$ inside a bulk. As a result it turns out that the resistivity increases linearly as temperature increases Fig. 6.7.

Chapter 2.

Anderson Impurity Model and NCA Solver

In Chapter 1, we have discussed that the dynamical mean field theory maps a lattice model onto an impurity model, and in the case of the Hubbard model, the corresponding impurity model is the Anderson impurity model (Anderson, 1961). Ever since this model was proposed, a lot of methods including perturbation theory (Yosida and Yamada, 1970), the renormalization group method (Wilson, 1975), the Fermi liquid method (Nozières, 1974), and non crossing approximation (NCA) method (Keiter and Kimball, 1971; Pruschke and Grewe, 1989) have been proposed to solve this model. We introduce the NCA method in this chapter.

To apply the NCA to the finite-U Hubbard model, four pseudo particle operators are required by the pseudo particle representation. The saddle point approximation leads to Gutzwiller's variational wave function (Kotliar and Ruckenstein, 1986). Therefore, this method can resolve the low energy features of the Hubbard model. To study the high energy features of a pseudo particle formalism, the summation of a particular perturbation series in powers of the hybridization $\tilde{\Delta}$ is required (Pruschke et al., 1993). As we are studying the domain problem which dominates in the high temperature region, the NCA is also applicable in this range of parameters.

2.1. The Anderson Impurity Problem

Before we derive the DMFT equations, we introduce the Anderson impurity model first. In the DMFT theory, a lattice of atoms is replaced by an impurity atom which interacts with a bath of electrons. This approximation captures the dynamics of the electrons on a central atom as it fluctuates among different configurations by exchanging particles with the bath: empty occupied $|0\rangle$, singly occupied $|\uparrow\rangle$ or $|\downarrow\rangle$, and doubly occupied $|2\rangle = |\uparrow\downarrow\rangle$. The key point in solving the DMFT equations is how to solve the impurity model. Georges and Kotliar (1992) showed that the Hubbard Model (Eq. (1.3)) can be mapped onto the Anderson impurity model

$$H_{AM} = \sum_{\mathbf{k},\sigma} E_{\mathbf{k}} c^{\dagger}_{\mathbf{k}\sigma} c_{\mathbf{k}\sigma} + \varepsilon_d \sum_{\sigma} d^{\dagger}_{\sigma} d_{\sigma} + U\, n_{d\uparrow} n_{d\downarrow} + \sum_{\mathbf{k},\sigma} V_{\mathbf{k}} (c^{\dagger}_{\mathbf{k}\sigma} d_{\sigma} + H.c.), \tag{2.1}$$

where $E_{\mathbf{k}}$ describes the conduction band, and ε_d is the reference energy of the impurity site. At half-filling, we choose the Fermi level $E_F \equiv 2\varepsilon_d + U$ to be 0. Thus, we have $\varepsilon_d = -U/2$. $V_{\mathbf{k}}$ describes the hybridization of the conduction band and the impurity. The Anderson model is widely used to study magnetic impurities inside metals (Hewson, 1993).

2.1.1. Pseudo Particle Representation

The difficulty of solving the Anderson impurity model is that the perturbation theory in U does not work when U is greater than the half bandwidth D. This is because a large repulsion U makes the doubly occupied states energy-costly and this means the doubly occupied states affect the low energy states only via virtual processes. The dynamics is thus constrained to a subspace of the total Hilbert space. It is very difficult to project the original problem to this subspace. It requires us to use auxiliary particles to perform this projection. The perturbation expansion in kinetic energy is also difficult because of the infinite degeneracy of the ground state of a lattice model when t is small. Furthermore, the conventional diagram technique fails here because Wick's theorem does not apply to a strongly correlated system. This can be seen by noticing that the Hubbard operator $X_{pq} = |p\rangle\langle q|$ does not obey the canonical (anti-)commutator relations (Hubbard, 1964b), where $|p\rangle$ and $|q\rangle$ belong to one of the four states $|0\rangle$, $|\uparrow\rangle$, $|\downarrow\rangle$, and $|2\rangle$. We have to use pseudo particles to make the Wick's theorem valid. Then we can use the well known diagram techniques to solve this problem.

For an impurity model, the occupancy in the impurity site is very important. At finite U, this site can be each of the four states: the empty state $|0\rangle$, the singly occupied state $|\uparrow\rangle$, $|\downarrow\rangle$, and the doubly occupied states $|\uparrow\downarrow\rangle = |2\rangle$. It is straightforward to divide the total Hilbert space into four sectors, with each sector labeled by one state. We define a creation operator $\alpha^\dagger$ for each sector $|\alpha\rangle$ as this operator can create a state $|\alpha\rangle$ from the vacuum state $|vac\rangle$: $|\alpha\rangle = \alpha^\dagger|vac\rangle$. For an impurity, whose spin degeneracy is 2, we define boson operator b and a, and two fermion operator f_σ, $\sigma = \uparrow, \downarrow$. The boson operator $b^\dagger$ creates an empty state from the vacuum state $|0\rangle = b^\dagger|vac\rangle$, and $a^\dagger$ creates a doubly occupied state $|2\rangle = a^\dagger|vac\rangle$. The fermion operator $f_\sigma^\dagger$ creates a singly occupied state with spin σ, $|\sigma\rangle = f_\sigma^\dagger|vac\rangle$. The electron creator $d^\dagger$ creates a singly occupied state from the empty state $|\sigma\rangle = d_\sigma^\dagger|0\rangle$, and also a doubly occupied states $|2\rangle = d_\downarrow^\dagger|\uparrow\rangle = -d_\uparrow^\dagger|\downarrow\rangle$. Therefore, the electron operator $d^\dagger$ is expressed in terms of the pseudo particle operators as

$$d_\sigma^\dagger = f_\sigma^\dagger b + \eta_\sigma a^\dagger f_{-\sigma}, \tag{2.2}$$

where $\eta_\sigma = \pm 1$, for $\sigma = \uparrow, \downarrow$ is introduced because of the antisymmetry for the doubly occupied states.

The use of pseudo particles enlarges the Fock space. The physics requires that the impurity site should be occupied with one and only one pseudo particle a time.

Therefore, we have the the pseudo particle number constraint

$$Q = \sum_{\sigma} f_{\sigma}^{\dagger} f_{\sigma} + b^{\dagger} b + a^{\dagger} a = 1. \tag{2.3}$$

With Eq. (2.2) and Eq. (2.3), the Hamiltonian (2.1) can be rewritten using the pseudo particle operators as:

$$\begin{aligned} H = & \sum_{\mathbf{k}\sigma} E_{\mathbf{k}} c_{\mathbf{k}\sigma}^{\dagger} c_{\mathbf{k}\sigma} + \varepsilon_d \left(\sum_{\sigma} f_{\sigma}^{\dagger} f_{\sigma} + 2 a^{\dagger} a \right) + U\, a^{\dagger} a + \\ & + V \sum_{\mathbf{k}\sigma} \left[c_{\mathbf{k}\sigma}^{\dagger} \left(b^{\dagger} f_{\sigma} + \eta_{\sigma} f_{-\sigma}^{\dagger} a \right) + h.c. \right]. \end{aligned} \tag{2.4}$$

In equation Eq. (2.3) and Eq. (2.4), the pseudo particle operators are diagonal except for the hybridization part. Eq. (2.3) is invariant under $U(1)$ gauge transformation: $f_{\sigma} \mapsto f_{\sigma} e^{i\phi(\tau)}$, $b \mapsto b\, e^{i\phi(\tau)}$, and $a \mapsto a\, e^{i\phi(\tau)}$. As we know any gauge symmetry relates to a conservation law. This $U(1)$ gauge symmetry relates to the conserved quantized charge Q. This property will be used to select the Fock space sector with $Q = 1$ in Section 2.1.2.

2.1.2. Exact Projection to the Physical Fock Space

The $U(1)$ gauge symmetry guarantees the conservation of the quantized charge Q, we have to choose the Fock space sector with $Q = 1$. Here, we follow the method given by Abrikosov et al. (1965) (see also Kroha and Wölfle (2001a)). We first consider the grand canonical density operator

$$\rho_G = \frac{1}{Z_G} e^{-\beta(H + \lambda Q)}, \tag{2.5}$$

where $Z_G = \mathrm{tr}\left\{\exp\left[-\beta(H + \lambda Q)\right]\right\}$ is the grand canonical partition function, and λ is the chemical potential. The trace is taken over the complete Fock space including all Q. The expectation value of an operator $\hat{A}$ in grand canonical ensemble is given by

$$\langle \hat{A} \rangle_G = \mathrm{tr}[\rho_G \hat{A}]. \tag{2.6}$$

Because we mostly consider the physical expectation value $\langle \hat{A} \rangle$, which is the expectation value in the grand canonical ensemble with $Q = 1$, we define $\xi = e^{-\beta\lambda}$. The derivative of $\langle \hat{A} \rangle_G$ is then

$$\frac{\partial \langle \hat{A} \rangle_G}{\partial \xi} = \mathrm{tr}[Q \hat{A} \rho_G] = \langle Q \hat{A} \rangle_G. \tag{2.7}$$

Thus, we have

$$\langle \hat{A} \rangle = \lim_{\lambda \to \infty} \frac{\frac{\partial}{\partial \xi} \mathrm{tr}[\hat{A}\, \rho_G]}{\frac{\partial}{\partial \xi} \mathrm{tr}[\rho_G]} = \lim_{\lambda \to \infty} \frac{\langle Q \hat{A} \rangle_G}{\langle Q \rangle_G}. \tag{2.8}$$

Based on Eq. (2.8), we get the canonical partition function in the subspace $Q = 1$

$$Z_C = \lim_{\lambda \to \infty} \mathrm{tr}\left[Q e^{-\beta(H + \lambda(Q-1))} \right] \tag{2.9}$$

$$= \lim_{\lambda \to \infty} \left[e^{\beta \lambda} \langle Q \rangle_G(\lambda) \right] Z_{Q=0}. \tag{2.10}$$

We also get the canonical expectation value of an operator $\hat{A}$ which reads

$$\langle \hat{A} \rangle_C = \lim_{\lambda \to \infty} \frac{\langle \hat{A} \rangle_G(\lambda)}{\langle Q \rangle_G(\lambda)}, \tag{2.11}$$

if we have $\hat{A}|Q = 0\rangle = 0$. This relation is always true for physical operators acting on the impurity. With this relation, it is easy to find that the constrained d-electron Green's function reads

$$G_d(\omega) = \lim_{\lambda \to \infty} \frac{G_d(\omega, \lambda, T)}{\langle Q \rangle_G(\lambda)}. \tag{2.12}$$

Since $G_d(\omega, \lambda, T)$ is defined on the enlarged Hilbert space, the pseudo fermion and slave bosons are used in this Green's function, thus Wick's theorem is applicable. The pseudo fermion and slave boson Green's functions are defined as

$$\mathcal{G}_{f\sigma}(\tau_1 - \tau_2) = -\langle \hat{T} \left[f_\sigma(\tau_1) f_\sigma^\dagger(\tau_2) \right] \rangle_G, \tag{2.13}$$

$$\mathcal{G}_b(\tau_1 - \tau_2) = -\langle \hat{T} \left[b(\tau_1) b^\dagger(\tau_2) \right] \rangle_G, \tag{2.14}$$

$$\mathcal{G}_a(\tau_1 - \tau_2) = -\langle \hat{T} \left[a(\tau_1) a^\dagger(\tau_2) \right] \rangle_G, \tag{2.15}$$

where $\hat{T}$ is the imaginary time ordering operator. The Dyson equation of this Green's function reads

$$\mathcal{G}_{f,b,a}(i\omega_n) = \left\{ \left[\mathcal{G}^0_{f,b,a}(i\omega_n) \right]^{-1} - \Sigma_{f,b,a}(i\omega_n) \right\}, \tag{2.16}$$

where $\mathcal{G}^0_{f,b,a}$ is the bare Green's function,

$$\mathcal{G}^0_{f\sigma}(i\omega_n) = (i\omega_n - \varepsilon_d - \lambda)^{-1}, \tag{2.17}$$

$$\mathcal{G}^0_{b}(i\omega_n) = (i\omega_n - \lambda)^{-1}, \tag{2.18}$$

$$\mathcal{G}^0_{a}(i\omega_n) = (i\omega_n - 2\varepsilon_d - U - \lambda)^{-1}. \tag{2.19}$$

As the projection procedure $\lambda \to \infty$ scales energy eigenvalues to infinity as λQ, it is useful to shift the pseudo particle frequency by λ. The projected Green's function is defined as

$$G_{f,b,a}(\omega) = \lim_{\lambda \to \infty} \mathcal{G}_{f,b,a}(\omega + \lambda). \tag{2.20}$$

This procedure will not affect the energy scale of physical quantities, because the energies of physical quantities are defined as the energy difference between the pseudo particles.

The local conduction electron Green's function reads

$$G_{c\sigma}(i\omega_n) = \left\{ \left[G^0_{c\sigma}(i\omega_n) \right]^{-1} - \Sigma_{c\sigma}(i\omega_n) \right\}^{-1}, \tag{2.21}$$

with

$$G^0_{c\sigma}(i\omega_n) = \sum_k (i\omega_n + \mu_c - E_k)^{-1}, \tag{2.22}$$

where μ_c is the chemical potential of the conduction electrons. To calculate the self energy $\Sigma_{c\sigma}$, we use the t-matrix, which is defined by the equation $G_{c\sigma} = G^0_{c\sigma}(1 + t_\sigma\, G^0_{c\sigma})$. The hybridization term $V\, c^\dagger_{k\sigma} d_\sigma$ in Anderson impurity model Eq. (2.1) gives us

$$t_\sigma(i\omega_n) = |V|^2 G_d(i\omega_n). \tag{2.23}$$

Comparing this equation with Eq. (2.21), we write out the self energy term as

$$\Sigma_{c\sigma}(i\omega_n) = \frac{|V|^2 G_{d\sigma}(i\omega_n)}{1 + |V|^2 G_{d\sigma}(i\omega_n) G^0_{c\sigma}(i\omega)}. \tag{2.24}$$

This equation expresses the conduction band self energy $\Sigma_{c\sigma}$ in terms of $G_{d\sigma}$. If we can calculate Σ_c, then the impurity Green's function G_d is also known.

2.2. Non-Crossing Approximation

The key point in impurity problems is to find the impurity Green's function G_d defined in Eq. (2.12). Here we present the non-crossing approximation (NCA) as an impurity solver for the Anderson impurity model with finite Coulomb interaction on the impurity sites. Keiter and Kimball (1971) developed this non-crossing diagram technique as a new method to solve the Anderson model for dilute alloys. Kuramoto et al. (Kuramoto, 1983; Kojima et al., 1984; Kuramoto and Kojima, 1984; Kuramoto, 1986) recognized the conserving property of this method. We will start from the conserving approximation to introduce this diagrammatic technique.

2.2.1. Conserving Approximation

In order to maintain the conservation laws for the electron particle number, the momentum, and the energy in approximative methods, Baym and Kadanoff (1961) and Baym (1962) developed the so called conserving approximation, which will obey the conservation laws for particle number, energy and so on when the two-particle correlation function $L(12, 1'2') = G_2(12, 1'2') - G(1-1')G(2-2')$ satisfies

$$L(12, 1'2') = \pm \left[\delta G(1, 1') / \delta U(2, 2') \right]_{U=0}. \tag{2.25}$$

According to the equation of motion, Baym concluded that to generate the conserving approximation, *the self energy must be a functional of* $G(U)$ *and* U, where U stands for the external potential. This conclusion tells us that the conservation laws at the vertex in the diagrammatic expansion is **not** sufficient for the conservation of momentum, energy and particle number. When expressed in terms of the generating functional Φ, the conserving approximation can be formulated as

$$\Sigma(1,1') = \delta\Phi/\delta G(1,1'). \tag{2.26}$$

Here we followed the notation of Baym (1962), $1, 1'$ are the space-time coordinates in the Green's function, and δ stands for the functional differential. As we know, translational invariance of a system yields momentum conservation. We start with the translational invariance of G. This translational invariance

$$G(r,t;r',t';U) \to G(r+R(t);r'+R(t');U) \tag{2.27}$$

should also lead to momentum conservation in many particle physics. We start from the functional variation of Φ

$$\delta\Phi = \int d1d1' \frac{\delta\Phi}{\delta G(1,1')}\delta G(1',1). \tag{2.28}$$

According to Eq. (2.26), $\delta\Phi/\delta G$ can be replaced with Σ, and according to Eq. (2.27)

$$\delta G(1',1) \to \nabla_{1'} G(1',1)\delta 1' + \nabla_1 G(1',1)\delta 1, \tag{2.29}$$

so we have

$$\delta\Phi = \int d2 \left[\nabla_1 G(1,2)\Sigma(2,1') + \Sigma(1,2)\nabla_{1'} G(2,1')\right]. \tag{2.30}$$

The translational invariance of the system ensures that $\delta\Phi = 0$, therefore we should have

$$\int d2 \left[\nabla_1 G(1,2)\Sigma(2,1') + \Sigma(1,2)\nabla_{1'} G(2,1')\right] = 0. \tag{2.31}$$

The equation of motion of the Green's functions reads

$$\int d\bar{1} \left[G_0^{-1}(1,\bar{1}) - U(1,\bar{1}) - \Sigma(1,\bar{1})\right] G(\bar{1},1') = \delta(1-1') \tag{2.32}$$

$$\int d1 G(1,\bar{1}) \left[G_0^{-1}(\bar{1},1') - U(\bar{1},1') - \Sigma(\bar{1},1')\right] = \delta(1-1'). \tag{2.33}$$

We apply $\nabla_{1'}$ to Eq. (2.32) and ∇_1 to Eq. (2.33) and keep in mind that $\nabla_{1'}\delta(1-1') + \nabla_1\delta(1-1') = 0$. After adding Eq. (2.32) and Eq. (2.33), we find

$$\begin{aligned} &\nabla_1 G(1,\bar{1})G_0^{-1}(\bar{1},1') + G_0^{-1}(1,\bar{1})\nabla_{1'} G(\bar{1},1') \\ =&\nabla_1 G(1,\bar{1})U(\bar{1},1') + U(1,\bar{1})\nabla_{1'} G(\bar{1},1'). \end{aligned} \tag{2.34}$$

Replacing G_0^{-1} with $G_0^{-1} = (i\partial_{t_1} + \nabla_1^2/2m)\delta(1-1') = (-i\partial_{t_{1'}} + \nabla_{1'}^2/2m)\delta(1-1')$, the left hand side of Eq. (2.34) reads

$$i\partial_{t_1}(\nabla_1 - \nabla_{1'})G(1,1').$$

The time derivative of the momentum yields

$$\frac{d}{dt_1}\langle P(t_1)\rangle = \frac{d}{dt_1}\int dr_1 \left[\frac{\nabla_1 - \nabla_{1'}}{2i} iG(1,1',U)\right]_{1'\to 1^+}. \tag{2.35}$$

This corresponds to the integrated $(\frac{1}{2i}\int dr_1)$ right hand side of Eq. (2.34). Therefore, we can conclude from Eq. (2.34) and Eq. (2.35) that

$$\frac{d}{dt_1}\langle P(t_1)\rangle = \int dr_1 \int \bar{1}\frac{\nabla_1 - \nabla_{1'}}{2i}\left[U(1,\bar{1})G(\bar{1},1') - G(1,\bar{1})U(\bar{1},1')\right]_{1'=1^+}. \tag{2.36}$$

The potential obeys $U(1,1') = U(1)\delta(1-1')$, applying this to Eq. (2.36), we find

$$\frac{d}{dt_1}\langle P(t_1)\rangle = -\int dr_1[\nabla_1 U(1)]\langle n(1)\rangle_U. \tag{2.37}$$

The right hand side of Eq. (2.37) is exactly the total force applied to the system. Thus Eq. (2.37) tells us that the time derivative of momentum equals to the total force applied to the system. This is actually the statement of momentum conservation. The conservation of the particle number, the energy etc. can also be derived using the gauge invariance $G(1,1') \to e^{i\Lambda(1)}G(1,1')e^{-i\Lambda(1')}$ and the time reverse invariance $G(1,1') \to (d\theta/dt)^{1/4}G(r,\theta(t),r',\theta(t'))(d\theta'/dt')^{1/4}$.

As an example, we show that the Hatree-Fock approximation

$\Sigma =$ 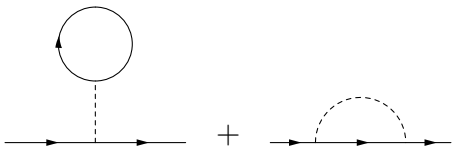 (2.38)

is the functional derivative of Φ

$\Phi =$ 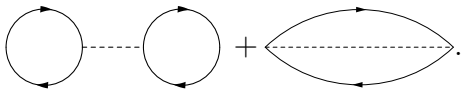 (2.39)

Therefore, the Hatree-Fock approximation is a conserving approximation.

2.2.2. The Non-Crossing Approximation (NCA) Diagrams

The generating functional Φ for the Anderson impurity model in terms of pseudo particles should consist of all vacuum skeleton diagrams, which are built of fully

renormalized Green's functions $G_\mu,\ \mu = a, b, c, f_\sigma$, where a is the heavy boson, b the light boson, f_σ the pseudo fermion, and c the conduction band electron. According to the conserving approximation theory, the self-energy is calculated by

$$\Sigma_\mu = \frac{\delta \Phi}{\delta G_\mu}. \tag{2.40}$$

The NCA is defined as the renormalized low order perturbation theory with the small parameter V/D, where D is the band width and V the interaction between the impurity and the conduction band. The conserving approximation theory requires that the self-energies are to be determined self-consistently. Hence this calculation contains the infinite resummation of the perturbation theory even if we only keep the second order skeleton diagram for Φ,

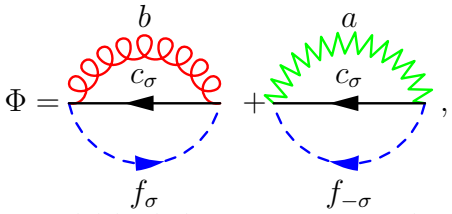

(2.41)

where the red, green, blue and black lines correspond to light boson b, heavy boson a, pseudo fermion f_σ and conduction electron c. The physical interpretation of this approximation can be discussed regarding the conduction-pseudo-fermion vertex function. The irreducible c-f vertex function can be derived taking the second functional derivative of Φ with respect to G_f and G_c. The irreducible c-f vertex function is then given by $V^2 G_b$ (or $V^2 G_a$) and depends on the spin configuration of f and c. The self-energy equations can be derived using Eq. (2.40)

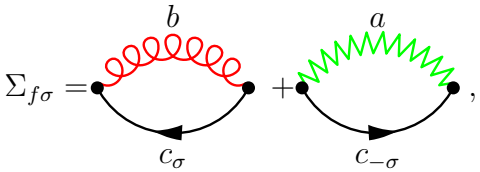

(2.42)

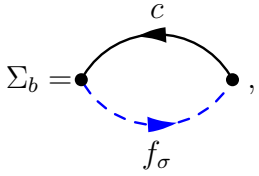

(2.43)

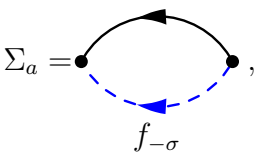

(2.44)

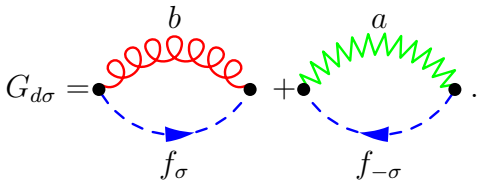

(2.45)

To evaluate these self-energies, we have

$$\Sigma_{f\sigma}(i\omega) = -\frac{V^2}{\beta}\sum_{i\omega'}[G_{c\sigma}(i\omega')G_b(i\omega - i\omega') + G_{c,-\sigma}(i\omega')G_a(i\omega + i\omega')], \tag{2.46}$$

$$\Sigma_b(i\Omega) = \frac{V^2}{\beta}\sum_{i\omega,\sigma} G_{c\sigma}(i\omega)G_{f\sigma}(i\Omega + i\omega), \tag{2.47}$$

$$\Sigma_a(i\Omega) = \frac{V^2}{\beta}\sum_{i\omega,\sigma} G_{c\sigma}(i\omega)G_{f,-\sigma}(i\Omega - i\omega), \tag{2.48}$$

$$\Sigma_c(i\omega) = V^2 G_d = -\frac{V^2}{\beta}\sum_{i\omega',\sigma}[G_{f\sigma}(i\omega')G_b(i\omega' - i\omega) + G_{f,-\sigma}(i\omega')G_a(i\omega + i\omega')], \tag{2.49}$$

where $i\omega$, $i\omega'$ and $i\Omega$ are fermionic and bosonic Matsubara frequencies. V^2 is calculated self consistently as the NCA equations converge.

A comparison of NCA results for the auxiliary particle and d-electron spectral functions $A_{f,b,d}$ with the results obtained for the single-channel case using NRG method shows that the pseudo particle spectral functions from NCA calculations are correct at energies $\omega > T_K$, where $T_K = D(M\Gamma/\pi D)^{M/N}\exp[-\pi|E_d|/N\Gamma]$ (Costi et al., 1996). However in low energies $\omega \ll T_K$, NCA fails. For the one band Hubbard model, we have only one channel, $M = 1$, and one spin number, $N = 2$. The phase transition occurs at $U \sim 2D$, thus $|E_d| = D$. The effective coupling constant is given by $\Gamma = \pi V^2 N(0)$, with $N(0)$ being the conduction electron density of states at the Fermi level. In my calculations, πV^2 ranges from 0.6 to 0.8, and $N(0)$ has a range from 0.01 to 0.45. This depends on whether it's in the insulating or the metallic state. Therefore, T_K has a maximum value of $0.00087D$, which is much lower then the phase transition temperature in our calculations (from $0.0042D$ to $0.0052D$). Therefore, we can use the NCA to investigate the MIT.

The failing of NCA at low temperatures can be explained by showing that the Bethe-Salpeter equation for the c-f vertex does not contain the spin-flip contribution, which is responsible for the coherent collective behavior below T_K. If we take the interactions shown in Fig. 2.1 into the generating functional Φ, the conserving-T matrix approximation (CTMA) is constructed (Kroha et al., 1997). The CTMA recovers the Fermi liquid behavior of the Anderson impurity model at low temperature. CTMA calculations are quite demanding and it is not necessary to apply this method to the domain problem in this thesis, because we are interested in the phase coexistence region, where $T > T_K$.

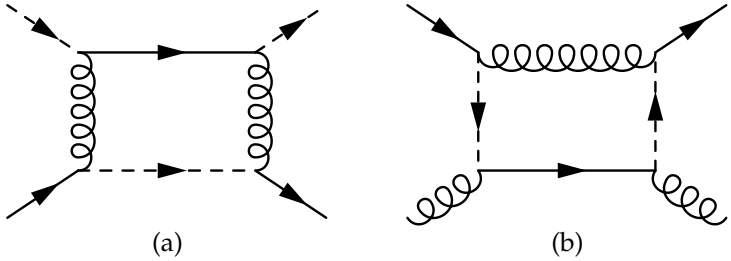

Figure 2.1.: (a) This conduction electron-pseudo fermion (c-f) vertex, which includes the spin flip contribution is neglected in NCA. (b) The conduction electron-slave boson(c-b) vertex which includes the charge fluctuation process is also neglected in NCA.

2.2.3. The NCA Equations

Although the NCA fails to give correct result at $T < T_K$, we still have a method to solve NCA equations even at low temperatures. This method is based on the fact that the pseudo-particle spectral functions $A_{f,b,a}$ vanishes for $\omega < 0$ and behaves as

$$A_{f,b,a} \sim |\omega - E_0|^{-\alpha_{a,b,f}} \theta(\omega - E_0), \tag{2.50}$$

where α is the critical exponent and E_0 the threshold. This can be derived using the NRG approach as done by Costi et al. (1996). The threshold behavior must be resolved in numerical calculation by iteration (Kroha and Wölfle, 2001a). The calculation of G_d is also difficult because A_f diverges at E_0 and E_0 is not initially known. Furthermore, the frequency summation in Eq. (2.49) gives the Fermi function which includes a factor of $e^{-\beta\omega}$. This factor diverges exponentially for $\omega < 0$ as $T \to 0$. To overcome this difficulty, we apply a gauge transformation to the pseudo particles because this is the intrinsic property of the Anderson impurity model as mentioned in Subsection 2.1.1. Then we replace $f_\sigma \to e^{i\lambda_0 t} f_\sigma$, $b \to e^{i\lambda_0 t} b$, $a \to e^{i\lambda_0 t} a$. After this transformation, the pseudo particle spectral functions changes as if the energy was shifted by λ_0. Thus, we have the "new" spectral function

$$A_{f,b,a}(\omega) = \lim_{\lambda \to \infty} \mathcal{A}_{f,b,a}(\omega + \lambda + \lambda_0), \tag{2.51}$$

and $\mathcal{A}_\mu(\omega) = \pm(1/\pi)\mathrm{Im}\mathcal{G}_\mu(\omega)$. The '+/-' sign corresponds to the retarded/advanced Green's function defined in Eq. (2.15).

As the total number of the pseudo particles should be equal to 1 (Eq. (2.3)), we have the constraint

$$\int e^{-\beta\omega} \left[\sum_\sigma A_{f_\sigma}(\omega) + A_b(\omega) + A_a(\omega) \right] d\omega = 1. \tag{2.52}$$

Under this constraint we determine the energy shift λ_0 within each iteration.

In the low temperature limit $T \to 0$, $e^{-\beta\omega}$ decreases rapidly as ω increases from $-\infty$

to $+\infty$. λ_0 is determined so that the threshold energy at E_0 is fixed in the vicinity of 0. To implement this numerically, we create an energy axis with increasing number of grid points around $\omega = 0$ for the integral equations of the NCA. Equation (2.52) also implies that the pseudo particle spectral function grows as $e^{\beta\omega}$ when $\omega < 0$. This gives us a hint that we can absorb the threshold behavior into new functions by defining

$$A_\mu(\omega) = f(-\omega)\tilde{A}_\mu(\omega), \tag{2.53}$$

$$\mathrm{Im}\Sigma_\mu(\omega) = f(-\omega)\mathrm{Im}\tilde{\Sigma}_\mu(\omega),\ \mu = a, b, f_\sigma. \tag{2.54}$$

The new functions $\tilde{A}_\mu$ and $\mathrm{Im}\tilde{\Sigma}_\mu$ will not diverge when $\omega < 0$. Furthermore, we know that the pseudo particle spectral function goes to 0 as ω increases when $\omega > 0$, this property ensures that the new function $\tilde{A}_\mu$ will not diverge at positive energies. With these newly defined functions, the NCA equations can be rewritten as

$$\mathrm{Im}\widetilde{\Sigma}_{f\sigma}(\omega) = \Gamma \int \mathrm{d}\varepsilon \frac{f(\varepsilon-\omega)f(-\varepsilon)}{f(-\omega)}[A_{c\sigma}(\omega-\varepsilon)\widetilde{A}_b(\varepsilon) + A_{c,-\sigma}(\varepsilon-\omega)\widetilde{A}_a(\varepsilon)] \tag{2.55}$$

$$\mathrm{Im}\widetilde{\Sigma}_b(\Omega) = \Gamma \int \mathrm{d}\varepsilon \frac{f(\varepsilon-\Omega)f(-\varepsilon)}{f(-\Omega)}[A_{c\sigma}(\varepsilon-\Omega)\widetilde{A}_{f\sigma}(\varepsilon) + A_{c,-\sigma}(\varepsilon-\Omega)\widetilde{A}_{f,-\sigma}(\varepsilon)] \tag{2.56}$$

$$\mathrm{Im}\widetilde{\Sigma}_a(\Omega) = \Gamma \int \mathrm{d}\varepsilon \frac{f(\varepsilon-\Omega)f(-\varepsilon)}{f(-\Omega)}[A_{c\sigma}(\Omega-\varepsilon)\widetilde{A}_{f,-\sigma}(\varepsilon) + A_{c,-\sigma}(\Omega-\varepsilon)\widetilde{A}_{f\sigma}(\varepsilon)], \tag{2.57}$$

where $\Gamma = \pi V^2$. The constraint for $\langle Q \rangle$ in Eq. (2.52) is transformed to

$$\int d\omega\, f(\omega) \left[\sum_\sigma \tilde{A}_{f_\sigma}(\omega) + \tilde{A}_a(\omega) + \tilde{A}_b(\omega) \right] = 1, \tag{2.58}$$

which can be used to determine the parameter λ_0. The redefined functions denoted by tilde are given by

$$\tilde{A}_{f\sigma}(\omega) = \frac{1}{\pi} \frac{\mathrm{Im}\tilde{\Sigma}_{f\sigma}(\omega)}{(\omega + \lambda_0 - E_d - \mathrm{Re}\Sigma_{f\sigma}(\omega))^2 + \mathrm{Im}\Sigma_{f\sigma}(\omega)^2} \tag{2.59}$$

$$\tilde{A}_b(\omega) = \frac{1}{\pi} \frac{\mathrm{Im}\tilde{\Sigma}_b(\omega)}{(\omega + \lambda_0 - \mathrm{Re}\Sigma_b(\omega))^2 + \mathrm{Im}\Sigma_b(\omega)^2} \tag{2.60}$$

$$\tilde{A}_a(\omega) = \frac{1}{\pi} \frac{\mathrm{Im}\tilde{\Sigma}_a(\omega)}{(\omega + \lambda_0 - E_a - \mathrm{Re}\Sigma_a(\omega))^2 + \mathrm{Im}\Sigma_a(\omega)^2} \tag{2.61}$$

$$\begin{aligned} A_d(\omega) = \int d\varepsilon \tilde{A}_f(\varepsilon) \Big\{ &[f(\varepsilon)f(\omega-\varepsilon) + f(\varepsilon-\omega)f(-\varepsilon)]\, \tilde{A}_b(\varepsilon-\omega) \\ &+ [f(-\varepsilon)f(\omega+\varepsilon) + f(-\varepsilon-\omega)f(\varepsilon)]\, \tilde{A}_a(\varepsilon+\omega) \Big\}. \end{aligned} \tag{2.62}$$

Equations (2.55)-(2.61) close one set of equations and we need to determine six functions $\tilde{A}_{f\sigma}$, $\tilde{A}_a$, $\tilde{A}_b$, $\Sigma_{f\sigma}$, Σ_b, Σ_a and one variable λ_0 self-consistently. Kroha and Wölfle (2001a) used the method stated above to solve the NCA equations for temperatures

down to $T \simeq 10^{-4} T_K$.

As an example, I calculated $A_d(\omega) = \mathrm{Im}G_d(\omega)/\pi$ for two different band shapes A_c, box DOS and semi-circular DOS, at different temperatures. Here, $2D$ is the band width. I choose $U = 2.4D$, and the particle-hole symmetry gives that $E_d = -U/2 = -1.2D$. This explains why the two side peaks locate separately at $\pm 1.2D$ in both Figures (Fig. 2.2 and Fig. 2.3).

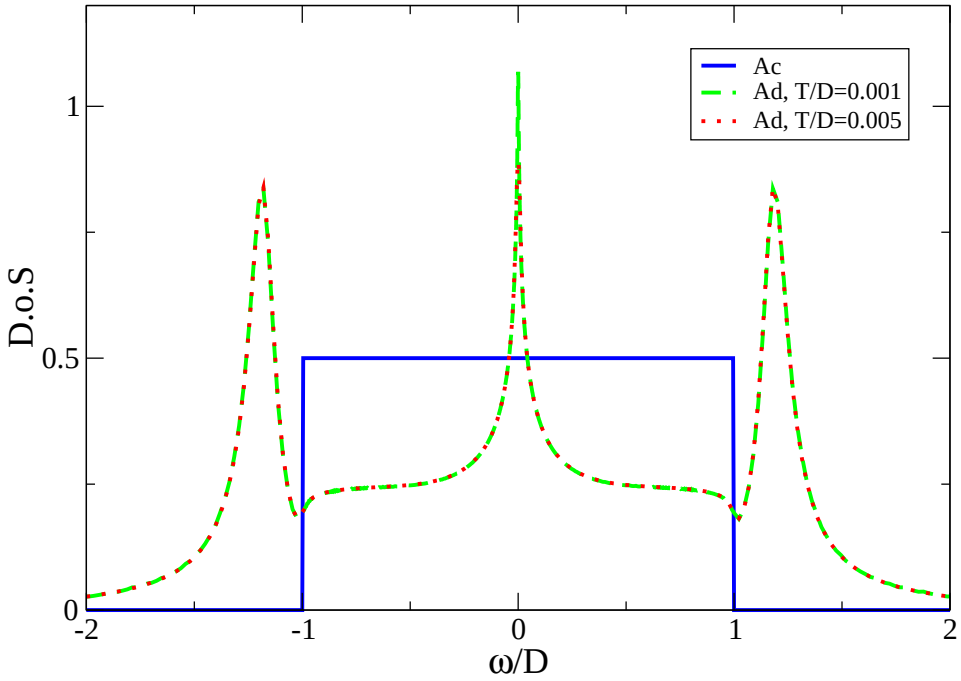

Figure 2.2.: Imaginary part of the impurity Green's function (green and red lines) within a box shaped band. The Kondo peak at $\omega = 0$ shows a critical dependence on temperature. The two side peaks will evolve into the lower and the upper Hubbard band in DMFT.

The pseudo-particle spectral functions are shown in Fig. 2.4. The slope of $\log_{10} \tilde{A}_f$ near 0 indicates the threshold exponents in Eq. (2.50).

Fig. 2.4 shows that $\tilde{A}_f$ has a peak near $\omega = 0$. The height of the peak grows as one approaches the insulating phase. The reason can be read off from Eq. (2.59). When a half-filled system switches to the insulating state, the possibility of a site to be occupied by one electron increases, which means the life-time of the pseudo-particle $\tau_{f\sigma}$ increases. This corresponds to a decreasing imaginary part of the self energy $\mathrm{Im}\Sigma_{f\sigma}$. Therefore, $\tilde{A}_f$ has a sharp peak whose position is determined by the equation $\omega + \lambda_0 - E_d - \mathrm{Re}\Sigma_{f\sigma}(\omega) = 0$. Since the function $\tilde{A}_f$ diverges near 0, a logarithmic grid as shown in Eq. (2.63) is required for calculating this function,

$$\omega_i = \frac{(2i - N)[\exp(\sigma \frac{|2i-N|}{N}) - 1]}{e^{\sigma}|2i - N|}. \tag{2.63}$$

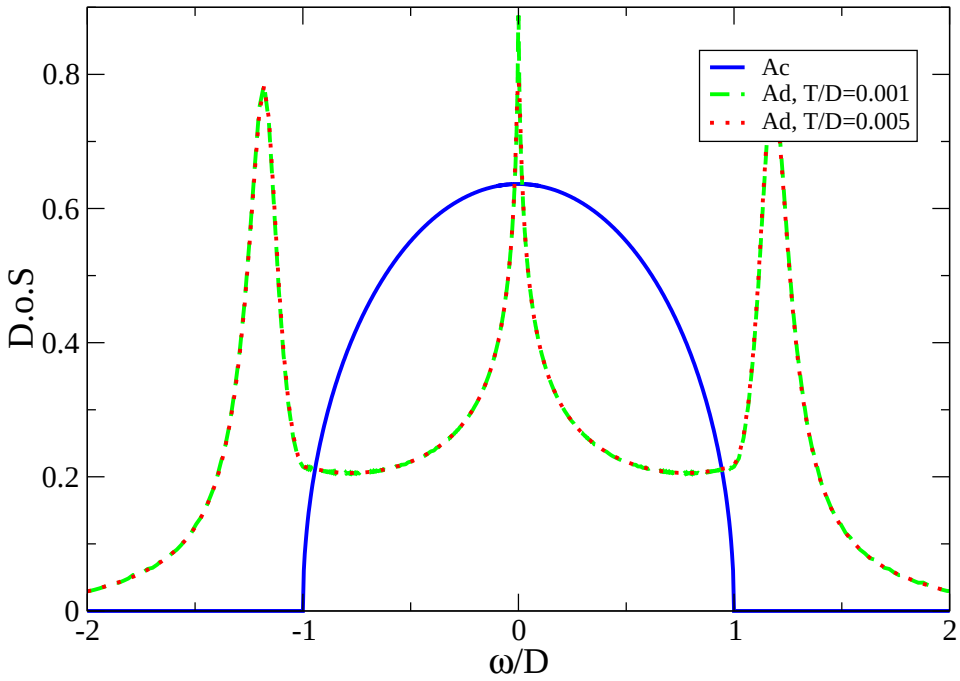

Figure 2.3.: $A_d(\omega)$ within a semi-circular shaped band.

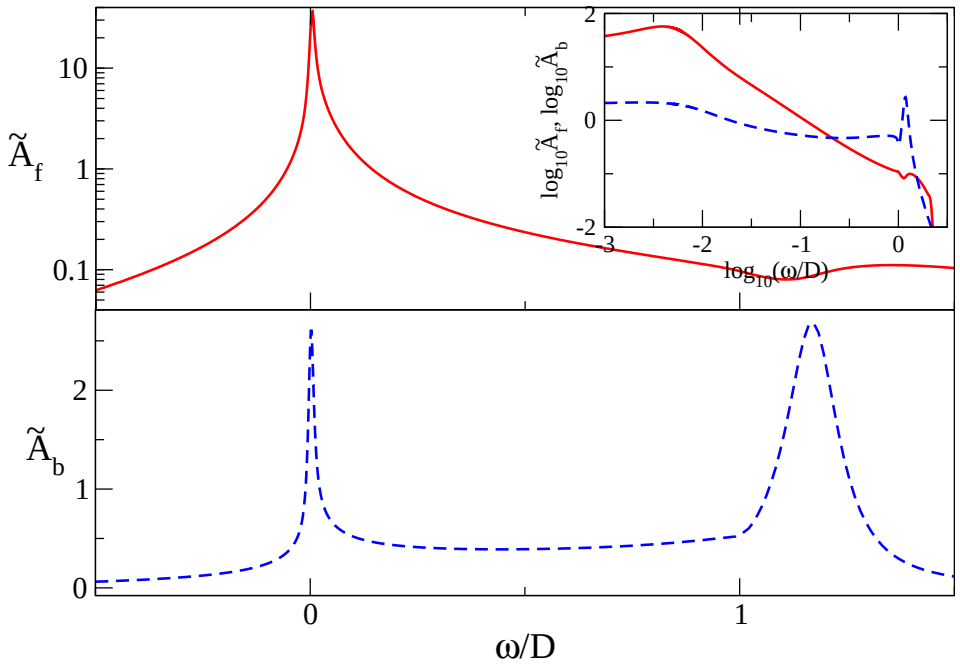

Figure 2.4.: Pseudo-particle spectral functions in semi-circle shaped band. Because of the particle hole symmetry, we have $E_a = 2E_d + U = 0$. The inset figure shows $\tilde{A}_f$ and $\tilde{A}_b$ in logscale. Kroha and Wölfle (2001b) pointed out that a broad peak of width $\sim \Gamma$ at $\omega \simeq |E_d|$ represents the hybridization of the impurity and the band. $\tilde{A}_f$ has a peak at $\omega \simeq T_k$.

In this chapter, we introduced the diagrammatic NCA technique as an impurity solver for the Anderson model. By absorbing the threshold behavior into the tilde function $\tilde{A}_\mu$, we solved the NCA equations for low temperatures. In the metal-insulator phase transition problem, this calculation is applicable.

Chapter 3.

Dynamical Mean Field Theory and Spatially Resolved DMFT

The difficulty in solving the metal-insulator transition of the Hubbard model lies in the fact that traditional perturbation theory can not treat both, the localization and the mobility at the same footing. In traditional perturbation theory, when $t \ll U$, we use t/U as a small perturbation, and obtain an insulating solution; when $U \ll t$, we employ U/t as a small expansion parameter and obtain the metallic solution. We can show that these two solutions are different, hence there must exist a phase transition. However, the coexistence of a metal and an insulator can not be resolved under this perturbation theory, because we only find one state, either metallic state or insulating , for the same parameters. The phase coexistence occurs at the intermediate U/t, where the perturbation method fails. This difficulty was solved in 1989, when Metzner and Vollhardt (1989b) pointed out the local nature of perturbation theory in $d = \infty$. When $d = \infty$, and the hopping parameter t is scaled as $t \to t/\sqrt{d}$, the contribution from two different vertices which are connected by three or more separate paths, are suppressed by a factor of $1/\sqrt{d}$. Therefore, only the on-site term in the self-energy diagram remains. This local property in $d = \infty$ tells us that the self-energy is position (or momentum) independent: $\Sigma_{ij}(i\omega) = \delta_{ij}\Sigma(i\omega)$. This is the key point in the DMFT theory. In this approach, spatial fluctuations are frozen, and the local quantum fluctuations in time are considered. Since this approach takes the $1/d$ (d is the lattice dimensionality) as the control parameter, this ensures that we can resolve the metal-insulating transition better than in perturbation theory in U/t or t/U. Because in the MIT, U/t is of the intermediate value, as discussed above.

3.1. Derivation of the DMFT Equation

We followed the derivation by Georges et al. (1996). The partition function of the Hubbard model Eq. (1.3) can be written as the path integral of Grassmann variables

$$Z = \int \prod_i D\, c^\dagger_{i\sigma} c_{i\sigma} \exp(-S), \tag{3.1}$$

$$S = \int_0^\beta d\tau [\sum_{i\sigma} c^\dagger_{i\sigma}(\tau)(\partial_\tau - \mu)c_{i\sigma}(\tau) - \sum_{ij,\sigma} t_{ij} c^\dagger_{i\sigma} c_{j\sigma} + U \sum_i n_{i\uparrow} n_{i\downarrow}]. \tag{3.2}$$

We choose one lattice site $i = o$ from the effective action Eq. (3.2) as S_o, and call the action without this site the cavity action $S^{(o)}$. So, the terms which are neither contained in S_o nor $S^{(o)}$ are called the interaction action ΔS. We replace S in Eq. (3.1) with $S = S_o + \Delta S + S^{(o)}$, then we have

$$Z = \int \prod_i D c^\dagger_{i\sigma} D c_{i\sigma} \exp(-S_o - \Delta S - S^{(o)}). \tag{3.3}$$

All these actions inside Eq. (3.3) read

$$S_o = \int_0^\beta d\tau [\sum_\sigma c^\dagger_{o\sigma}(\tau)(\partial_\tau - \mu)c_{o\sigma} + U\, n_{o\uparrow}(\tau) n_{o\downarrow}(\tau)], \tag{3.4}$$

$$\Delta S = -\int_0^\beta d\tau [\sum_{i\sigma} (t_{io} c^\dagger_{i\sigma} c_{o\sigma} + t_{oi} c^\dagger_{o\sigma} c_{i\sigma})], \tag{3.5}$$

and

$$S^{(o)} = \int_0^\beta d\tau [\sum_{i\neq o,\sigma} c^\dagger_{i\sigma}(\partial_\tau - \mu)c_{i\sigma} - \sum_{i,j\neq o,\sigma} t_{ij} c^\dagger_{i\sigma} c_{j\sigma} + U \sum_{i\neq o} n_{i\uparrow} n_{i\downarrow}]. \tag{3.6}$$

With the definition $\Delta S = \int d\tau \Delta S(\tau)$ and $\Delta S(\tau) = \sum_{i\sigma} [t_{io} c^\dagger_{i\sigma}(\tau) c_{o\sigma}(\tau) + t_{oi} c^\dagger_{o\sigma}(\tau) c_{i\sigma}(\tau)]$, we integrate over the degrees of freedom on all sites except site o in the partition function Eq. (3.3)

$$Z = \int D c^\dagger_{o\sigma} D c_{o\sigma} \exp(-S_o) \int \prod_{i\neq o} D c^\dagger_{i\sigma} D c_{i\sigma} \exp\left(-S^{(o)} - \int_0^\beta \Delta S(\tau) d\tau\right). \tag{3.7}$$

Now, we expand $\exp(-S^{(o)} - \int_0^\beta \Delta S(\tau) d\tau)$ in a series

$$\begin{aligned} Z = \int D c^\dagger_{o\sigma} D c_{o\sigma} \exp(-S_o) \int \prod_{i\neq o,\sigma} D c^\dagger_{i\sigma} D c_{i\sigma} \exp(-S^{(o)}) \times \\ \left(1 - \int_0^\beta \Delta S(\tau) d\tau + \frac{1}{2!} \int_0^\beta d\tau_1 d\tau_2 T_\tau \Delta S(\tau_1) \Delta S(\tau_2) + \dots\right). \end{aligned} \tag{3.8}$$

With the definition of $\langle X\rangle^{(o)} = (\int \prod_{i\neq o,\sigma} Dc^\dagger_{i\sigma} Dc_{i\sigma} \exp(-S^{(o)})X)/Z^{(o)}$, the partition function can be written as

$$Z = \int Dc^\dagger_{o\sigma} Dc_{o\sigma} \exp(-S_o) Z^{(o)} \left(1 - \int_0^\beta \langle \Delta S(\tau)\rangle^{(o)} d\tau + \frac{1}{2!}\int_0^\beta d\tau_1 d\tau_2 \langle T_\tau \Delta S(\tau_1)\Delta S(\tau_2)\rangle^{(o)} + \dots\right). \tag{3.9}$$

All the odd order terms vanish. The lowest order term reads

$$\begin{aligned}
&\frac{1}{2!}\int_0^\beta d\tau_1 d\tau_2 \langle T_\tau \sum_{i\sigma}\Big[t_{io}c^\dagger_{i\sigma}(\tau_1)c_{o\sigma}(\tau_1) + t_{oi}c^\dagger_{o\sigma}(\tau_1)c_{i\sigma}(\tau_1)\Big]\times \\
&\qquad \sum_{j\sigma}\Big[t_{jo}c^\dagger_{j\sigma}(\tau_2)c_{o\sigma}(\tau_2) + t_{oj}c^\dagger_{o\sigma}(\tau_2)c_{j\sigma}(\tau_2)\Big]\rangle^{(o)} = \\
&\int_0^\beta d\tau_1 d\tau_2 \sum_\sigma c^\dagger_{o\sigma}(\tau_1)\sum_{ij} t_{io}t_{oj}\langle T_\tau c_{i\sigma}(\tau_1)c^\dagger_{j\sigma}(\tau_2)\rangle^{(o)} c_{o\sigma}(\tau_2) = \\
&\qquad \int_0^\beta d\tau_1 d\tau_2 \sum_\sigma c^\dagger_{o\sigma}(\tau_1)\sum_{ij} t_{io}t_{oj}G^{(o)}_{ij}(\tau_1-\tau_2)c_{o\sigma}(\tau_2).
\end{aligned} \tag{3.10}$$

In deriving Eq. (3.10), we used the property

$$\int_0^\beta d\tau_1 \int_0^\beta d\tau_2 \langle T_\tau \sum_{ij,\sigma} t_{io}t_{jo}c^\dagger_{i\sigma}(\tau_1)c_{o\sigma}(\tau_1)c^\dagger_{o\sigma}(\tau_2)c_{j\sigma}(\tau_2)\rangle^{(o)} = \tag{3.11}$$

$$\int_0^\beta d\tau_1 \int_0^\beta d\tau_2 \langle T_\tau \sum_{ij,\sigma} t_{io}t_{jo}c^\dagger_{o\sigma}(\tau_1)c_{i\sigma}(\tau_1)c^\dagger_{j\sigma}(\tau_2)c_{o\sigma}(\tau_2)\rangle^{(o)} = \tag{3.12}$$

$$\int_0^\beta d\tau_1 \int_0^\beta d\tau_2 \sum_\sigma c^\dagger_{o\sigma}(\tau_1)\sum_{ij} t_{io}t_{oj}\langle T_\tau c_{i\sigma}(\tau_1)c^\dagger_{j\sigma}(\tau_2)\rangle^{(o)} c_{o\sigma}(\tau_2). \tag{3.13}$$

Eq. (3.13) is easily proved by demonstrating that when $\tau_1 > \tau_2$, Eq. (3.11) is equal to

$$\int_0^\beta d\tau_1 \int_0^{\tau_1} d\tau_2 \sum_\sigma c^\dagger_{o\sigma}(\tau_2)\sum_{ij} t_{io}t_{oj}\langle c_{j\sigma}(\tau_2)c^\dagger_{i\sigma}(\tau_1)\rangle^{(o)} c_{o\sigma}(\tau_1), \tag{3.14}$$

and when $\tau_2 > \tau_1$, Eq. (3.12) is equal to

$$\int_0^\beta d\tau_2 \int_0^{\tau_2} d\tau_2 \sum_\sigma c^\dagger_{o\sigma}(\tau_1)\sum_{ij} t_{io}t_{oj}\langle c_{j\sigma}(\tau_1)c^\dagger_{i\sigma}(\tau_2)\rangle^{(o)} c_{o\sigma}(\tau_2). \tag{3.15}$$

Since τ_1 and τ_2 are dummy variables, it's easy to show that Eq. (3.14) is equal to Eq. (3.15). Using the definition of effective action S_{eff}:

$$e^{-S_{eff}}/Z_{eff} = \int \prod_{i\neq o} Dc^{\dagger}_{i\sigma} Dc_{i\sigma} e^{-S}/Z, \tag{3.16}$$

we have

$$\begin{aligned} S_{eff} = \sum_{n=1}^{\infty} \sum_{i_1\cdots j_n} \int \eta^{\dagger}_{i_1}(\tau_{i_1})\cdots\eta^{\dagger}_{i_n}(\tau_{i_n})\eta_{j_1}(\tau_{j_1})\cdots\eta_{j_n}(\tau_{j_n}) \\ \times G^{(o)}_{i_1\cdots j_n}(\tau_{i_1}\cdots\tau_{i_n},\tau_{j_1}\cdots\tau_{j_n}) + S_o + const, \end{aligned} \tag{3.17}$$

where $\eta_i = t_{io}c_{i\sigma}$. As the large d limit requires us to scale the hopping $t_{ij} \to t_{ij}/\sqrt{d}^{|i-j|}$, the n-th term in Eq. (3.17) is of the order $d^2/d^{2n/2} = (1/d)^{n-2}$, so that only the $n = 2$ term survives when d is very large. For example, in the first term of Eq. (3.17), $G^{(o)}_{ij} \sim t^{|i-j|}$, therefore $G^{(o)}_{ij} \sim (1/d)^{|i-j|/2}$, the two sums give d^2, and the scale of $t_{io}t_{oj}$ gives $1/d$. So the first term is of the order 1. The second order term involves a connected four point Green's function $G^{(o)}_{ijkl}$. This function falls off as $1/(d^{|i-j|/2}d^{|i-k|/2}d^{|i-l|/2})$, the cavity property makes this term equal $1/d^3$. This term has a prefactor of t^4, which is of the order $1/d^2$. The sum $\sum_{ijkl}$ yields d^4. Considering all above, the second term is of the order of $1/d$. This term vanishes as $d \to \infty$. If we consider the term with $i = j \neq k, l$, the sum $\sum_{i=j\neq k,l}$ yields d^3. The prefactor contributes $1/d^2$, and since $G^{(o)}_{i=j,kl} \sim 1/d^2$, so the second term is also of the order $1/d$, which vanishes as $d \to \infty$. Since we have proved that only the one-particle Green's functions survive in the large-d limit, the effective action could be reduced to the interaction between the impurity and a dynamical field

$$\begin{aligned} S_{eff} = &-\int_0^{\beta} d\tau_1 \int_0^{\beta} d\tau_2 \sum_{\sigma} c^{\dagger}_{o\sigma}(\tau_1)\mathcal{G}_0^{-1}(\tau_1-\tau_2)c_{o\sigma}(\tau_2) + \\ &\int_0^{\beta} d\tau U\, n_{o\downarrow}(\tau)n_{o\uparrow}(\tau) \\ = S_o &+ \int_0^{\beta} d\tau_1 \int_0^{\beta} d\tau_2 \sum_{\sigma} c^{\dagger}_{o\sigma}(\tau_1) \sum_{ij} t_{io}t_{oj}G^{(o)}_{ij}(\tau_1-\tau_2), \end{aligned} \tag{3.18}$$

in which the Weiss field $\mathcal{G}_0^{-1}$ reads

$$\mathcal{G}_0^{-1}(\tau_1-\tau_2) = -(\partial_{\tau_1}-\mu)\delta_{\tau_1\tau_2} - \sum_{ij} t_{io}t_{oj}G^{(o)}_{ij}(\tau_1-\tau_2). \tag{3.19}$$

The effective Weiss field $\mathcal{G}_0(\tau_1 - \tau_2)$ describes the effective amplitude for a fermion created at time τ_1 and destroyed at time τ_2. This picture describes that the lattice site

o exchange particles with the effective bath. Eq. (3.19) tells us that the Weiss function $\mathcal{G}_0$ is related to the cavity Green's function $G_{ij}^{(o)}$. To obtain a closed set of equations, we should find the relation between the cavity Green's function $G_{ij}^{(o)}$ and the local Green's function G_{ij}. Hubbard (1964a) has derived this equation as

$$G_{ij}^{(o)} = G_{ij} - \frac{G_{io}G_{oj}}{G_{oo}}. \tag{3.20}$$

It is not difficult to understand Eq. (3.20). G_{ij} includes the paths which go through the cavity o, and also those which avoid the cavity o. The number of paths which go through o is proportional to $G_{io}G_{oj}$, and this quantity must be divided by G_{oo} to avoid counting twice the paths which originate from o and then return to the same site. With Eq. (3.19), we can prove that the self-energy is local. It's easy to find the Fourier transform of Eq. (3.19)

$$\mathcal{G}_0^{-1}(i\omega) = i\omega + \mu - \sum_{ij} t_{io}t_{oj}G_{ij}^{(o)}(i\omega). \tag{3.21}$$

Inserting Eq. (3.20) into Eq. (3.21), and using that

$$\sum_{ij} t_{io}t_{oj}G_{ij}(i\omega) = \int_{-\infty}^{\infty} d\epsilon \frac{\rho(\epsilon)\epsilon^2}{i\omega + \mu - \Sigma(i\omega) - \epsilon}, \tag{3.22}$$

we express the Weiss effective field as

$$\mathcal{G}_0^{-1}(i\omega) = \Sigma(i\omega) + G^{-1}(i\omega), \tag{3.23}$$

in which

$$G(i\omega) = \int_{-\infty}^{\infty} d\epsilon \frac{\rho(\epsilon)}{i\omega + \mu - \Sigma(i\omega) - \epsilon}. \tag{3.24}$$

To close these DMFT equations, we need to calculate $\Sigma(i\omega)$ from the Weiss field $\mathcal{G}_0(i\omega)$, which is done in the impurity solver. In deriving Eq. (3.23), we used the assumption that the self-energy is local (k-independent) $\Sigma_{ij}(i\omega) = \delta_{ij}\Sigma(i\omega)$. The local property can be proved by considering the diagrams in perturbation theory. In perturbation theory, $Un_{i\uparrow}n_{i\downarrow}$ is shown as a four-leg vertex i. The hopping term is scaled by $1/\sqrt{d}$, the path connecting i and j has a factor of $1/\sqrt{d}^{|i-j|}$. The summation on j should be calculated with fixed site i. This summation gives us a factor of $d^{|i-j|}$. Let $\mathcal{P}_{ij}$ be the number of paths connecting i and j, then we have the factor $d^{|i-j|}/\sqrt{d}^{|i-j|\mathcal{P}_{ij}}$. If $\mathcal{P}_{ij} > 2$, only diagrams with $i = j$ survive when $d \to \infty$. In momentum space, this property means that when two vertices can be "collapsed" according to this rule, the propagator $G^{(o)}(k, i\omega)$ which connects these two vertices can be replaced by the k-independent $\sum_k G^{(o)}(k, i\omega)$, which means we can "ignore" the momentum conservation at this vertex. Since the two vertices in a skeleton diagram can always be connected by more than two paths, all diagrams contributing to the self-energy can

be collapsed to a single-site. The Luttinger-Ward functional is the sum of all vacuum to vacuum diagrams. We have

$$\Phi = \sum_i \phi[G_{ii}],\ d \to \infty. \tag{3.25}$$

As we know the self-energy is the functional derivative of Φ:

$\Phi =$ 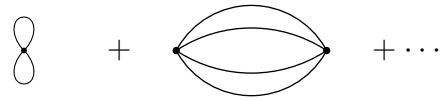 $+ \cdots$ (3.26)

$$\Sigma_{ij} = \frac{\delta \Phi}{\delta G_{ij}}. \tag{3.27}$$

Thus we have

$$\Sigma_{ij}(i\omega) = \delta_{ij}\Sigma(i\omega). \tag{3.28}$$

Eq. (3.28) is the *local property* theorem in DMFT.

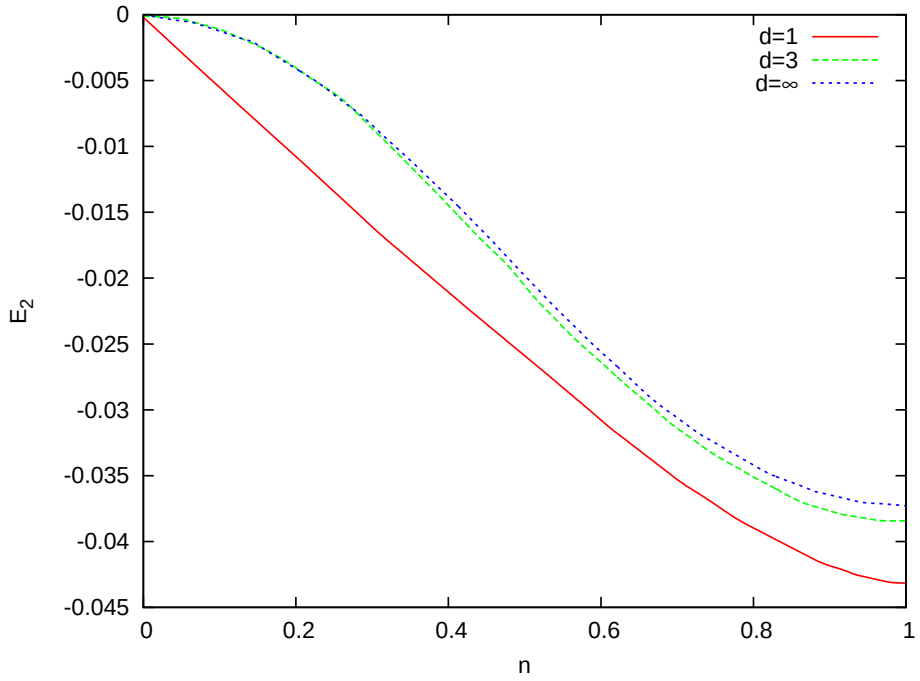

Figure 3.1.: Second-order correlation energy $E_2 \equiv E_2/[LU^2/|\epsilon_0(1/2,1/2)|]$. Figure taken from Metzner and Vollhardt (1989a)

From the derivation above, we know that the DMFT is an **exact** method in $d = \infty$, e.g. hypercubic and Bethe lattice in $d \to \infty$. For other systems of finite dimensions, the local property Eq. (3.28) could only be treated as an approximation. Metzner and

Vollhardt (1989a) calculated the second order energy correction

$$E_2 = \frac{LU^2}{(2\pi)^2} \int d\mathbf{k} d\mathbf{k}' \frac{n^0_{\mathbf{k}\uparrow} n^0_{\mathbf{k}'\downarrow} (1 - n^0_{\mathbf{k}+\mathbf{q}\uparrow})(1 - n^0_{\mathbf{k}'-\mathbf{q}\downarrow})}{\epsilon_{\mathbf{k}} + \epsilon_{\mathbf{k}'} - \epsilon_{\mathbf{k}+\mathbf{q}} - \epsilon_{\mathbf{k}'-\mathbf{q}}} \tag{3.29}$$

for $d = 1, 2, 3, \infty$ and they showed that the result for $d = \infty$ is very close to $d = 3$ (Fig. 3.1). Thus, we think the DMFT approximation is a good approximation for $d = 3$ systems.

3.2. NCA as an Impurity Solver in DMFT

From Section 3.1, we know that the key point in DMFT is to solve the impurity problem, that is to say, how to calculate Σ from $\mathcal{G}_0$. Popular impurity solvers are quantum Monte Carlo (QMC) method, exact diagonalization method, iterated perturbation theory (IPT) and NCA. The QMC method, for example, Hirsch and Fye (1986) algorithm, considers the impurity problem in discrete imaginary time, and the interaction Green's function is calculated by stochastic Monte Carlo sampling. The exact diagonalization method treats the Anderson impurity model as a Hamiltonian with finite orbitals, and this Hamiltonian can be diagonalized exactly using standard algorithms. IPT provides us an interpolation scheme between the weak-coupling and the strong-coupling limit (Georges et al., 1992; Zhang et al., 1993). NCA (Subsection 2.2.2) is also extensively applied in DMFT as an impurity solver, or sometimes as a default model supplementing of QMC. The early works of Kuramoto (1986, 1983); Kojima et al. (1984); Kuramoto and Kojima (1984) applied the NCA to the Anderson model, and later on, Pruschke et al. (1993) applied this method to the Hubbard model at infinite dimensions. Here we are going to apply the NCA method which is introduced in Subsection 2.2.2 to the DMFT impurity problem.

3.2.1. Weiss-Field Function of the Anderson Model

First, we follow the steps in Section 3.1, the action S of the Anderson model is expressed as in Eq. (3.30). We use the notation $d^\dagger/d$ as the operator on the impurity site instead of $c_o^\dagger/c_o$. Following the same steps as in Section 3.1, the action of Eq. (2.1) reads

$$S = \int_0^\beta d\tau \left\{ \sum_{\mathbf{k}\sigma} c^\dagger_{\mathbf{k}\sigma}(\partial_\tau - \mu + E_{\mathbf{k}}) c_{\mathbf{k}\sigma} + \sum_\sigma d^\dagger_\sigma(\partial_\tau + \varepsilon_d) d_\sigma + \right.$$
$$\left. \sum_{\mathbf{k}\sigma} V_{\mathbf{k}} (c^\dagger_{\mathbf{k}\sigma} d_\sigma + d^\dagger_\sigma c_{\mathbf{k}\sigma}) + U\, n_{d\uparrow} n_{d\downarrow} \right\}. \tag{3.30}$$

H_{AM} is quadratic in $c^\dagger_{\mathbf{k}}$ and $c_{\mathbf{k}}$, this variable can be integrated out in S. We write out the partition function Z as

$$Z = \int D[c^\dagger_{\mathbf{k}\sigma}, c_{\mathbf{k}\sigma}] \int D[d^\dagger_\sigma, d_\sigma] e^{-S} \tag{3.31}$$

$$= \underbrace{\int D[d^\dagger_\sigma, d_\sigma] \exp\left\{ -\int_0^\beta d\tau \left[d^\dagger_\sigma(\partial_\tau + \varepsilon_d) d_\sigma + U\, n_{d\downarrow} n_{d\uparrow} \right] \right\}}_{Z_d} \times$$

$$\underbrace{\int D[c^\dagger_{\mathbf{k}\sigma}, c_{\mathbf{k}\sigma}] \exp\left\{ -\int_0^\beta d\tau \left[\sum_{\mathbf{k}\sigma} c^\dagger_{\mathbf{k}\sigma}(\partial_\tau - \mu + E_{\mathbf{k}}) c_{\mathbf{k}\sigma} + V_{\mathbf{k}}(c^\dagger_{\mathbf{k}\sigma} d_\sigma + d^\dagger_\sigma c_{\mathbf{k}\sigma}) \right] \right\}}_{Z_c}. \tag{3.32}$$

The term Z_c can be simplified because it is an Gaussian integral,

$$Z_c = \exp\left[-\int_0^\beta d\tau\, d^\dagger_\sigma \left(\sum_{\mathbf{k}} V^2_{\mathbf{k}} \frac{1}{\partial_\tau - \mu + E_{\mathbf{k}}} \right) d_\sigma \right]. \tag{3.33}$$

Insert Eq. (3.33) into Eq. (3.32), we get the partition function

$$Z = \int D[d^\dagger_\sigma, d_\sigma] \exp\left\{ \underbrace{-\int_0^\beta d\tau \left[d^\dagger_\sigma \mathcal{G}_0^{-1} d_\sigma + U\, n_{d\uparrow} n_{d\downarrow} \right]}_{S_0} \right\}. \tag{3.34}$$

S_0 in Eq. (3.34) has the same form as Eq. (3.18), with

$$\mathcal{G}_0^{-1}(i\omega_n) = i\omega_n - \varepsilon_d - \int \frac{d\varepsilon}{\pi} \frac{\Delta(\varepsilon)}{i\omega_n - \varepsilon}, \tag{3.35}$$

where $\Delta(\varepsilon) = \pi \sum_k V_k^2 \delta(\varepsilon - E_k)$ is the DOS of the conduction band. The Weiss field function $\mathcal{G}_0$ is thus expressed by the conduction bath function.

3.2.2. DMFT Iterations and Analytical Results in $U = 0$ and $t_{ij} = 0$ Limit

Since the DMFT maps the Hubbard model onto the Anderson impurity model, in order to proceed solving DMFT equations, we need to solve Eq. (2.1) with a given bath $\Delta(\varepsilon)$. The iteration steps in solving DMFT equations are summarized as:

1. Calculate the lattice Green's function G with an initially guessed self energy Σ through Eq. (3.24).
2. Construct the effective field function $\mathcal{G}_0$ by using $\mathcal{G}_0^{-1} = \Sigma + G^{-1}$ (Eq. (3.23)).

3. Calculate the local Green's function G_d (or self energy Σ) with any given $\mathcal{G}_0$ by solving the Anderson impurity model.

4. Repeat all steps above until the solution reaches the desired accuracy.

In most cases, the DMFT equations should be solved self-consistently with numerical computing. But in the non-interacting limit and the atomic limit, the solutions to these equations are easy to obtain and we can get analytical results. In the non-interacting limit ($U = 0$), the self energy $\Sigma = 0$. Using Eq. (3.24), we got the lattice Green's function

$$G(i\omega) = \int_{-\infty}^{\infty} \frac{\rho(\varepsilon)d\varepsilon}{i\omega + \mu - \varepsilon}. \tag{3.36}$$

The DMFT equation Eq. (3.23) gives us $\mathcal{G}_0^{-1} = G^{-1}$. To calculate the updated self-energy with $\mathcal{G}_0$, we have $\Sigma \simeq U/2 + U^2 \int_0^\beta d\tau \hat{\mathcal{G}}_0^3$. This self-energy is always 0 for $U = 0$, which means the self-energy remains unchanged. The equation Eq. (3.36) is exactly the free on-site Green's function. This is the solution describing the metallic behavior.

In the atomic limit $t_{ij} = 0$, which also means that the interaction between the impurity and the bath $V_k = 0$, Eq. (3.35) yields $\mathcal{G}_0^{-1} = i\omega - \varepsilon_d$. The local Green's function $G = \langle T\, d^\dagger d \rangle_{S_{eff}}$ reads

$$G = \frac{1/2}{\mathcal{G}_0^{-1} - U} + \frac{1/2}{\mathcal{G}_0^{-1}}. \tag{3.37}$$

This describes the insulating solution like Eq. (1.6). The lower Hubbard band and the upper Hubbard band are separated by the distance of U.

3.2.3. DMFT with NCA

In most cases, the Anderson impurity model has to be solved by numerical methods. As the quantum impurity models have already been studied for over fifty years, many methods can be used to solve this problem. Here we apply the NCA to the Anderson impurity model.

In Subsection 2.2.2 we use the subscript c to denote the conduction band functions, thus Eq. (3.35) is equivalently written as

$$\mathcal{G}_0^{-1}(i\omega) = i\omega + \mu - V^2 G_c(i\omega). \tag{3.38}$$

As we know that the Weiss function can also be expressed as $\mathcal{G}_0^{-1} = \Sigma + G_{loc}^{-1}$ (Eq. (3.23)), we can write out the momentum dependent Green's function immediately

$$G_k(i\omega) = \frac{1}{V^2 G_c + G_{loc}^{-1} - \varepsilon_k}. \tag{3.39}$$

The local Green's function should be equal to the lattice Green's function. Then we

have the DMFT equation

$$G_{loc} = \int \frac{\rho(\varepsilon)d\varepsilon}{G_{loc}^{-1} + V^2 G_c - \varepsilon}. \tag{3.40}$$

Here, $\rho(\varepsilon)$ is the non-interacting DOS, and is determined by the hopping t and the structure of the crystal. This is one important property in DMFT theory. *The dimension of the model affects the result only through the non-interacting DOS*. The iterations of DMFT in Subsection 3.2.2 could be modified a little, because we don't calculate $\mathcal{G}_0$ and Σ directly. The new iterations look like this:

1. We start with a guessed bath Green's function G_c.
2. We solve the Anderson Model with NCA and then get $G_{loc} = G_d$.
3. Inserting G_c and G_{loc} into Eq. (3.40), we get a new local Green's function. Let us call it $G_{loc}^{(n)}$ for the n-th iteration.
4. Using $V^2 G_c^{(n)} + (G_{loc}^{(n)})^{-1} = V^2 G_c^{(n-1)} + (G_{loc}^{(n-1)})^{-1}$, we get a new bath Green's function $G_c^{(n)}$.
5. Replace $G_c^{(n-1)}$ with $G_c^{(n)}$, and go to step 2. The iteration continues until the difference $|G_c^{(n-1)} - G_c^{(n)}|$ reaches the desired accuracy limit.

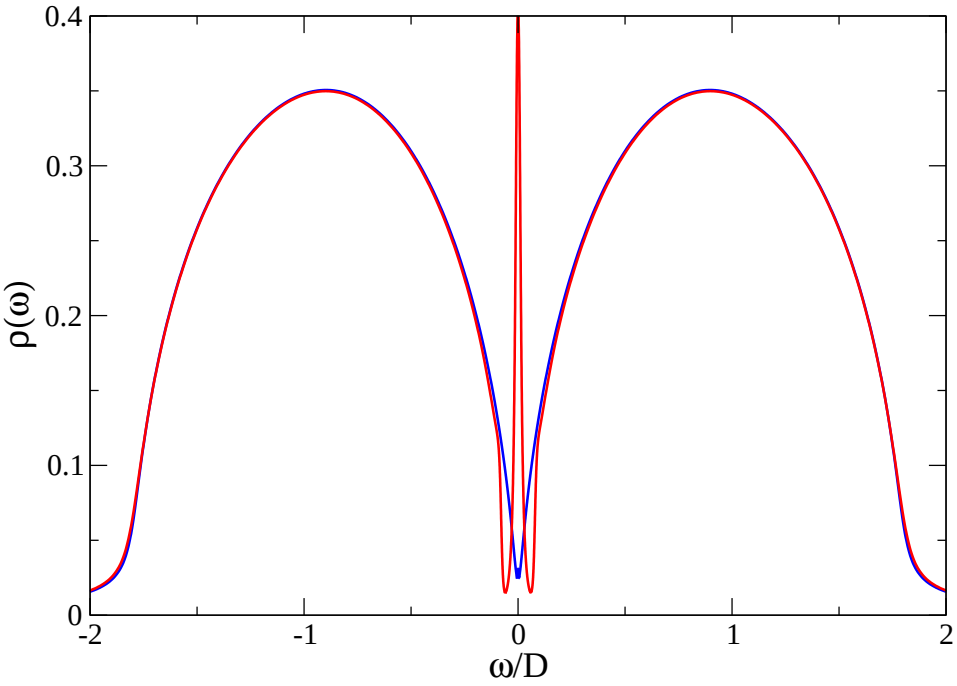

Figure 3.2.: Metal and insulator coexistence. In the phase coexistence region, at a specified U and T, the metallic (the red curve) and insulating (the blue curve) solution coexists.

We know that the bath DOS at the Fermi surface affects the transport behavior. The Kondo resonance peak at the Fermi surface indicates the metallic phase, as shown in Fig. 3.2. The blue curve has a gap at the Fermi energy, which indicates the insulating phase.

If we increase U/D in a system at the fixed temperature, the DOS at the Fermi surface will first slowly decrease. Then, when U is greater than the critical U_{c2}, the DOS jumps to a very low value, which indicates the Metal-Insulator phase transition. The interaction U drives the system from metal to insulator or vice versa. We call this kind of MIT as interaction induced MIT. Fig. 3.3 shows the DOS on Fermi surface increases as U/D decreases. At $U_{c1}/D = 1.590$, it transits from the insulating state to the metallic state.

If we keep U fixed, we can get the MIT by tuning T. This is called the temperature induced MIT.

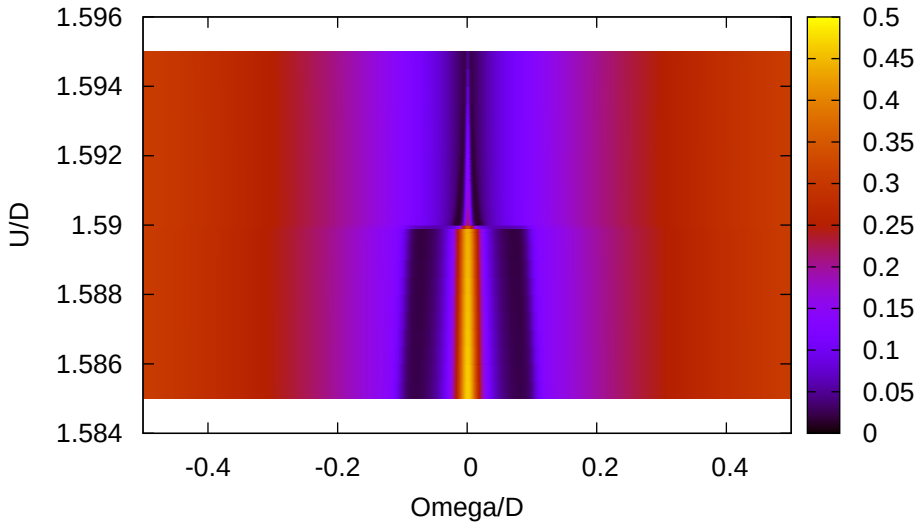

Figure 3.3.: Bath DOS at different U/D and ω/D. $T/D = 0.005$. The DOS is calculated from $U/D = 1.595$ to $U/D = 1.585$. By decreasing U, we get the first order phase transition point at this temperature is about $U_{c1}/D = 1.590$.

3.3. Spatially Resolved DMFT Theory

If there exists a phase coexistence region, a domain wall is set up between two different phases. Suppose we have a bulk metal and a bulk insulator when T and U are the same, what will happen if we bring this bulk metal and the bulk insulator in a very good connection, like a hetero-structure? Of course, we believe that nothing

will happen deep inside the bulk materials, but the DOS on the two contact-sides must change somehow. This is the formation of domain wall. And as the domain wall forms, the free energy on the domain wall also changes. To study this domain wall formation, we apply a spatially resolved DMFT theory. With this theory, we can calculate the spatially resolved DOS. And we can draw a picture of the domain wall in position space.

3.3.1. Derivation of Spatially Resolved DMFT

We start from the non-interacting 3-d Hamilton

$$H = \sum_{i\alpha,j\beta} t_{i\alpha,j\beta} c^\dagger_{i\alpha} c_{j\beta}, \tag{3.41}$$

where i, j are the xy plane indices, and α, β are the layer indices in the z-direction. We apply the Fourier transform in the xy plane $c^\dagger_{i\alpha} = \sum_{k\parallel} \exp(i\, k_\parallel r_{i\alpha}) c^\dagger_{k\parallel\alpha}$ to Eq. (3.41), and the Hamiltonian is written as

$$H = \sum_{i\alpha K\, K'\delta} t_{i\alpha,i\alpha+\delta} e^{i(K-K')\cdot r_{i\alpha}} e^{-iK'\cdot\delta} c^\dagger_{K,\alpha} c_{K',\alpha+\delta_z}, \tag{3.42}$$

where $K \equiv k_\parallel$ is the momentum in xy plane, δ is a unit vector in x, y or z direction.

According to the direction of δ, the Hamiltonian can be divided into two parts:

$$H_\parallel = \sum_K \varepsilon(K) c^\dagger_{K,\alpha} c_{K,\alpha},\ (\delta_z = 0) \tag{3.43}$$

and

$$H_\perp = \sum_{K,\delta_z=\pm 1} t_\perp c^\dagger_{K,\alpha} c_{K,\alpha+\delta_z},\ (\delta_{x,y} = 0) \tag{3.44}$$

where $\varepsilon(K) = 2t_{NN}[\cos(K_x) + \cos(K_y)]$, and t_{NN} indicates the nearest-neighbor hopping in the xy plane, $t_\perp$ is the inter-layer hopping term. Combining Eq. (3.43) and Eq. (3.44) together, the original Hamiltonian Eq. (3.41) can be written in a matrix form

$$H = C^\dagger_K \begin{pmatrix} \varepsilon(K) & t_\perp & & \\ t_\perp & \varepsilon(K) & t_\perp & \\ & t_\perp & \varepsilon(K) & \ddots \\ & & \ddots & \ddots \end{pmatrix} C_K, \tag{3.45}$$

where $C^\dagger_K = \begin{pmatrix} c^\dagger_{K,1} & c^\dagger_{K,2} & \cdots & c^\dagger_{K,n} \end{pmatrix}$. With this Hamiltonian, we can write down the Green's function in operator form immediately

$$G(i\omega) = (i\omega - H)^{-1}, \tag{3.46}$$

where H is the matrix form of the Hamiltonian in Eq. (3.45).

We will use the effective medium interpretation (Janiš, 1991; Janiš and Vollhardt, 1992a,b) of the DMFT to derive the Layer-DMFT. In this approach, we replace the interacting lattice model with a non-interacting medium plus a local self-energy Σ. The action of this effective medium is written as

$$S_{med} = -\int d\tau \int d\tau' \sum_{\mathbf{k}\sigma} c^{\dagger}_{\mathbf{k}\sigma} G^{-1}_{med} c_{\mathbf{k}\sigma}, \tag{3.47}$$

where

$$G^{-1}_{med}(\mathbf{k},\omega) = \begin{pmatrix} \omega+\mu-\Sigma_1(\omega)-\varepsilon(\mathbf{k}) & t_\perp & \\ t_\perp & \omega+\mu-\Sigma_2(\omega)-\varepsilon(\mathbf{k}) & \ddots \\ & \ddots & \ddots \end{pmatrix}. \tag{3.48}$$

The summation of $\mathbf{k}$ is performed in the xy plane and $\Sigma_\alpha\,(\alpha = 1,\ldots,n)$ is layer dependent. n is the number of layers.

Now, we switching on the local interaction $U\,n_{o\uparrow}n_{o\downarrow}$ and removing the self-energy on the site o, we have a model with the impurity embedded as

$$S_{emb} = S_{med} + U\int n_{o\uparrow}n_{o\downarrow}d\tau \times I - \int d\tau d\tau' \sum_{\sigma} C^{\dagger}_{o\sigma}\Sigma\, C_{o\sigma}, \tag{3.49}$$

where I is the unit matrix, the self-energy is also in matrix form and $C_{o\sigma}$ is a vector whose elements are $c_{o\alpha\sigma}\,(\alpha = 1,\ldots,n)$.

Comparing S_{emb} with the S_{eff} in Eq. (3.18), it is easy to write the Weiss field function as

$$\mathcal{G}_0^{-1} = G_d^{-1} + \Sigma, \tag{3.50}$$

where

$$G_d \equiv \int d\varepsilon \rho^{2d}(\varepsilon) \begin{pmatrix} i\omega+\mu-\Sigma_1-\varepsilon & t & \\ t & \ddots & \ddots \\ & \ddots & \ddots \end{pmatrix}^{-1}. \tag{3.51}$$

(3.50) looks the same as (3.23), we should notice that in Eq. (3.50) all the Green's functions and self-energies are in matrix form.

We follow the steps in Subsection 3.2.3 to calculate the local Green's function G_d or G_c in matrix form. Because the self-energy is layer dependent and momentum independent, it is easy to realize the paralleled computing on clusters.

3.3.2. 3-d Non-Interacting DOS

If we switch off the interaction, we have $\Sigma_\alpha = 0$. Then Eq. (3.51) gives us the 3-d non-interacting DOS. This property can be used to prove the validity of this layer

formalism of the Green's function, because the 3-d non-interacting DOS can be calculated analytically.

Suppose, the 2-d DOS is a flat band

$$\rho^{2d}(\varepsilon_{2d}) = \begin{cases} \frac{3D}{4} & |\varepsilon_{2d}| \leq \frac{2D}{3} \\ 0 & |\varepsilon_{2d}| > \frac{2D}{3}, \end{cases} \tag{3.52}$$

where D is the half-bandwidth, we could calculate the 3-d DOS from the definition. We know that the energy in 3-d structure can be divided into the 2-d energy and the 1-d energy:

$$\varepsilon = \varepsilon_{2d}(k_{\|}) + 2t\cos k_z, \tag{3.53}$$

where $k_z = z\pi/n$, $z = 1, \ldots, n$. From the definition of DOS, we have

$$\rho^{3d}(\varepsilon) = dN/d\varepsilon = \frac{1}{n}\sum_{z=1}^{n} \rho^{2d}(\varepsilon - 2t\cos\frac{z\pi}{n}). \tag{3.54}$$

This expression describes the 3-d DOS with finite layer number n. And ρ^{3d} should converge to the bulk 3-d DOS ρ^{3d}_{Bulk} when $n \to \infty$,

$$\rho^{3d}_{Bulk}(\varepsilon) = \begin{cases} 3/4D & |\varepsilon| < D/3 \\ (1 - \frac{\arccos((2D-3\varepsilon)/D)}{\pi}) \times \frac{3}{4D} & D/3 \leq \varepsilon \leq D \\ \frac{\arccos((-2D-3\varepsilon)/D)}{\pi} \times \frac{3}{4D} & -D \leq \varepsilon \leq -D/3 \\ 0 & |\varepsilon| > D. \end{cases} \tag{3.55}$$

We have calculated the 3-d DOS from the band structure and the definition of the DOS in the above Eq. (3.55). Now, we can calculate this DOS again from the matrix formulation of the Green's function. From Eq. (3.51), we have

$$G_d(i\omega \to \omega - i\delta) = \int d\varepsilon \rho^{2d}(\varepsilon) \begin{pmatrix} \omega - \varepsilon - i\delta & t & & \\ t & \ddots & \ddots & \\ & \ddots & \ddots & \end{pmatrix}^{-1}. \tag{3.56}$$

With the knowledge of linear algebra, we can find the eigenvectors q_j of a $n \times n$ matrix M, and form them into a matrix $Q = (q_1, q_2, \ldots, q_n)$. We have $M = Q\lambda Q^{-1}$, where λ is a diagonal matrix with λ_{jj} the eigenvalue corresponding to q_j. If we choose

$$M = \begin{pmatrix} 0 & t & & \\ t & \ddots & \ddots & \\ & \ddots & \ddots & \end{pmatrix} = Q\lambda Q^{-1}, \tag{3.57}$$

we can write G_d as

$$G_d(\omega - i\delta) = \int \frac{\rho^{2d}(\varepsilon)d\varepsilon}{Q\lambda Q^{-1} + Q(\omega - \varepsilon - i\delta)IQ^{-1}} \tag{3.58}$$

$$= \int \frac{\rho^{2d}(\varepsilon)d\varepsilon}{Q\left[\lambda + (\omega - \varepsilon - i\delta)I\right]Q^{-1}} \tag{3.59}$$

$$= Q\left[\int \frac{\rho^{2d}(\varepsilon)d\varepsilon}{\lambda + (\omega - \varepsilon - i\delta)I}\right]Q^{-1} \tag{3.60}$$

where I is $n \times n$ unity matrix, and Q can be excluded from the integration because Q is ε-independent. As $\rho^{3d}(\omega) = \mathrm{Im}G_d/\pi$, we have

$$\rho^{3d}(\omega) = Q \begin{pmatrix} \rho^{2d}(\lambda_{11} + \omega) & & \\ & \ddots & \\ & & \rho^{2d}(\lambda_{nn} + \omega) \end{pmatrix} Q^{-1}. \tag{3.61}$$

Since ρ^{2d} is defined in (3.52) to be either $3/4D$ or 0, the ij-th element of ρ^{3d} reads $\rho^{3d}_{ij} = \sum_{kl} Q_{ik}\hat{\rho}_{kl}(Q^{-1})_{lj} = \sum_k Q_{ik}\hat{\rho}_{kk}(Q^{-1})_{kj}$. We could write ρ^{3d} as

$$\rho^{3d}(\omega) = \frac{1}{n} \begin{pmatrix} \sum_{i=1}^n \rho^{2d}(\lambda_{ii} + \omega) & & \\ & \ddots & \\ & & \sum_{i=1}^n \rho^{2d}(\lambda_{ii} + \omega) \end{pmatrix}. \tag{3.62}$$

The index of the elements indicates the layer. We find that the DOS on every layer has the same value in (3.62). Since we are studying the homogeneous non-interacting bath, the DOS on each layer must be the same. Therefore, the DOS of the 3-d bulk reads

$$\rho^{3d}(\omega) = \frac{1}{n}\sum_{i=1}^{n} \rho^{2d}(\lambda_{ii} + \omega). \tag{3.63}$$

It's not difficult to see that Eq. (3.54) and Eq. (3.63) have the same form. If we can prove that $\lambda_{ii} = -2t\cos\frac{i\pi}{n}$, we can make sure that the matrix formalism can correctly describe the layer structure of a bulk material. The proof of $\lambda_{ii} = -2t\cos\frac{i\pi}{n}$ is shown in Appendix A.

Fig. 3.4 shows the structure of the 3-d DOS calculated from Eq. (3.54) and Eq. (3.63). As a comparison, we also draw the 3-d DOS of a simple cubic lattice with only nearest neighbour hopping term in the same figure. In the following calculations, we will use the DOS from Eq. (3.63) because the integration of a flat 2-d band is easy to calculate. On the other hand, the 2-d simple cubic lattice DOS diverges at $\varepsilon = 0$, which makes the integration very difficult to carry out. In order to calculate 3-d DOS within the matrix Green's function, we have used $M = Q\lambda Q^{-1}$ to simplify the energy integration, because by this way we need to do the matrix inversion only *once*. This process is also very useful when we calculate the 3-d Green's function when $\Sigma \neq 0$. In that

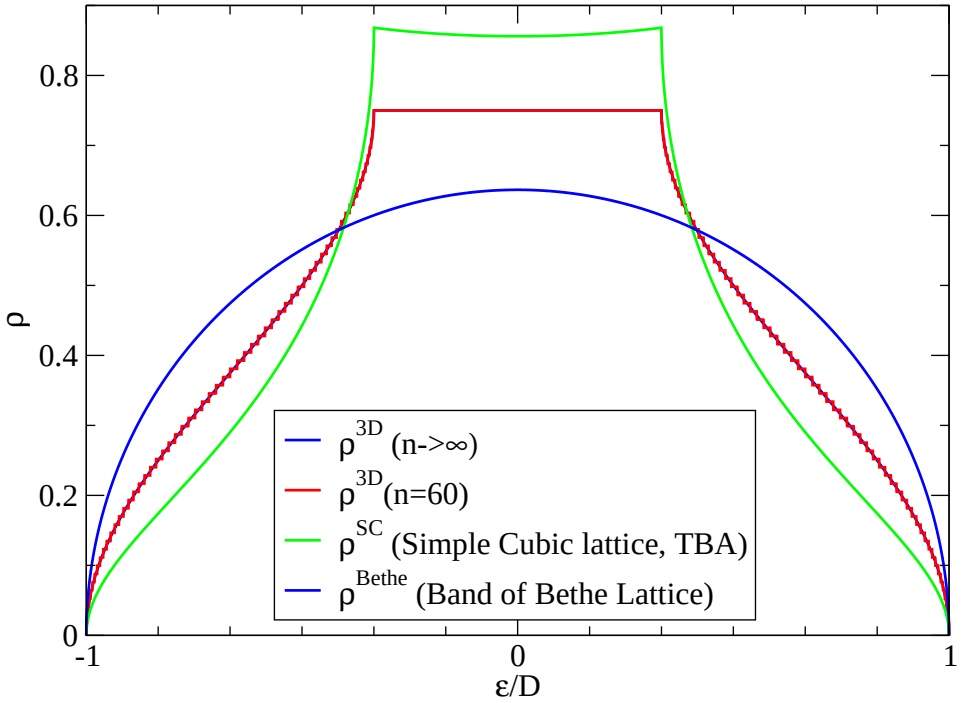

Figure 3.4.: The red and blue ρ^{3D} lines show the 3-d DOS calculated from a flat 2D band (using Eq. (3.52), and n is the number of layers.). The green line shows the DOS of a SC lattice with only nearest neighbour hopping term. ρ^{Bethe} is the DOS of a Bethe lattice. Bethe lattice DOS will be introduced in Section 4.3.

case, the self energy should be included in the matrix M. And λ therefore should be composed by complex numbers.

Chapter 4.

The First Order Metal-Insulator Phase Transition

The two important parameters in the Hubbard model are the electron correlation strength U/t and the filling of the band n. We can divide the MIT in the Hubbard model into two types. One is the interaction induced MIT, which is also called the *bandwidth controlled* (BC)-MIT or the Mott transition. In a BC-MIT, the metal-insulator transition is driven by tuning the correlation strength U/t. As Mott (1956, 1990) has argued, the carrier density decreases with increasing U/t. Thus, the screening of the long range Coulomb interaction becomes weak, which makes the formation of electron-hole pairs possible. This results in a first order metal-insulator transition. The other MIT type is the *filling controlled* (FC)-MIT, which means that different particle fillings n lead to different phases. In most cases, the filling at a non-integer n leads to the metallic phase. In the large U/t region, the filling of $n = 0, 1, 2$ always leads to the insulating phase. The FC-MIT can be understood within the band theory. The integer filling n always indicates that the band is either totally filled or totally empty. In this situation, the DOS on the Fermi surface is 0. Therefore, it is the insulating phase. When $n = 1$, the insulator-metal phase transition can be achieved by changing U/t. In this chapter, we concentrate on this kind of MIT. The phase transition in this case does not break the translational symmetry of the lattice. Thus, the strong electron correlations must be considered in this phase transition. This has been an interesting problem since Mott made the first step towards understanding the electron correlations in insulator about 60 years ago (Mott, 1949). Using the DMFT method, Rozenberg et al. (1992, 1995) also demonstrated that the Mott-Hubbard MIT at finite temperature is a first-order phase transition. They have also calculated the phase diagram for this kind of phase transition. In this chapter, we give first a short introduction to the Ginzburg-Landau theory for the first-order phase transition. Later on, we will show the phase diagram obtained with our method.

4.1. The Ginzburg-Landau Theory for the First Order Phase Transition

In statistical mechanics, we have learned that at the phase transition the chemical potentials, and, therefore, the free energy, must change continuously. The derivatives of the free energy can be used to identify the order of the phase transition. A discontinuous free energy derivative indicates a first order phase transition. Ginzburg and Landau (Landau and Lifshitz, 1980, page 456) proposed a theory to explain the phase transition with the symmetry breaking of the system. In a first order phase transition, the order parameter changes discontinuously as one crosses the coexistence curve. We are going to show this within the Ginzburg-Landau theory.

Here we consider only the MIT. We choose the DOS at the Fermi surface $\rho(0)$ to be the order parameter η. The free energy is a function of U and T. We expand the free energy in the insulating phase, thus we have

$$F(U,\, T,\, \eta) = F_0(U,\, T) + \alpha_2\eta^2 + \alpha_3\eta^3 + \alpha_4\eta^4 + \cdots . \tag{4.1}$$

We have dropped the first term of first order in η in Eq. 4.1, because this term only results in a nonzero value of the minima of η, which is irrelevant in our study. To further simplify our model, we set $F_0 = 0$, which does not change the shape of the free energy curve. All parameters α_n are functions of U and T.

The extrema of the free energy are found by solving $\partial F/\partial\eta = 0$, which yields $\eta_1 = 0$ and $\eta_{2,3} = (-3\alpha_3 \pm \sqrt{9\alpha_3^2 - 32\alpha_2\alpha_4})/8\alpha_4$. We define $\Delta = 9\alpha_3^2 - 32\alpha_2\alpha_4$. If $\Delta < 0$, the $\eta_{2,3}$ solutions are not real numbers, therefore, we have only one valid solution $\eta_1 = 0$, which shows that the system is in the insulating state. When $\Delta > 0$, there exist two minima and one maximum. Since we have chosen the point $\eta_1 = 0$ as one minimum of F, we must have $\alpha_2 > 0$. Because η is the DOS at the Fermi surface, $\eta > 0$ must be assured. The easiest way to assure this is to set $\alpha_3 < 0$, and $\alpha_4 > 0$. We know that $F(\eta)$ has a maximum at either η_2 or η_3, so we can pick out the minima solution by demanding $\partial^2 F/\partial\eta^2 > 0$. Thus, F has another minimum at $\eta_2 = (-3\alpha_3 + \sqrt{\Delta})/8\alpha_4$. When $F(\eta_2) > F(\eta_1) = 0$, this is a metastable state, and when $F(\eta_2) < F(\eta_1)$, this solution describes a stable state. The first order transition happens when $F(\eta_2) = F(\eta_1)$. There, the insulating state can transit into the metallic state and vice versa without costing any energy.

Fig. 4.1 shows the free energy behavior for different α_3. Since we can change α_3 by changing U or T, this figure also provides an example which shows the free energy for different U or T. A phase transition is of first order, if the derivative $\partial F/\partial Y$ with $Y = U, T$ shows a discontinuity at the phase transition point. From Eq. (4.1) and within the condition that α_2 and α_4 are constant, we can derive $\partial F/\partial T = \eta^2\partial\alpha_3/\partial T$. For $\alpha_3 > -8.4852$, the system is in the insulating state where $\eta_{minimum} = 0$. For $\alpha_3 < -8.4852$, the system is in the metallic state where $\eta_{minimum} \neq 0$. Thus, at the phase transition point $\alpha_3 = -8.4852$, we find that $\partial F/\partial T$ jumps from 0 to a nonzero value. This is a typical first order phase transition.

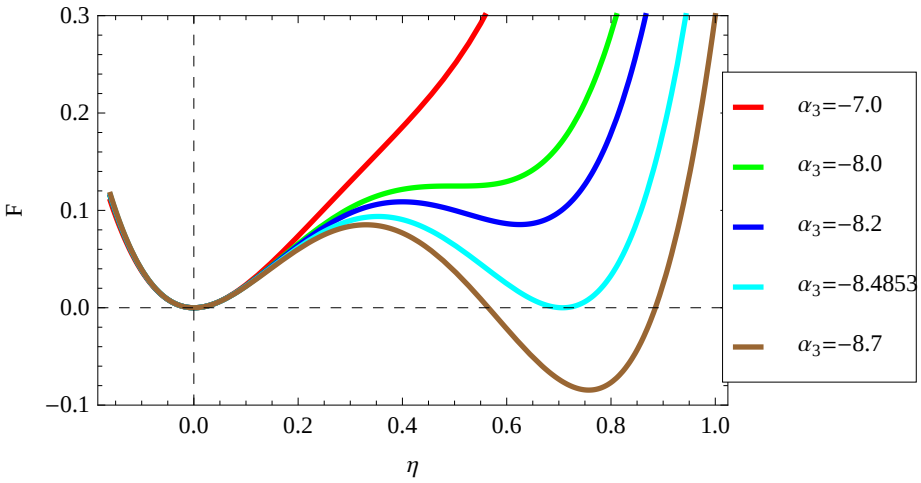

Figure 4.1.: The behavior of the free energy $F(\eta) = \alpha_2\eta + \alpha_3\eta^2 + \alpha_4\eta^3$, at $\alpha_2 = 3$ and $\alpha_4 = 6$. For $\Delta|_{\alpha_3=-7} < 0$, $F(\eta)$ has only one minimum at $\eta = 0$. For $\Delta|_{\alpha_3=-8.0} = 0$, $\partial F(\eta)/\partial\eta = 0$ has two solutions. The non trivial solution at $\eta = -3\alpha_3/8\alpha_4$, which is the location of the boundary of the phase coexistence region. When we come into this coexistence region, we can find two states (Metallic and Insulating states) coexisting. $\alpha_3 < -8.0$ indicates this coexistence region. For $\alpha_3 = -8.4853$, we find the insulating state has the same free energy as the metallic state. If we decrease α_3 from -8.2 to -8.7, the physical ground state changes from insulating state to the metallic state. Therefore, this free energy $F(\eta)$ describes a first order phase transition.

In this section, we have studied the first-order phase transitions in the Ginzburg-Landau theory. We started from the insulating state, and by tuning $\alpha_3(U,T)$ we showed that Eq. (4.1) contains a solution of a metallic state. This metallic state can become a stable state when α_3 is smaller than the first-order phase transition value. With Eq. 4.1, we could only show that the metallic state can exist simultaneously with the insulating state, but we can not show that the metallic state can exist by itself. This is because we expanded the free energy around $\eta = 0$, which means that the insulating state must exist. If we would do this series expansion at the metallic state by setting $\eta = \eta - \eta_{Metallic}$ and try to find a minimum in the range of $\eta < 0$, we could show that the insulating state can disappear in a certain range of values for α_3.

4.2. The Free Energy Behavior in the Metal-Insulator Phase Transition within the DMFT Theory

In Section 4.1, we have shown that the GL equation can be used to explain the metal-insulator phase transition. Since we are going to use the DMFT theory and the NCA as impurity solver to resolve this metal-insulator phase transition, it is very necessary to show that DMFT+NCA can reproduce this free energy behavior, which at the same time means that this treatment applied to the Hubbard model really yields the first order M-I phase transition. Brandt and Mielsch (1991) calculated the free energy of

the Falicov-Kimball model. In their calculations, they have established the relation between the lattice free energy F and the impurity free energy Ω_{imp}. Here, we are going to follow these steps and derive a relation between the average free energy and local Green's functions.

First, we know that the grand canonical potential Ω can be expressed by the partition function Z:

$$\Omega = -T \ln Z. \tag{4.2}$$

The band electron's Green's function can be written as functional derivative (Brandt and Mielsch, 1991)

$$G_{ij}(\tau, \tau'; \mathcal{G}_0^{-1}) = \frac{\delta W}{\delta \mathcal{G}_0^{-1}}, \tag{4.3}$$

where

$$W = \Phi - \mathrm{Tr}(\Sigma G) + \mathrm{Tr}(\ln G). \tag{4.4}$$

As we have discussed in Section 3.1, Φ is the generating functional for the self energy Eq. (3.27). The second term on the right hand side, $\mathrm{Tr}(\Sigma G)$ is defined as

$$\mathrm{Tr}(\Sigma G) = \sum_{i,j} \int_0^\beta d\tau \int_0^\beta d\tau' \Sigma_{ij}(\tau, \tau') G_{ji}(\tau', \tau), \tag{4.5}$$

and the last term on the right hand side of Eq. (4.4) is

$$\frac{\delta \mathrm{Tr}(\ln G)}{\delta G_{ji}} = -(G^{-1})_{ij}. \tag{4.6}$$

We can replace W with $-\ln Z$ by setting those free constants in a proper way, then we have

$$-\ln Z = \Phi - \mathrm{Tr}(\Sigma G) + \mathrm{Tr} \ln G. \tag{4.7}$$

With the same method, we can get the expression for the impurity

$$-\ln Z_{imp} = \Phi_{imp} - \mathrm{Tr}(\Sigma_{imp} G_{imp}) + \mathrm{Tr} \ln G_{imp}. \tag{4.8}$$

We multiply T to both sides of Eq. 4.7 and Eq. 4.8 and eliminate the functional Φ in these two equations, obtaining the expression for free energy

$$\begin{aligned} \frac{\Omega}{N} = \Omega_{imp} - T \sum_{n\sigma} \Big(\int d\varepsilon \rho(\varepsilon) \\ \times [\ln(i\omega_n + \mu - \Sigma_\sigma(i\omega) - \varepsilon) + \ln G_\sigma(i\omega_n)] \Big). \end{aligned} \tag{4.9}$$

From the DMFT equation, we can calculate the second term in Eq. (4.9). The unknown quantity is the impurity potential Ω_{imp}. In Subsection 2.2.3, we used Eq. (2.58) to calculate λ_0 by iterating the integral equations. We can prove that this λ_0 is exactly the impurity potential Ω_{imp}.

In Eq. (2.10), we have calculated the canonical partition function in the subspace $Q = 1$,

$$Z_C = \lim_{\lambda\to\infty} \left[e^{\beta\lambda}\langle Q\rangle_G(\lambda)\right] Z_{Q=0}, \tag{4.10}$$

where

$$\langle Q\rangle_G(\lambda) = \int d\omega \left[f(\omega)\mathcal{A}_f(\omega,\lambda) + b(\omega)\mathcal{A}_b(\omega,\lambda)\right]. \tag{4.11}$$

$f(\omega)$ and $b(\omega)$ are the Fermi and Bose functions, and $\mathcal{A}_{f,b}$ are grand-canonical auxiliary particle spectral functions. Here, the subscript b denotes both states $|\uparrow\downarrow\rangle$ and $|0\rangle$. From the definition $\Omega_{imp} = -\frac{1}{\beta}\ln(Z_C/Z_{Q=0})$, we can express the impurity contribution to the free energy as

$$e^{-\beta\Omega_{imp}} = \int d\omega\, e^{-\beta\omega}\left[A_f(\omega) + A_b(\omega)\right], \tag{4.12}$$

where $A_{f,b}$ are the projected spectral functions. The calculation of $\langle Q\rangle_G(\lambda)$ is nontrivial because the auxiliary particle spectral functions $A_{f,b}$ are divergent at the threshold frequency E_0 at $T = 0$, and the exact position of E_0 is unknown. To avoid this problem, we redefine the frequency again by setting $\omega \to \omega + \lambda_0$ and taking the limit $\lambda \to \infty$ after this replacement. λ_0 is determined by solving

$$\int d\omega\, e^{-\beta\omega}\left[A_f(\omega) + A_b(\omega)\right] = 1, \tag{4.13}$$

where $A_{f,b}(\omega) = \lim_{\lambda\to\infty} A_{f,b}(\omega + \lambda_0, \lambda)$ is the new auxiliary spectral function with the new reference energy. Comparing Eq. (4.13) with Eq. (4.12), it can be shown that $\lambda_0 = \Omega_{imp}$. Now, all parameters and variables in Eq. (4.9) are known and the average free energy $F \equiv \Omega/N$ can be calculated.

4.3. First-Order Phase Transition on a Bethe Lattice With Infinite Connectivity

Since DMFT is exact for an infinite dimensionality, we apply this method to a $d = \infty$ Bethe lattice, and calculate the phase diagram and the free energy.

In a Bethe lattice with connectivity z, every point has z nearest neighbors. Fig. 4.2 depicts a Bethe lattice with connectivity $z = 4$. There is no simple Fourier transform for this lattice. Therefore, we cannot calculate the DOS directly, but we can use the cavity method to formulate the lattice Green's function and calculate the DOS thereafter. For an infinite connectivity, we should use the renormalized hopping term $t = t_{ij}/\sqrt{z}$ to make the energy finite (see Section 3.1).

The local Green's function is formulated as

$$G = \frac{(z-2)\xi - z\sqrt{\xi^2 - 4(z-1)t^2/z}}{2(zt^2 - \xi^2)}, \tag{4.14}$$

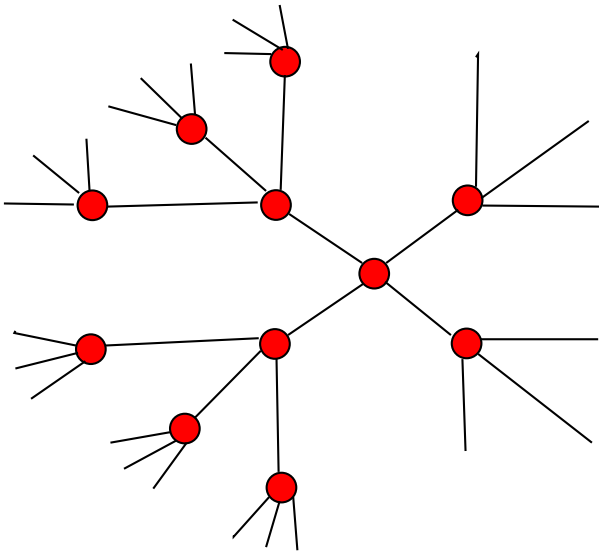

Figure 4.2.: Bethe lattice with connectivity $z = 4$.

where $\xi = i\omega + \mu$. The density of states $\rho(\varepsilon) = -\mathrm{Im}G(\varepsilon + i0)/\pi$ reads

$$\rho(\varepsilon) = \frac{\sqrt{\varepsilon^2 - 4(z-1)t^2/z}}{2\pi(t^2 - \varepsilon^2/z)}. \tag{4.15}$$

Taking the limit $z \to \infty$, the DOS of the Bethe lattice yields

$$\rho^{Bethe}(\varepsilon) = \frac{\sqrt{\varepsilon^2 - 4t^2}}{2\pi t^2}, \tag{4.16}$$

which is a semicircular-shaped band. Insert this non-interacting DOS into Eq. (3.40), we can calculate the Green's function at all interactions U and temperatures T, from which we can extract the DOS.

For any fixed temperature $0 < T < T_c$, we scan through U and find that as U increases, the DOS at the Fermi surface will slowly decrease. When $U > U_{c2}$, it will drop down abruptly and then keep decreasing, as is shown in Fig. 4.3. When U decreases from the insulating state, the system remains in the insulating state until U comes close to U_{c1}. Then it transits into a metallic state.

Looking at both Fig. 4.1 and Fig. 4.3, we can explain the M-I phase transition more clearly. Suppose we have an insulator and begin to decrease the interaction U. When $U > U_{c2}$, we have only one insulating solution, this is the case when $\alpha_3 > -8.0$ in $F(\eta) = 3\eta + \alpha_3\eta^2 + 6\eta^3$. When $U_{1st} < U < U_{c2}$, the metallic state begins to exist. Thermal excitations can excite some of the insulating states into the metastable metallic state. This is the case when $-8.4853 < \alpha_3 < -8.0$. In this region, it is still possible for us to get pure insulating states without metallic ones, if we can avoid transferring energy to the system. The same mechanism is used to over-cooled water. This is why we keep getting the insulating solution until $U = U_{c1}$ within the numerical treatment

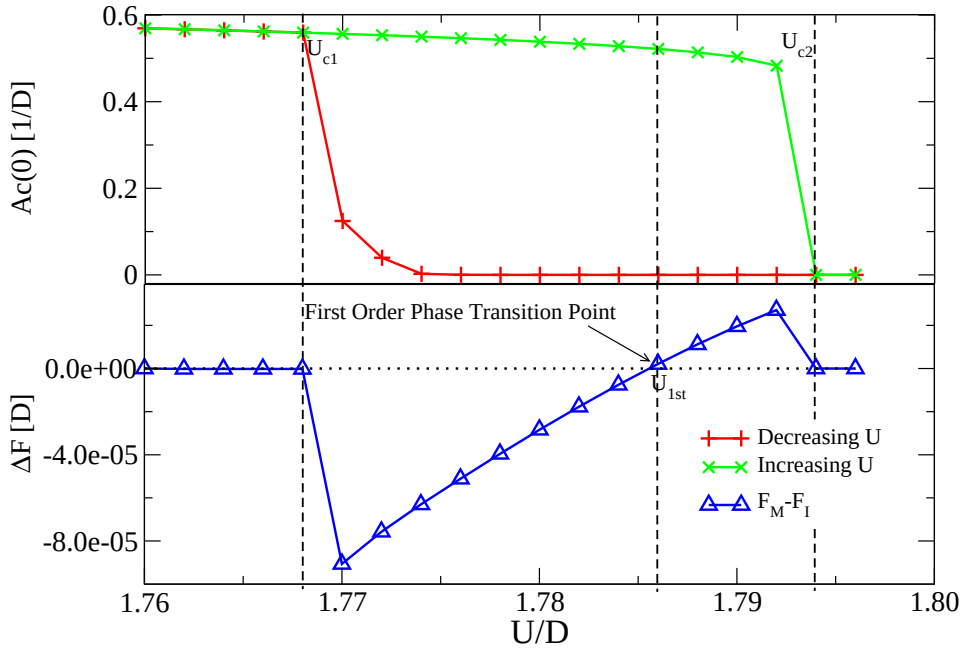

Figure 4.3.: $F_M - F_I$ in phase coexistence region. The red and green curve shows the density of states at Fermi surface changes at temperature $T/D = 0.005$, when interaction U increases (decreases). When $U_{c1} < U < U_{1st}$, the metallic state is a stable state and the insulating state is a metastable state. As U increases, the insulating state becomes stable and the metallic state is switched into the metastable state. When $U > U_{c2}$, the metallic state disappears and then the total system has only one state: insulating state.

of this system. When $U_{c1} < U < U_{1st}$, the insulating state is in the metastable state. Any thermal excitation can stop this insulator-metal phase transition suddenly. This corresponds to the case when $\alpha_3 < -8.4853$. When $U < U_{c1}$, the insulating state disappears and there is only one possible metallic state for the system.

After we carry out this calculation for all different temperatures, we can plot $F_M - F_I$ against U as shown in Fig. 4.4. From this figure, we read that at low temperatures, the free energy difference ranges from $-9 \times 10^{-5}D$ to $2 \times 10^{-5}D$, and at high temperatures, this range is much smaller, from $-2 \times 10^{-5}D$ to $1 \times 10^{-5}D$. As the free energy difference at high temperatures is much smaller than at low temperatures, this makes thermal excitations from low energy states to high energy states easier. At the same time, a high temperature can provide the needed energy much easier, this is also in favor of the thermal excitations. This property is very important and this explains why there is a higher possibility to obtain larger domains when we come close to the *first order phase transition line* (see chapter 5).

If we plot all U_{c1}, U_{c2} and U_{1st} points from Fig. 4.4 with U as the X-axis and T as the Y-axis, we can get the phase diagram of a paramagnetic metal-insulator phase transition (Fig. 4.5).

If we consider the DOS only, an exact insulator exists only at $T = 0$. There, the

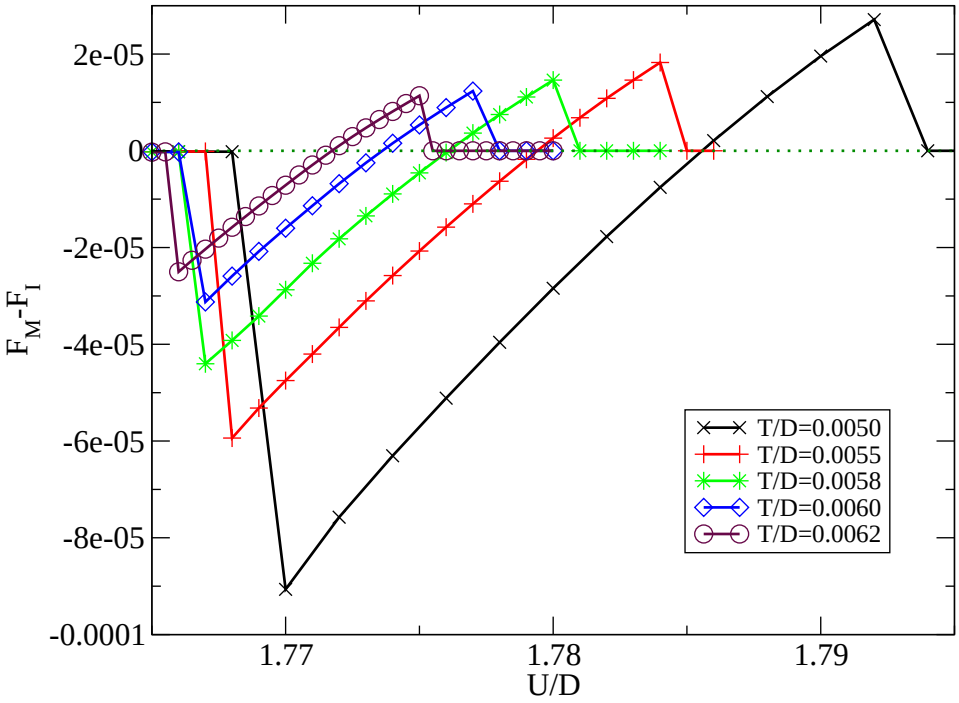

Figure 4.4.: $F_M - F_I$ at all temperatures.

density of states at the Fermi energy is exactly 0. At finite temperatures, the DOS at the Fermi energy is always non-zero because the thermal excitation can always excite the particles from the lower Hubbard band to the Fermi surface. Despite this, the distinction between a metal and an insulator is still possible because the DOS of the metal has a peak at the Fermi energy and the DOS of an insulator has a gap at the Fermi energy. The resulting free energy gives us another way to distinguish between a metal and an insulator. When $U_{c1} < U < U_{c2}$ and $T < T_c$, the red and blue lines in Fig. 4.5 draw a triangular region which is the phase coexistence region. In this region, the green line connects the second order phase transition point at both T_c and $T = 0$. When $T > T_{c,}$, a metallic phase can move continuously to an insulating phase. At $T = 0$ and $U = U_{c2}$, it is also a second order phase transition point, because at this point $d\Delta F/dU = 0$. The insulating state is only possible at $U > U_{c2}$ and the metallic state is possible at $U < U_{c2}$. This green line is the first order phase transition line, because it connects the points where $F_M = F_I$. On this line, the metallic state can transit into an insulating state without paying any energy. This phase transition happens without considering lattice deformation in the model. This kind of phase transition is reported to exist in the compound of $Y_{1-x}Ca_xTiO_3$ by Kato et al.; Nakao et al. (2007). They find that the M-I phase transition happens before the lattice structure changes.

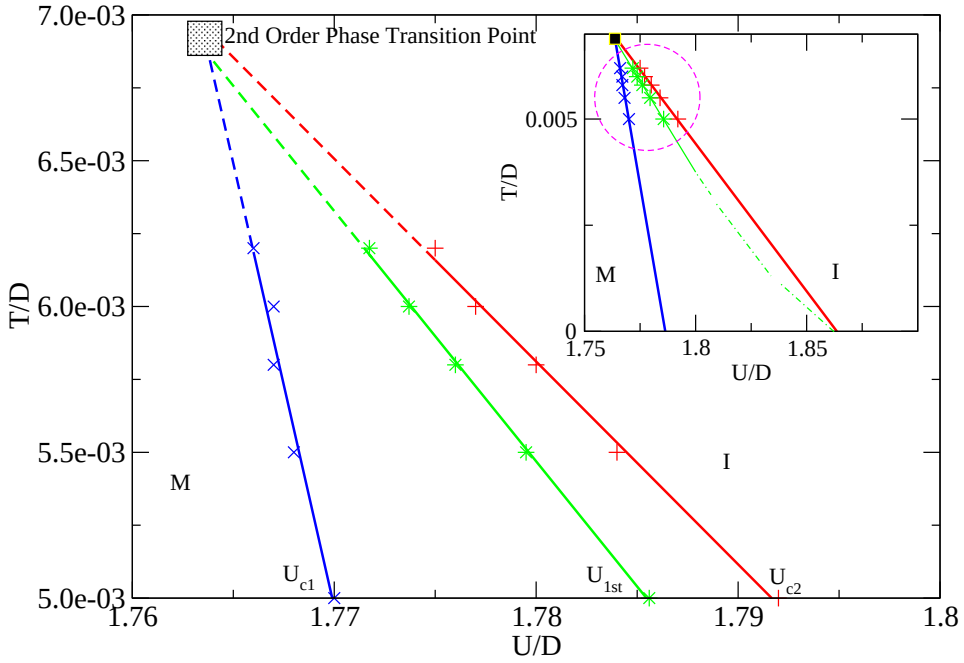

Figure 4.5.: Paramagnetic metal-insulator phase diagram. Since we concentrate on thermal excitations of the low energy states, we calculate only the high temperature part of the phase diagram. The inset shows the entire phase diagram, and the dashed circle shows the region which we are interested in. The green line is the first order phase transition line, on which we have $F_M = F_I$. Both ends of this green line are second order phase transition points. One of them is denoted by the black box. At this point, one phase can move continuously to another phase. The other one of the second order phase transition points is located at $T(U_{c2}) = 0$.

4.4. The First Order Phase Transition in the 3-d Hubbard Model

In Fig. 3.4 we have compared the DOS of the SC lattice model and the DOS of the layer structure with a flat 2-d band on each layer. Because of the divergence of 2-d DOS in the SC lattice model, we insert the DOS of Eq. (3.63) into Eq. (3.40) and calculate the Green's function of the 3-d Hubbard model and also the phase diagram.

As shown in Fig. 4.6, we find that the free energy difference $\Delta F(U,T) = F_M(U,T) - F_I(U,T)$ of the 3-d lattice lies in a smaller range than it does in the Bethe lattice with the same half-bandwidth D at the same temperature. This is because of the change of the lattice. Because when ΔF is smaller, it is more difficult to get the convergence of the layer DMFT. In the following chapter, we need to calculate the Green's function in high accuracy. This makes the convergence very slow. At the same time, the change of the lattice also changes the phase diagram.

The phase diagram Fig. 4.7 shows that we are very close to the second order phase transition point. This is indeed what we want, because we are interested in studying the thermal excitations of the micro domains. And these excitations take place with a

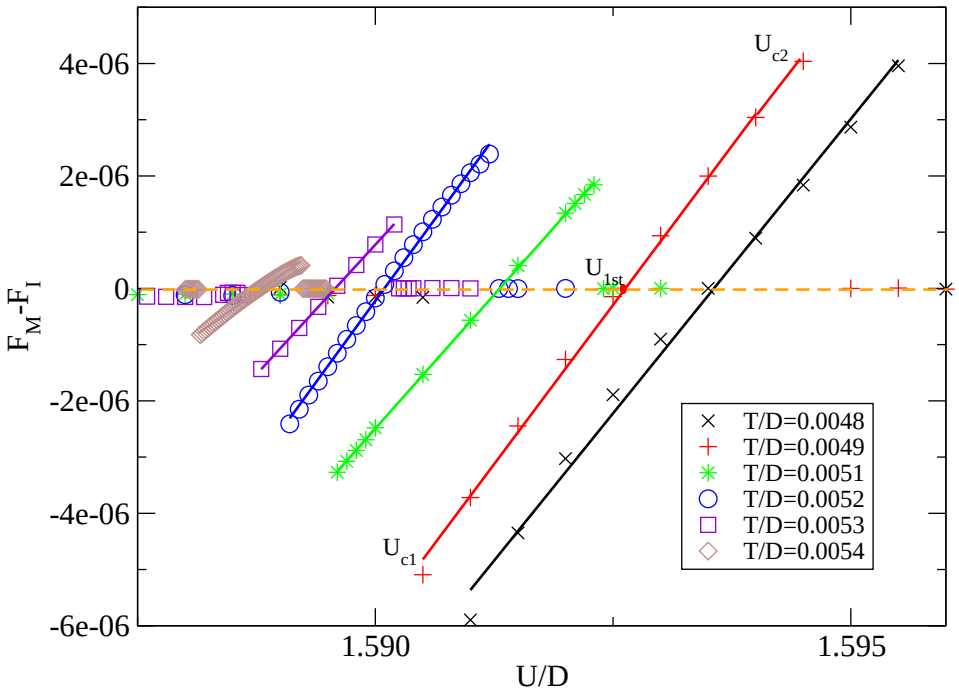

Figure 4.6.: $F_M - F_I$ .vs. U in 3-d lattice at different temperatures. Because the change of the non-interacting DOS, the ΔF range is smaller than the Bethe lattice case.

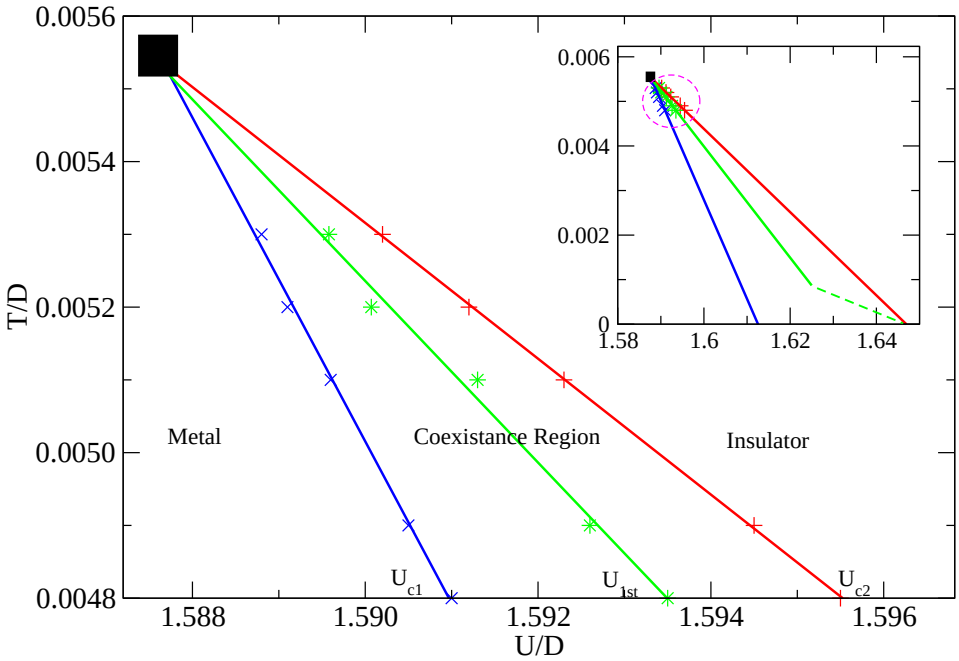

Figure 4.7.: Phase Diagram of a 3-d Lattice with the non-interacting DOS equal to ρ^{3D}.

higher possibility when the system comes to the high temperature coexistence region.

Since the M-I transition of the 3-d lattice Hubbard model is a first order phase transition, the phase coexistence region is depicted in Fig. 4.7 (the triangular region between the red and blue line). In this region, the metallic phase and the insulating phase coexist. A domain wall between the metallic and insulating phase should form. How to study the domain wall formation is the topic of the next chapter.

Chapter 5.

Micro Domain Formation

In Chap. 4 we showed that the Mott-Hubbard metal-insulator transition at finite temperature in a 3-d Hubbard model is a first order phase transition, and it has a phase coexistence region in the phase diagram (Fig. 4.7). In this phase coexistence region, domains can be thermally excited from the bulk material into a meta stable state, what hints the coexistence of insulating and metallic states. It is known that, the insulating state has a lower DOS on the Fermi energy $\rho_I(0)$ than the metallic state $\rho_M(0)$, i.e. $\rho_M(0) > \rho_I(0)$. Between $\rho_M(0)$ and $\rho_I(0)$, there is the domain wall, whose DOS ranges between ρ_M and ρ_I. What is the shape of the domain and how is the domain formed, these are still open questions. These questions can be answered by studying the DOS and the free energy on domain wall. The layer dependent DOS shows that the thickness of the domain wall increases as $|\Delta F|$ goes to 0. The free energy against order parameter plot agrees with the Ginzburg-Landau theory, which shows that the metallic and insulating states are located at the local minimum on this curve.

Making use of the studies of the free energy on the domain wall, we can calculate the domain size distribution function $P(R)$, which turns out to be dependent on the temperature and interaction strength. $P(R)$ function gives the probability to find a domain of radius R. And it also shows what is the most possible size of the domain at different T and U.

5.1. DOS on the Domain Wall

What's the "domain wall"? The domain wall is something which connects the domain (the meta-stable state) to the bulk (the stable state). In Fig. 5.1, the upper left schematic picture shows how the metallic domains are distributed inside a bulk material, and how the "wall" separates the domain from the bulk material. To explain the formation of domain wall, let's do a Gedankenexperiment. Suppose we have a bulk material in the metallic state and a bulk in the insulating state. The U and T of these two material are on the same point in the phase coexistence region of the phase diagram (see Fig. 4.5 and Fig. 4.7). What will it be if we connect this bulk metal and the bulk insulator together (It is somehow a hetero-junction in macro size, see upper right of Fig. 5.1)? Of course, we believe that nothing will happen deep inside the bulk material, but the DOS at the two sides of the contact must change somehow. This is the formation of domain wall (see Fig. 5.1, upper right corner). As the domain wall

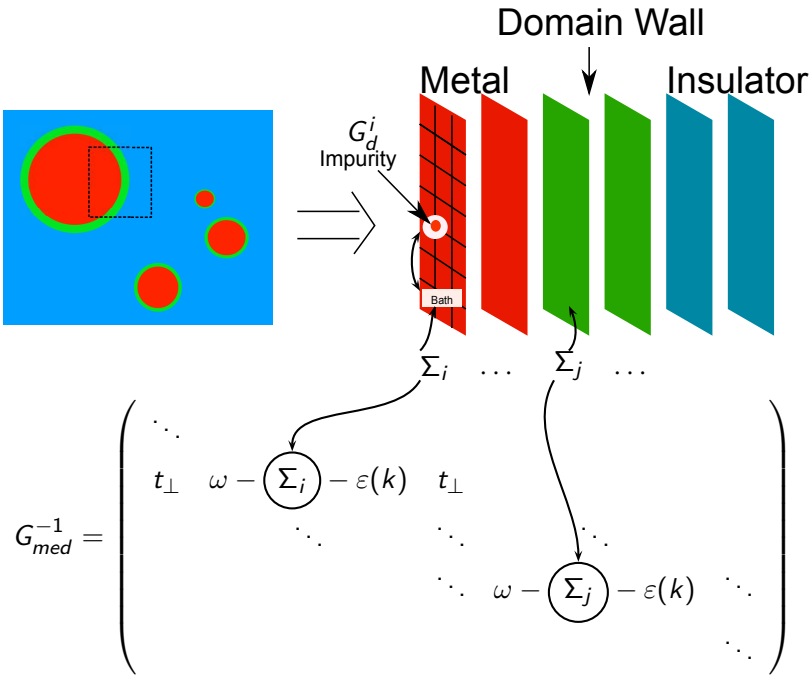

Figure 5.1.: Schematic domain structure. Let's begin with the assumption that all domains have a spherical shape. e.g. a metallic domain inside a bulk insulator. The metallic domain has a spherical shape, and there is a domain wall surrounding it, as shown in the upper left. We can expand the domain wall to layers of plains by letting the domain radius $R \to \infty$, as is shown in upper right corner. Then we have a pack of layers with each layer dominated by a self energy $\Sigma_i(\omega)$, where i is the index of the layer. The layer dependent self energy is used to calculate the medium Green's function $G_{med}(\omega)$, which is a $N \times N$ matrix, N is the total number of layers.

forms, the free energy on the domain wall changes. The free energy on each layer changes from the free energy of the metallic state to the free energy of the insulating state, which means the domain wall is actually somehow unstable. Because from Ginzburg-Landau theory, we know that the metallic and insulating state are the only two minima of $F(\eta)$ curve (see Fig. 4.1), all other F values are unstable solutions. In other words, we can have a domain wall in macro size only if we can have a bulk metal and a bulk insulator in macro size in the phase coexistence region at the same time. But this is not possible (The possibility is too small to let this happen, because of the thermal excitations.) in macroscopic world at all. According to the Landau theory of phase transition, we know that in the coexistence region, the system has two local minima of the free energy as a function of the order parameter (as shown in Fig. 4.1). This phase transition scheme tells us that in the phase coexistence region, any bulk material, either metal or insulator, has a certain possibility to contain another phase inside this bulk material. It is the same as the ice water phase coexistence. However, we can calculate the domain distribution function by considering

the free energy on the domain wall to obey a Boltzmann distribution function.

To calculate the domain distribution function, we should calculate the free energy of the domain first. The flow diagram of this calculation is shown in the lower panel of Fig. 5.1. Suppose we have a N-layer system, we assume the layers with index $i = 1, \ldots, N/2$ in the metallic state and the layers $i = N/2 + 1, \ldots, N$ in the insulating state. That is to say, we set an initial DOS on each layer, which also means that we know $G_{c,i}(\omega)$ (Eq. (3.38)) at the beginning. On each layer, we solve an impurity problem with NCA, by which we obtain $G_{d,i}$ and $\Sigma_i(\omega)$ from $G_{c,i}(\omega)$. With this Σ_i, we can write out the medium Green's function (Eq. (3.48)). Integrating out this G_{med}, we can calculate the new impurity Green's function $G_{d,i}^{(n+1)}$ (Eq. (3.51)). All Green's functions are denoted by a superscript $^{(n)}$, when it is the Green's function from the n-th iteration. We can get the new bath Green's function $G_c^{(n+1)}$ by solving equation $V^2 G_c^{(n+1)} + (G_d^{(n+1)})^{-1} = V^2 G_c^{(n)} + (G_d^{(n)})^{-1}$. The steps to calculate the layer dependent Green's functions are summarized as below:

1. We start from a Green's function $G_{c,i}$. The $G_{c,i}$ are the solution of the bulk system under the same parameter U and T. In the phase coexistence region, $G_{c,i}$ can have two possible solutions: the insulating solution and the metallic solution.

2. On each layer i, we apply the NCA algorithm to solve the impurity problem. By this, we obtain the corresponding $G_{d,i}$ and therefore Σ_i.

3. Using Eq. (3.48) to determine G_{med}^{-1}, we obtain the medium Green's function.

4. By integrating $\int d\varepsilon \rho^{2D}(\varepsilon)(G_{med}^{(n)})^{-1}$, we obtain $G_{d,i}^{(n+1)}$.

5. Solving $V^2 G_c^{(n+1)} + (G_d^{(n+1)})^{-1} = V^2 G_c^{(n)} + (G_d^{(n)})^{-1}$ to get $G_c^{(n+1)}$.

6. Comparing $G_{c,i}^{(n)}$and $G_{c,i}^{(n+1)}$, if the difference reaches the required accuracy, stop and output the results, otherwise, go to step 2.

Here, we should point out that all the Green's functions and free energies in this calculation are matrices. Therefore, it usually takes a very long time to obtain a converged result. In our case, it takes about 20 days for a 120-layer system to converge to $err < 5.0\mathrm{E} - 4$ on a cluster of 20 nodes. If we use a much smaller convergence criterion, it takes much more time of course. As this is a demanding calculation, we can not expect that the layer dependent free energy has the same accuracy as the layer independent one. In spite of this very demanding calculation, we can still get enough information, especially on the physical background, from analyzing the results.

The first important result is about the layer dependent DOS. Since the idea of calculating the domain wall is to bring an insulator and a metal into contact, we need at first the bulk solutions at the same temperature and pressure. These can be obtained by using NCA+DMFT (subsection 3.2.3). With the metallic and insulating solutions for the same parameters, we set the first 30 layers as insulators, and the last 30 layers

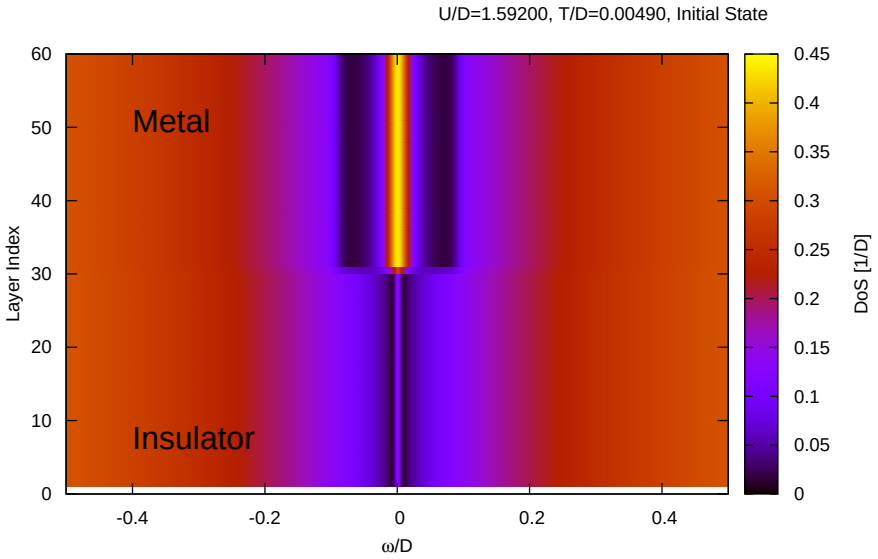

Figure 5.2.: As a comparison, we show here the initial DOS on each layer when $U/D = 1.59200$ and $T/D = 0.00490$.

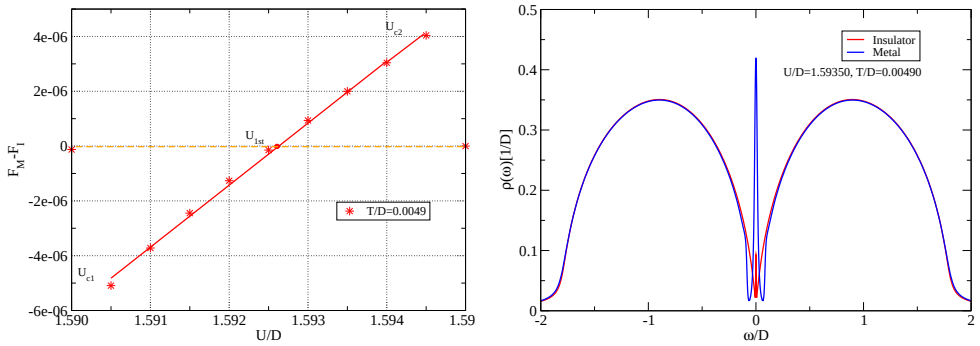

(a) (b)

Figure 5.3.: (a) $F_M - F_I$ vs. U at $T/D = 0.00490$. At this temperature, the first order phase transition interaction reads $U_{1st} \simeq 1.5926$. (b) Initial DOS for layer dependent calculation. Usually, we set the first 30 layers as an insulator, and the last 30 layers as metal in a 60-layer system. As we have discussed in Chapter 4, in the phase coexistence region, as shown in Fig. 4.7, we can always find two solutions for the Hubbard model using DMFT and NCA, which is introduced in Subsection 3.2.3.

as metals, that is to say, let $G_{c,i} = G_{c,insulator}$ for $i = 1, \ldots, 30$, and $G_{c,i} = G_{c,metal}$ for $i = 31, \ldots, 60$. (see Fig. 5.2)

To study the domain wall formation during the M-I phase transition, we keep the temperature fixed and increase the interaction U. As shown in Fig. 5.3, when $1.5905 < U/D < 1.5926$, the metallic state is the stable one, and as U increases, the free energy difference $|\Delta F| \equiv |F_M - F_I|$ also becomes smaller. This change has a fundamental effect, that is the low energy state is easier to be excited to the high energy metastable state. Because the energy gap between these two states becomes smaller. Usually, only the layers which are located very close to the metal-insulator interface can be excited, but when $|\Delta F|$ is small, this kind of thermal excitation can extend into the bulk material. This is reflected by showing that the domain wall thickness increases as $|\Delta F \to 0|$.

The results are shown in Fig. 5.4, Fig. 5.5 and Fig. 5.6. Fig. 5.4 shows the $\rho_i(\omega) = \mathrm{Im}G_c(\omega - I0^+)/\pi$, where i is the index of layer. As ρ_i is the density of states of the conduction band, it should contain the lower and upper Hubbard band as shown in Fig. 5.3(b). Since we are interested in the transport property only, which is dominated mostly by the DOS on the Fermi surface, we show here DOS near the Fermi energy (Fig. 5.2).

5.1.1. Layer Dependent DOS for $\Delta F < 0$

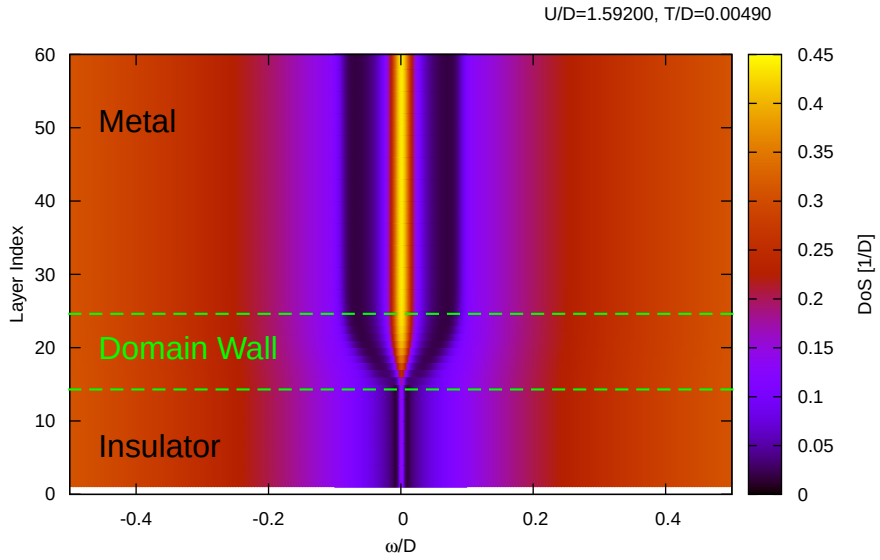

Figure 5.4.: Layer dependent DOS $\rho_i(\omega)$ for $U/D = 1.59200$ and $T/D = 0.00490$. In Fig. 5.3, we know that the corresponding $\Delta F = F_M - F_I \simeq -1.7 \times 10^{-6} D$. Here $F_M < F_I$, if we connect the metal to the insulator, the total system will tend to transit into the *metallic state*, which has lower energy. Thus, the insulator becomes *smaller* and the metal becomes *bigger*. In this figure, the domain wall has a thickness of about $10a$, where a is the lattice constant.

For $\Delta F < 0$, the metallic state is stable, and the insulating state is meta stable. If we push such two material in different states together, part of the insulator will transit

into the metal, in order to keep the total energy low. Therefore, comparing to the initial state in Fig. 5.2, we should find that the volume of insulator will shrink and the volume of metal will increase. Fig. 5.4 shows this behavior clearly. It seems like that the domain wall drift to the insulator side.

To make the calculation running properly, we should set the boundary condition for the system, otherwise, after several iterations, the whole system will find the final solution at in the stable state. We set the boundary condition like this: keeping $G_i = G_{c,insulator}$ for $i = 1, \ldots, 15$ and $G_i = G_{c,metal}$ for $i = 46, \ldots, 60$ constant. In Fig. 5.3 (b), one can observe that there is a very high resonance peak at the Fermi energy in the metallic state. In the insulating state, there is a gap at the Fermi energy instead. In Fig. 5.4, we find that from $i = 15$ to $i = 25$, the DOS at the Fermi energy $\rho_i(\omega = 0)$ increases, this indicates the range of the domain wall.

5.1.2. Layer Dependent DOS for $\Delta F > 0$

The position of the domain wall drifts when ΔF varies. When ΔF increases and changes to positive, the domain wall will drift into the metallic side. This is because that the metallic state is the metastable state when $\Delta F > 0$. If the initial state of a system is the metallic state, it will transit into the insulating state to keep the total energy lower. This effect results in the domain wall drifting away from the insulator side, as shown in Fig. 5.5. The thickness of the domain wall measures about $12a$.

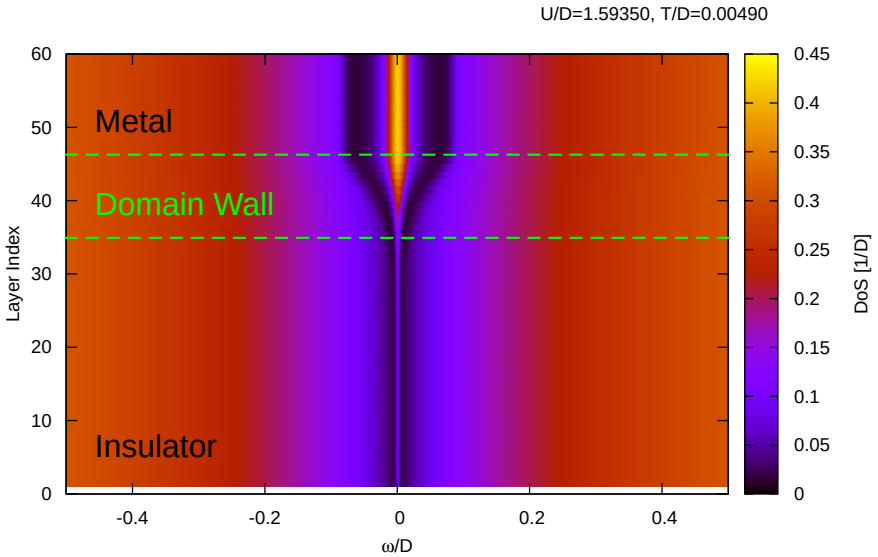

Figure 5.5.: Layer dependent DOS $\rho_i(\omega)$ at $U/D = 1.59350$ and $T/D = 0.00490$. In Fig. 5.3, we know that at the same parameters the corresponding ΔF reads $\Delta F = F_M - F_I \simeq 2.0 \times 10^{-6} D$. Since here $F_M > F_I$, if we connect the metal with the insulator, the total system will tend to change into the *insulating state*, which has lower energy. Thus, the volume of the insulator becomes *bigger* and the volume of the metal becomes *smaller*. The domain wall has a thickness of about $12a$.

5.1.3. Layer Dependent DOS for $\Delta F \to 0$

We have discussed the domain wall formation in the case of $\Delta F > 0$ and $\Delta F < 0$ so far. Now we can move a step further, let us see what will happen for ΔF close to 0. First, let us see numerical results of the layer dependent DOS in Fig. 5.6.

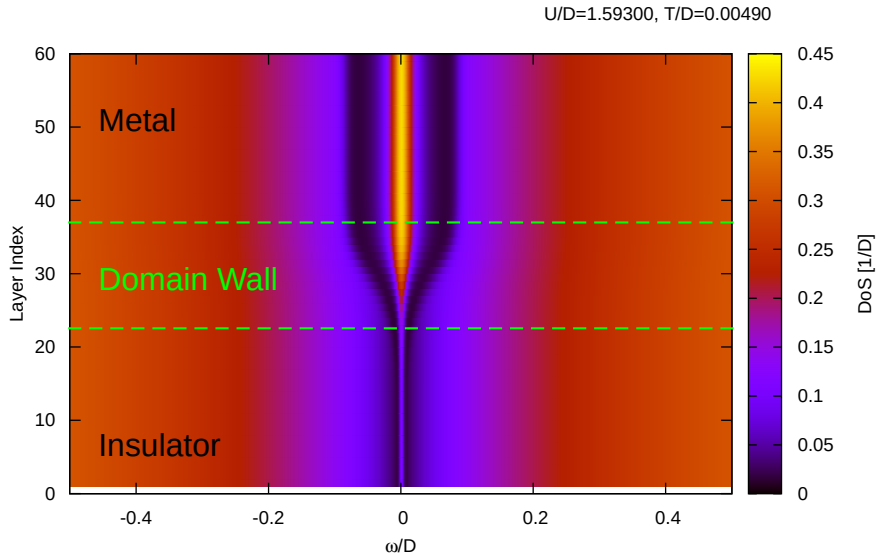

Figure 5.6.: Layer dependent DOS $\rho_i(\omega)$ when $U/D = 1.59300$ and $T/D = 0.00490$. In Fig. 5.3, we know that the corresponding $\Delta F = F_M - F_I \simeq 1.0 \times 10^{-6} D$. Since here $F_M > F_I$, if we connect the metal with the insulator, the total system will tend to change into the metallic state, which has lower energy. On the other hand, the value ΔF under this U parameter is smaller comparing to the ΔF when $U/D = 1.59350$, the final insulator volume should be bigger than the metal volume, but smaller than the insulator volume at $U/D = 1.59350$. The domain wall has a thickness of about $18a$, which is much thicker than Fig. 5.4 and Fig. 5.5.

Because we are doing a numerical calculation, and the needed CPU time diverges as ΔF comes closer to 0, we can not provide the numerical results for the case ΔF is exactly 0. We choose here a point ($U/D = 1.5930$ and $T/D = 0.00490$) in the free energy diagram (Fig. 5.3), which is closer to 0 than other points that we have calculated. For this parameter, $\Delta F = 1 \times 10^{-6} D$, which is almost half of the ΔF for $U/D = 1.5920$ and $U/D = 1.5935$, ΔF is still greater than 0, which means that in Fig. 5.6, the metallic state has higher energy, but the absolute value of this energy difference is smaller comparing to the case in Fig. 5.4 and Fig. 5.5. For this reason, the domain wall extends deep into the bulk material comparing to the case when U/D is close to the boundary of the phase diagram at the same temperatures. This is easy to understand. When $|\Delta F|$ is small, at the same temperatures, the low energy states has greater possibility to be excited to the high energy state, because the energy barrier is lower comparing to the thermal excitation. Therefore, more low energy layers can be excited to the high energy states. At the same time, more layers in the high energy state also hop to the low energy states. The total effect of this thermal excitation and hopping results that the thickness of the domain wall increases as $|\Delta F| \to 0$. From Fig. 5.6, we read

that the domain wall extends to about 18 layers. As is known, a lot physical parameters diverge at the phase transition point, e.g. the correlation length ζ and the heat capacity C. It is the same for the size of the domain wall, as shown in Fig. 5.7.

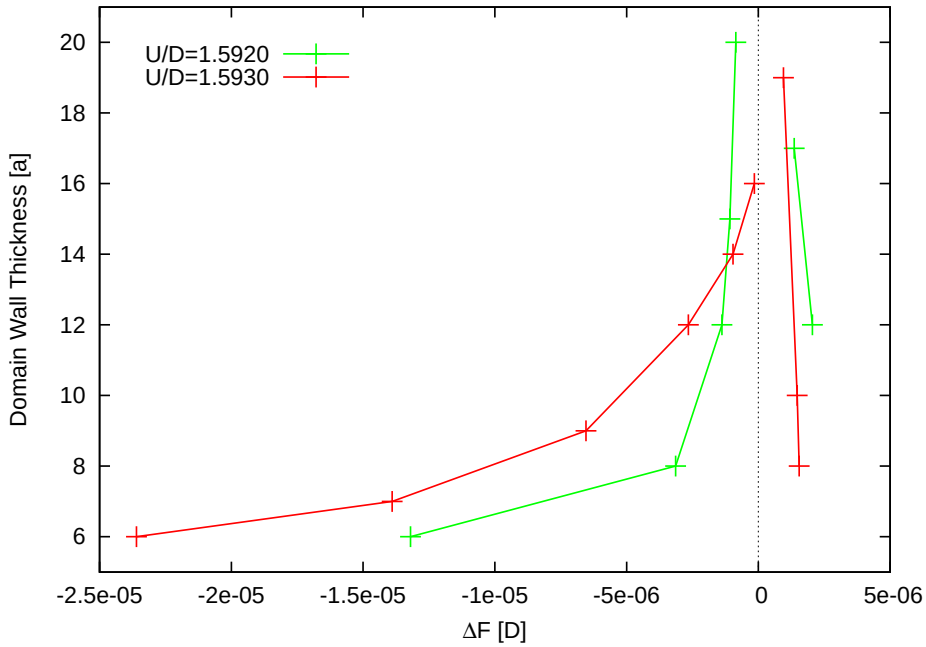

Figure 5.7.: The thickness of the domain wall diverges as $|\Delta F| \to 0$, where $\Delta F \equiv F_M - F_I$.

5.2. Free Energy on Domain Wall

In Section 5.1, we showed that if we connect an insulator and a metal together when they are in the phase coexistence region, a domain wall will be created and its position shifts according to the free energy difference $\Delta F \equiv F_M - F_I$, where $F_{M,I}$ is the site free energy of the metallic/insulating state. With the help of layer dependent DMFT, we can also calculate the Green's function on the domain wall, and we showed the domain wall by plotting the DOS on each layer in Fig. 5.4, Fig. 5.5, and Fig. 5.6. With the layer dependent Green's function, We can also calculate the free energy on the domain wall from Eq. (4.9).

Fig. 5.8 shows the layer dependent free energy on each layer. The left hand side is the insulator and the right hand side is the metal. $F(i)$ is the free energy on the layer i, where i is an index ranging from 1 to 60 as shown in Fig. 5.8. F_M is the metallic state free energy. We use $F(i) - F_M$ instead of $F(i)$ as the y value, because it is more suitable for our further analysis. First, we know from Fig. 5.8 that ΔF in this figure equals to the corresponding $F_M - F_I$ in Fig. 5.3. This shows the validity of our LDMFT method in domain wall calculations, because we can reproduce the normal DMFT results with LDMFT. In Fig. 5.3, we obtain the free energy using the normal DMFT on a simplified

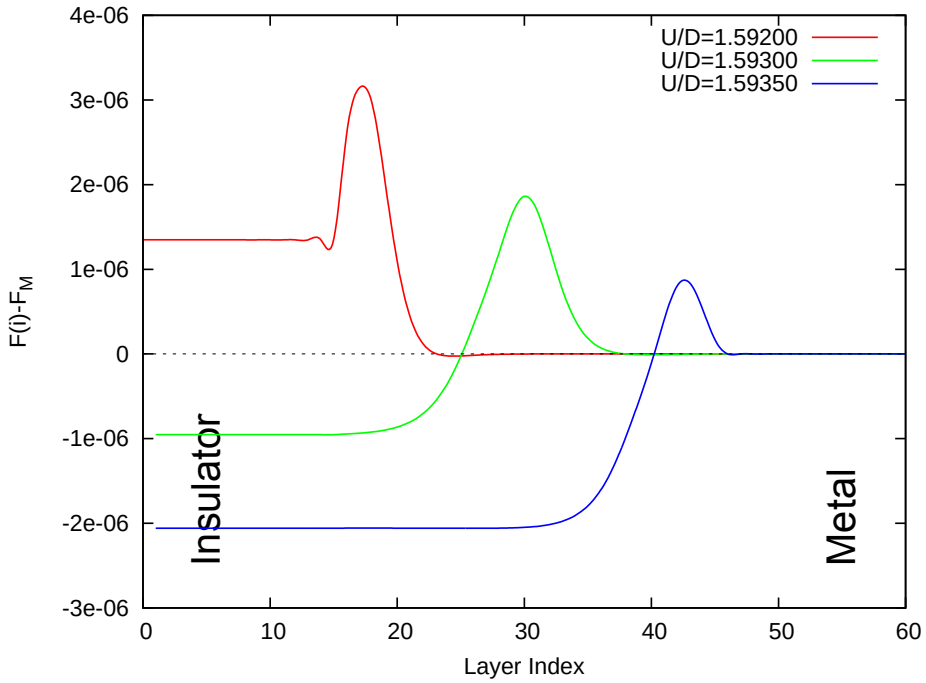

Figure 5.8.: Layer dependent free energy shows the position and thickness of a domain wall (at $T/D = 0.0049$).

3-d simple cubic lattice, whose DOS is obtained by Eq. (3.55). Here, we obtained the layer dependent free energy $F(i) - F_M$ using the spatially resolved DMFT (Eq. (3.51)). On each layer, the momentum integration is carried out over a flat band (Eq. (3.52)). Therefore, at the same parameters U and T, ΔF in Fig. 5.3 and Fig. 5.8 should be equal. Second, we should notice that on the high energy side of the domain wall, the free energy is higher than the free energy in metastable state, and there exists a energy barrier between the metastable state and the stable state. This barrier has a fundamental impact in domain formation, because the system should pay some extra energy to overcome this energy barrier. If we choose the DOS at Fermi energy $\rho_i(\omega = 0)$ as the order parameter η, we have Fig. 5.9.

The lines in Fig. 5.9 have the same shape as those in Fig. 4.1, the difference is that here we replaced $F(\eta)$ with numerical results calculated by LDMFT instead of that conceptional equation. As we have discussed in Chapter 4, the on-site interaction induced metal-insulator phase transition is a first-order phase transition. Here, our numerical calculation shows the $F(\eta)$ function for different interaction parameters U. This $F(\eta)$ functions shows a first order phase transition according to the previous discussion of Ginzburg-Landau theory. In Fig. 5.9, η_I and η_M are the order parameters which makes the first order derivative of $F(\eta)$ to η equal to 0. From this plot, we can conclude that for decreasing U, the free energy difference ΔF decreases, until the local minimum at η_I disappears. And for increasing U ΔF increases, until U steps out of the phase coexistence region and there the minimum at η_M disappears. In a value between $U/D = 1.59200$ and $U/D = 1.59300$, there should exist a value U_{1st}, at

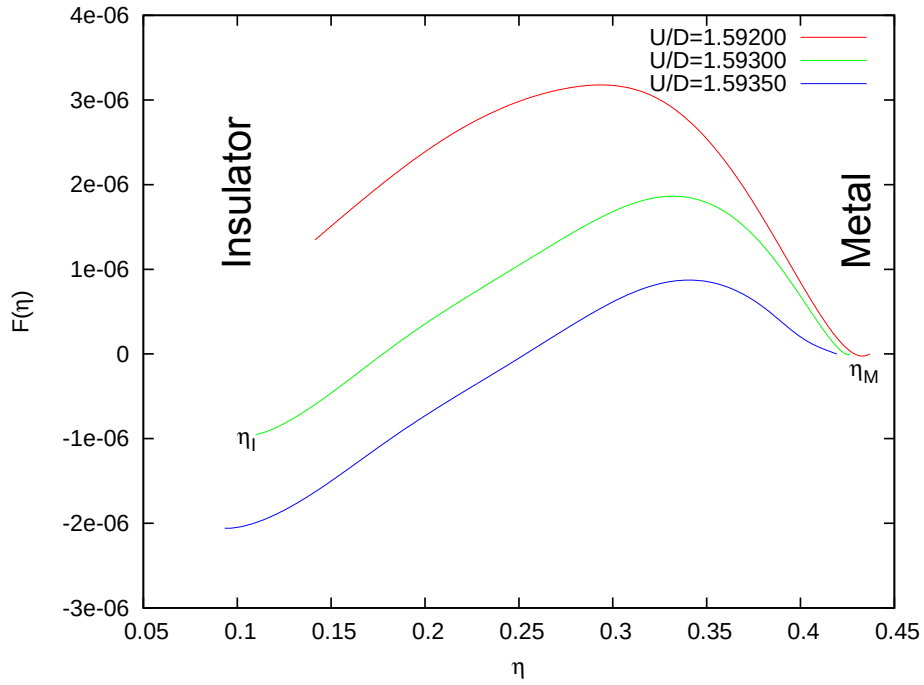

Figure 5.9.: free energy vs. order parameter η at $T/D = 0.00490$. The DOS on Fermi surface $\rho_i(0)$ is chosen as the order parameter η. The point η_I and η_M indicates position of the minima in function $F(\eta)$ in Eq. (4.1).

which $F(\eta_M) = F(\eta_I)$. Although we have not calculated directly, we conclude that this U_{1st} value should be around 1.5926, according to Fig. 5.3.

If we keep the interaction U fixed, and increase/decrease the temperature T in phase diagram Fig. 4.7, the system can also transit from metallic state to the insulating state, and vice versa. This is a so called temperature induced phase transition. In the experiments of Wu et al. (2006) and Berger et al. (1998), they showed such kind of phase transition. We can also show that the temperature induced phase transition is also a first-order phase transition by the $F(\eta)$ curve at different temperatures (Fig. 5.10).

It's easy to see that there are two local minima in Fig. 5.10, and the curve of $T/D = 0.00485$ shows $F(\eta_I)$ is almost equal to $F(\eta_M)$, because the point $T/D = 0.00485$ and $U/D = 1.59300$ is very close to the first order phase transition line.

5.3. Domain Distribution Function

In Section 5.2 we have calculated the free energy on the domain wall, and we find that the free energy on part of the domain wall can be greater than $\max(F_M, F_I)$. This means that, if we want to calculate the total free energy of a domain bubble with radius R, we must also consider the free energy on the domain wall. The sketch Fig. 5.11 explains how we define the domain radius R. The red color indicates the

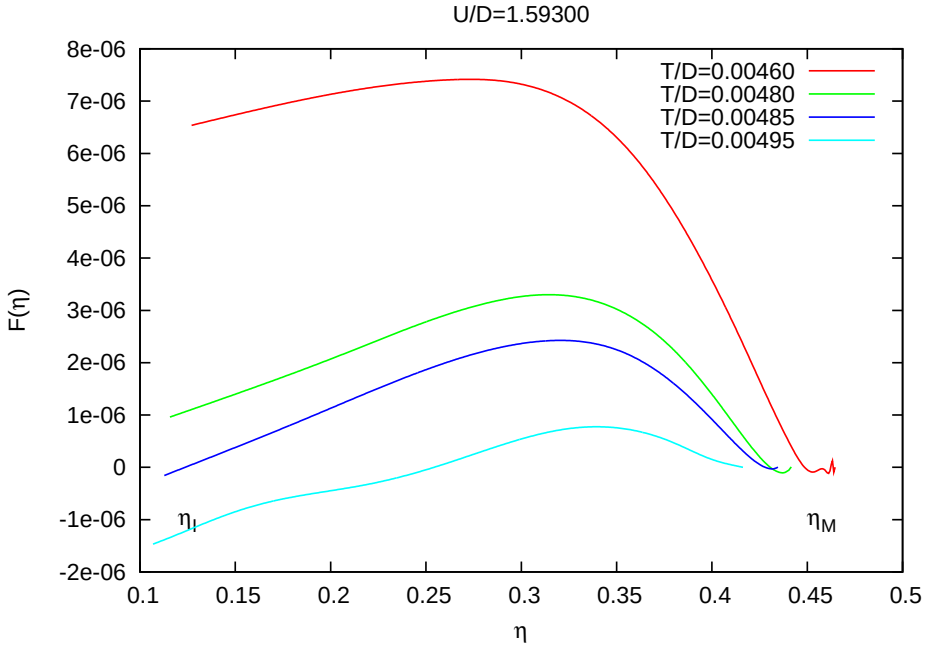

Figure 5.10.: $F(\eta)$ at different T, $U/D = 1.59300$.

insulator region and the blue stands for the metal region. The green color stands for the domain wall with the thickness of d. The domain bubble radius R equals to the insulator radius r plus the domain wall thickness d.

From Fig. 5.11, we see that in order to calculate the free energy of the bubble, we must calculate the free energy of the insulator region ($\mathcal{F}(r)$, red part) and also the free energy on the domain wall ($\mathcal{F}(d)$, green part). As only the free energy difference is relevant, we could always shift the energy level to choose the low energy state as the ground energy level. For example, when we discuss the insulator domain bubble inside a metal bulk, we could set $F_M = 0$ and replace F_I by $F_I - F_M$. Keeping in mind that F_I is average free energy of one site and the free energy of the insulator bubble reads

$$\mathcal{F}(r) = \frac{4\pi}{3}(\frac{r}{a})^3 F_I, \tag{5.1}$$

where a is the lattice constant. To calculate $\mathcal{F}(d)$, we divide the domain wall into shells, and on every shell, the site free energy F_i can be obtained from analysing Fig. 5.8. As we have set the free energy to let $F_M = 0$, we have

$$\mathcal{F}(d) = \sum_{i=1}^{d/a} 4\pi(r/a + i)^2 F(i + i_0), \tag{5.2}$$

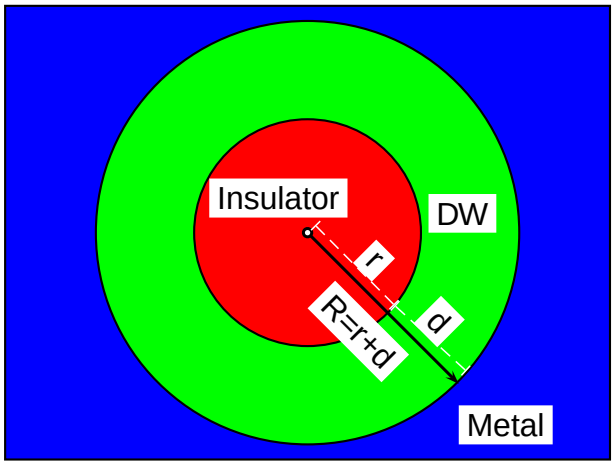

Figure 5.11.: Sketch of a domain bubble.

where d is the width of the domain wall, and i_0 indicates the starting position of the domain wall in Fig. 5.8. The total free energy of the domain bubble then reads

$$\mathcal{F}(R) = \mathcal{F}(r) + \mathcal{F}(d). \tag{5.3}$$

Analogously, $\mathcal{F}(r)$ for a metallic bubble can be obtained by setting $F_I = 0$ and replacing F_M by $F_M - F_I$.

According to the Boltzmann distribution function, the possibility to find a domain bubble of radius R inside a bulk material is

$$P(R) = C \exp(-\frac{\mathcal{F}(R)}{k_B T}), \tag{5.4}$$

where k_B is the Boltzmann constant, T is the temperature, and the coefficient C is determined through normalization condition

$$\int P(R) dR = 1. \tag{5.5}$$

Since the function $\mathcal{F}(R)$ depends on both U and T in a complex way, we can only study this $P(R)$ function numerically.

5.3.1. Results of $P(R)$

The distribution function $P(R)$ shows the possibility to find a domain of radius R. Fig. 5.12 shows $P(R)$ for $U/D = 1.59200$ and temperatures which assures $\Delta F < 0$. When $\Delta F < 0$, the metallic state is the stable state. The insulating micro domains are excited inside this bulk metal. As T increases, ΔF goes close to 0, we find that the most probable value of the distribution function also increases with T. It is because

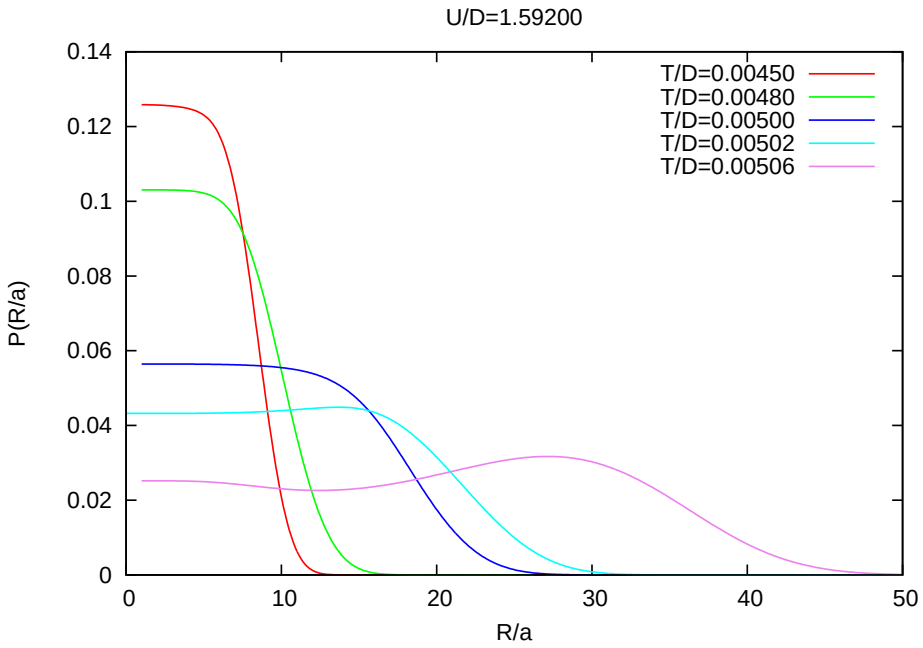

Figure 5.12.: Distribution function at $U/D = 1.59200$, $T/D \leq 0.00506$. In this region, $\Delta F < 0$, insulating domains is excited inside a metal bulk.

when the free energy difference ΔF is smaller, the free energy of the total domain bubble $\mathcal{F}(R)$ is also smaller and therefore $P(R)$ is greater. $\mathcal{F}(R)$ depends on $F(i) - F_M$ (Fig. 5.13) and the domain radius R. When the temperature is very low, e.g. at $T/D = 0.0045$, the system is very close to the phase boundary of the metallic state side. At this point, the free energy of the insulating state is much greater than the metallic state. And for lower temperatures, it is difficult to excite the insulating domain inside a metal bulk material. We find that $P(R)$ under this parameter peaks at $R/a = 5$. As T increases, $F(i)$ decreases, it becomes easier to excite an insulating domain inside a metal bulk. We find that $P(R)$ extends to 50 when $T/D = 0.00506$. This tells us that the average domain size increases as T increases before T reaches to $0.00506D$

The evolution of $P(R)$ changes when $\Delta F > 0$ (Fig. 5.14). When $T/D > 0.00508$, from $P(R)$ we read that the average domain size decreases with increasing T. This can be explained for $\Delta F > 0$ ($\Delta F \equiv F_M - F_I$, Fig. 5.15), the absolute value of ΔF increases as T increases. This makes the excitation of a metallic domain inside an insulator bulk more difficult at higher temperature. Correspondingly, we find that the peak of $P(R)$ moves towards 0 with an increasing T.

5.3.2. The Algorithm about creating randomly distributed domains

From Fig. 5.12 and Fig. 5.14, we know that what is happening in a metal-insulator phase transition . We take the temperature induced M-I transition at $U/D = 1.59200$

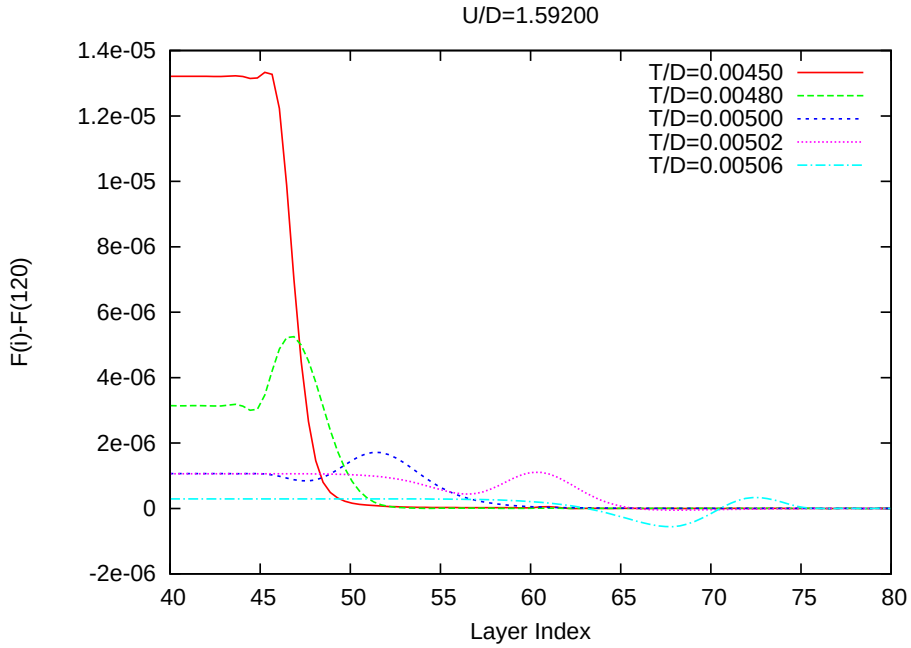

Figure 5.13.: Free energy on domain wall, $U/D = 1.59200$. $Layer\,Index < 40$ indicates the insulating state, and $Layer\,Index > 80$ indicates the metallic state.

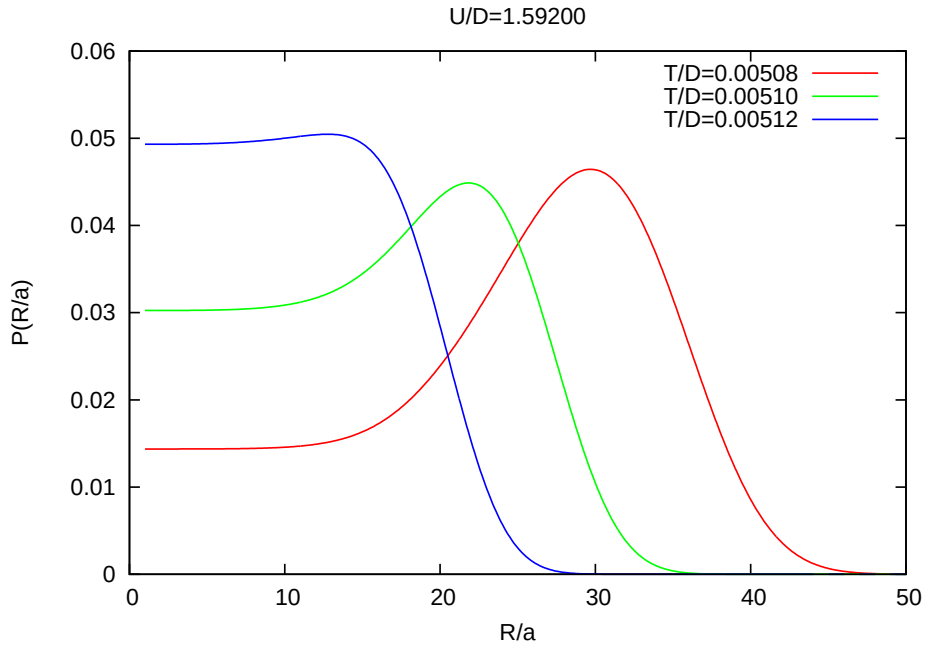

Figure 5.14.: Distribution function at $U/D = 1.59200$, $T/D > 0.00508$. This region indicates where $\Delta F > 0$ and therefore metallic domains are excited inside an insulator bulk.

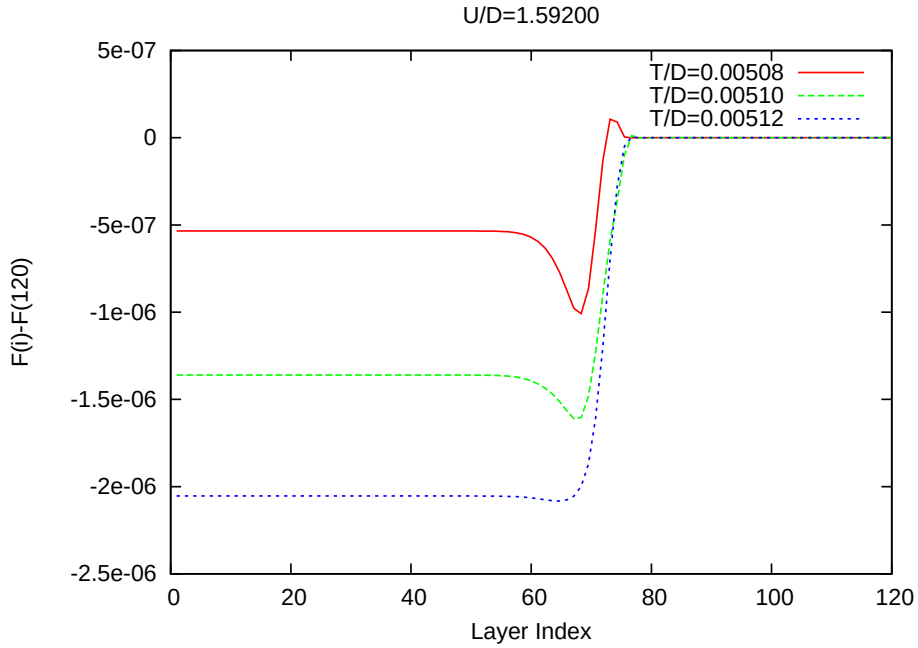

Figure 5.15.: Free energy on domain wall, $U/D = 1.59200$. $Layer\ Index < 40$ indicates the insulating state, and $Layer\ Index > 80$ indicates the metallic state.

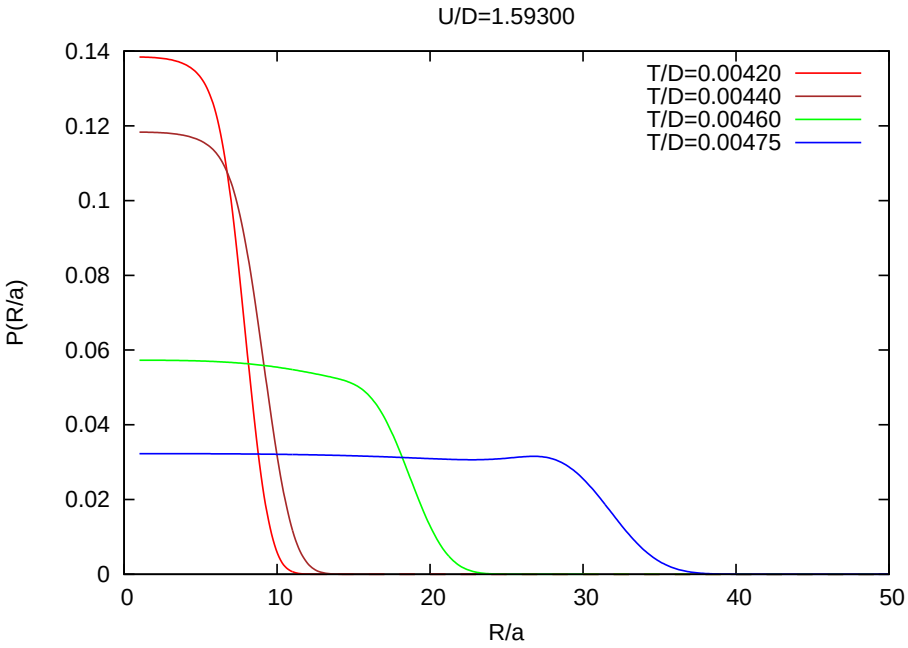

Figure 5.16.: Distribution Function at $U/D = 1.59300$, $T/D < 0.00485$. Insulator domains are excited inside metal bulk.

as an example. At low temperatures in the phase coexistence region, e.g. $T/D = 0.00450$, the maximum value of $P(R)$ locates around 5. This indicates that most of the domains has a size of $R/a \simeq 5$. To determine the number of domains, we still need the energy distribution on the bulk material and the domains. For example, suppose we have a cubic bulk with the size of $N \times N \times N$, and suppose we have m domains inside this bulk. m domain holds $m \times \int dR 4\pi R^3 P(R)/3$ lattice sites, we name it N_{domain} and we call the other sites in the system N_{bulk}. The system has $N_{Tot} \equiv N^3$ sites. We have

$$N_{domain} + N_{bulk} = N_{Tot}. \tag{5.6}$$

According to the Boltzmann distribution, we know that

$$\frac{N_{domain}}{N_{bulk}} = \exp\left[-\frac{F_{domain} - F_{bulk}}{k_B T}\right], \tag{5.7}$$

and we define $\kappa \equiv N_{domain}/N_{bulk}$. Because F_{domain} and F_{bulk} are already known, the value of m can be calculated by solving Eq. (5.6) and Eq. (5.7).

With the knowledge of N_{domian}, we use the following algorithms to create the random domains:

1. Create a random coordinate (x, y, z), where $0 \leq x,\ y,\ z \leq N$. This coordinate is the center of one domain bubble.

2. Create another random number pair (r, p), r is the radius and p is the probability to create a domain bubble. If $p \leq P(r)$, this number pair is accepted, otherwise, we create another pair of (r, p). Here, the function $P(r)$ is the domain distribution function which was defined in Eq. (5.4). This step assures that the randomly generated domains obey the domain distribution function $P(R)$ in statistics.

3. For one pair of (x, y, z) and r, we draw a bubble inside the $N \times N \times N$ cubic lattice. With this algorithm, we can create lots of domain bubbles. We calculate the number of lattice sites which are included inside all of these bubbles, and call this number N_{SD}. If $N_{SD} < N_{domain}$, go to step 1 and create one more pair of (x, y, z) and r, until we get $N_{SD} \geq N_{domain}$. Therefore, in this algorithm, the new generated domian can overlap with the old domains.

With the knowledge of the number of domains inside the bulk material, we can calculate how many domains of a specified radius R are created inside a bulk material. Fig. 5.17 shows what is happening when there is a temperature induced M-I transition. Out of the phase coexistence region, e.g. at $U/D = 1.5920$ and $T/D < 0.0045$, only metallic state exists. There is no domain at all. We tune the temperature carefully, once the system comes into the coexistence region, suddenly a lot domain bubbles are formed, and we can calculate the $\kappa = 0.997$ at this point. Increasing of the temperature has two effects:

1. The average domain size increases;

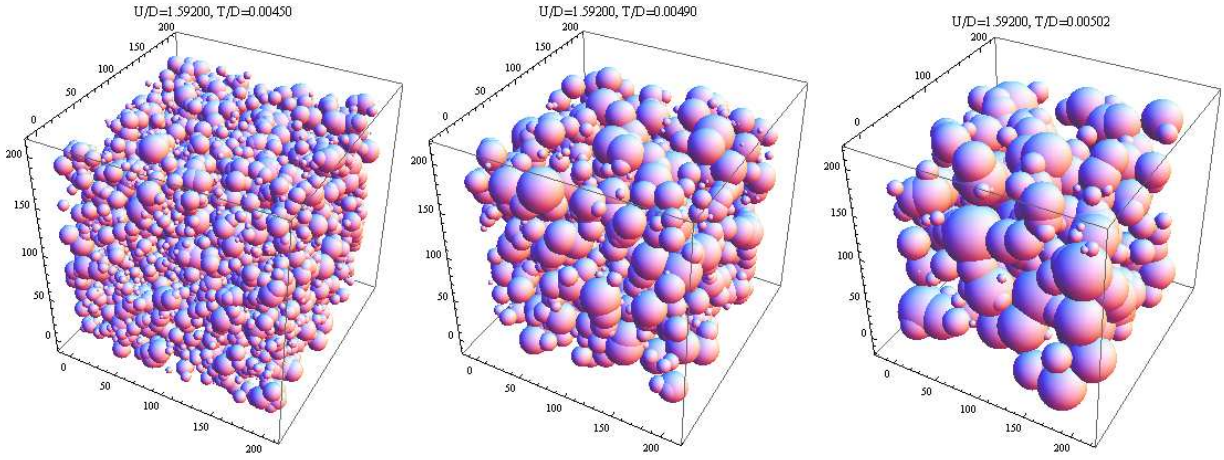

(a) (b) (c)

Figure 5.17.: Insulating domains inside a bulk metal at $T/D = 0.0045, 0.0049$ and 0.00502. Under these parameters, $\Delta F < 0$. These three figures show that insulating domains inside a bulk metal.

2. κ increases.

We find that the volume of the insulating domains are growing, and at the same time, the volume of metal is decreasing. As T comes close to the first order phase transition line, where $F_M = F_I$, we have $\kappa = 1$, which means $N_{domain} = N_{bulk}$. At this point, the insulating domains have the same volume as the metallic part. If we continue increasing T, the insulating state becomes more stable, and the excited metallic domains are created inside a bulk insulator. In this case, increasing of T makes the metallic domains smaller, which also means that the size of insulator is increasing.

Until now, the details of the temperature induced M-I transition is totally revealed. When U keeps unchanged, the increasing of temperature will make the volume of insulator increasing, and the metallic state volume decreasing. But there is still one thing which is contradictory to the experiment. In experiment, we observes that there exist only very few domains when the MIT begins. The word "few" here means that $N_{domain} \ll N_{bulk}$. In our calculation, we find that once the system comes into the coexistence region, κ is changed suddenly from 0 to 0.997, which is very close to 1. This is because, in our calculation, we are studying a homogeneous system, in this system, every part has the same temperature. This assumption can not be achieved in most experiments. In experiments, any change of the temperature will induce a temperature gradient inside the system, this will break the symmetry of the system, and our calculation is not suitable anymore. But, our calculation can be applied in a special case, if we make the temperature gradient small enough, e.g. close to 0, as it is done to prepare the over heated liquid. Any external disturbance will make this liquid boil. In this case, we find that the system changes suddenly form a liquid to gas. The volume ratio between liquid and gas is determined by the free energy difference of these two states.

Chapter 6.

Linear Resistivity behaviour during Temperature Induced Metal-Insulator Phase Transition

As we know, in real metals, the conductivity (or resistivity) originates in the electron scattering: scattering with impurity, scattering with phonons or scattering with electrons themselves. The resistivity due to electron-electron scattering increases as T^2 (Kaveh and Wiser, 1984) (Eq. (B.21)). In the high temperature region, the resistivity of a metal grows linearly with temperature according to Debye theory. The electron-phonon scattering gives a temperature dependence of T^5. Since the discovery of high-Tc superconductors, we find more kinds of resistivity behaviours (Mackenzie et al., 1996). Most high-T_c superconductors show linear resistivity at optimal doping in a very broad temperature range. Since most high-T_c superconductors have a $\mathrm{CuO_2}$ plane, Anderson extended the Luttinger liquid theory to 2-d to explain this phenomena (Schrieffer, 2007, Page 399). In Appendix B, Eq. (B.10), we showed that the resistivity is proportional to the inverse of scattering time: τ^{-1}, and we can calculate the resistivity behaviour by calculating τ^{-1}. We apply here Kubo's formula to derive the conductivity of the spectral function, and use this formula to calculate the conductivity of a metallic (or insulating) state. Based on these results and using the domain distribution function $P(R)$ from Section 5.3, a random network of resistors is created and we can calculate the total resistivity of this network, which appears to have a linear temperature dependence.

6.1. Conductivity of a Homogeneous System

We follow Kubo's derivation to calculate the conductivity formula. The idea is using the equation of motion to calculate the first order current response of a disturbance Hamiltonian H'. The expression for the current J_α reads

$$J_\alpha = \mathrm{Tr}\left[\rho(t)\, j\right], \tag{6.1}$$

where $\rho(t) = \rho_0 + f(t)$ is the density matrix, which contains the time independent part ρ_0 and the time dependent part $f(t)$. $\rho_0 = \exp\left[\beta(\Omega + \mu N - H_0)\right]$ describes the equi-

librium system, where the full Hamiltonian reads $H = H_0 + H'(t)$. The Heisenberg equation of motions can be used to calculate the derivative of the density matrix

$$\frac{d\rho(t)}{dt} = -i\left[H_0 + H'(t), \rho(t)\right], \tag{6.2}$$

and because ρ_0 is time independent, this equation can be written as

$$\frac{df(t)}{dt} = [H_0, f(t)] + [H'(t), \rho_0] + O\left(H'^2\right). \tag{6.3}$$

If we set $H'(-\infty) = 0$ and therefore $f(-\infty) = 0$, we have the following expression for $f(t)$

$$f(t) = -ie^{-iH_0t}\left\{\int_{-\infty}^{t} dt'\left[H'(t'), \rho_0\right]\right\}e^{iH_0t}. \tag{6.4}$$

The current J_α equals to

$$J_\alpha(r,\, t) = \mathrm{Tr}\left[f(t) j_\alpha(r)\right] \tag{6.5}$$

$$= -i\int_{-\infty}^{t} dt' \langle[j_\alpha(r),\, H'(t')]\rangle. \tag{6.6}$$

Here $H'(t) = \frac{i}{\omega} j_\alpha(\mathbf{q}) E_\alpha e^{-i\omega t}$ and E_α is the applied electric field. The DC conductivity $\sigma_{\alpha\beta}$ reads

$$\sigma_{\alpha\beta}(T) = \int_0^\infty dt\, e^{-st}\int_0^\beta d\lambda \langle j_\alpha(0)\, j_\beta(t + i\lambda)\rangle. \tag{6.7}$$

We consider a homogeneous system, therefore the conductivity is direction independent and we can write the conductivity as

$$\sigma(T) = \frac{1}{3}\int_0^\infty dt\, e^{-st}\int_0^\beta d\lambda \langle j_\alpha(0)\, j_\beta(t + i\lambda)\rangle. \tag{6.8}$$

Using the spectral function, the conductivity formula looks like this

$$\sigma = -\frac{\hbar e^2}{3m^2\pi}\sum_{k\sigma}\int d\epsilon \frac{\partial F(\epsilon)}{\partial \epsilon} A^2_{c\sigma}(k, \epsilon)\left(\frac{\partial E_k}{\partial k}\right)^2, \tag{6.9}$$

where F is the Fermi distribution function, and dE_k/dk is the energy dispersion relation. The momentum summation $\sum_k$ can be replaced by the integral over energy and density of states $N(\epsilon)$. We define $g(\epsilon)$ as the number of states from the bottom of the energy band to energy ϵ

$$g(\epsilon) = \int_{-D}^{\epsilon} d\epsilon' N(\epsilon'). \tag{6.10}$$

The energy dispersion can be written as

$$\frac{\partial E_k}{\partial k} = \frac{3a}{(6\pi^2)^{1/3}} \frac{g^{2/3}(\epsilon)}{N(\epsilon)}, \tag{6.11}$$

and the final conductivity reads

$$\sigma = -\left(\frac{3}{4\pi}\right)^{1/3} \frac{e^2}{\hbar a} \sum_{\sigma} \int d\omega d\epsilon \frac{dF(\omega)}{d\omega} A_{c\sigma}^2(\epsilon,\omega) \frac{g^{4/3}(\epsilon)}{N(\epsilon)}, \tag{6.12}$$

where $A_{c\sigma}(\epsilon,\omega) = \mathrm{Im}G_{c\sigma}(\epsilon,\omega - i0^+)/\pi$, $G_{c\sigma}^{-1}(\epsilon,\omega) = \omega + \mu - \epsilon - \Sigma_{c\sigma}(\omega)$, and a is the lattice constant. Since $G_{c\sigma}$ can be calculated through DMFT and NCA, we can obtain the conductivity easily. Since the term $(\frac{3}{4\pi})^{1/3}\frac{e^2}{\hbar a}$ before the summation sign is a constant, we choose this as the *unit* of the conductivity, and the inverse of this term as the unit of the resistivity.

6.2. Resistivity in the Phase Coexistence Region (No Domain)

First, let us look at the temperature dependence of the resistivity in the metallic phase. We have calculated the resistivity at different temperatures and at different Coulomb interactions as shown in Fig. 6.1. It shows that the resistivity in metallic state grows as T^2, as is predicted by the Fermi liquid theory (Eq. (B.21)).

Section B.1 shows that the scattering of electrons conserves momentum and energy. Under this constraint, we can prove that the inverse of the relaxation time τ_{ee}^{-1} is proportional to T^2. Since we have not included the phonon-electron interaction in our calculation scheme, this resistivity behaviour $\rho \propto T^2$ in the metallic phase is reasonable within our theory.

In the insulating phase, the $\rho(T)$ grows also monotonically. This is because this phase is not a real insulating phase. Usually, the definition of an insulator is that the energy gap Δ_{gap} is much greater than the thermal excitation k_BT. For example, the diamond is an insulator, which has $\Delta_{gap} \simeq 5\mathrm{eV} \sim 5.8 \times 10^3\mathrm{K}$, and it's easy to see that at room temperature $k_BT \ll \Delta_{gap}$. But now we are studying the high temperature region in the metal-insulator phase diagram, which is very close to the second order phase transition point, therefore we have $\Delta_{gap} \sim k_BT$ in our calculation. This relation can be confirmed by Fig. 6.3. So, strictly speaking, we show here a metal-bad metal phase transition. The resistivity of bad metal is 10-100 times the resistivity of a metal.

As the transport properties are dominated by the DOS on the Fermi surface $\rho(0)$, we show $\rho(0)$ as a function of T in Fig. 6.4. This figure shows that when we increase the temperature of the insulating state in the phase coexistence region, the DOS on the Fermi surface decreases. Therefore the conductivity also decreases according to

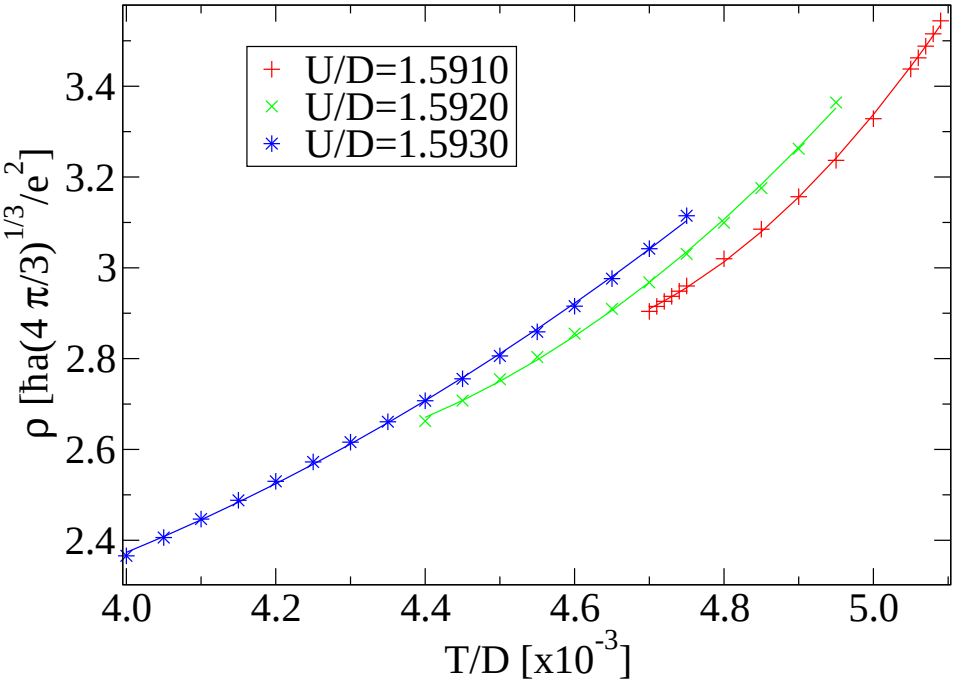

Figure 6.1.: $\rho(T)$ in metallic state. All data points are fitted by a function $f(x) = ax^2 + bx + c$. The variance of residuals reaches to the order of $10^{-5}Unit$, and $|c| \ll |b| \ll a$.

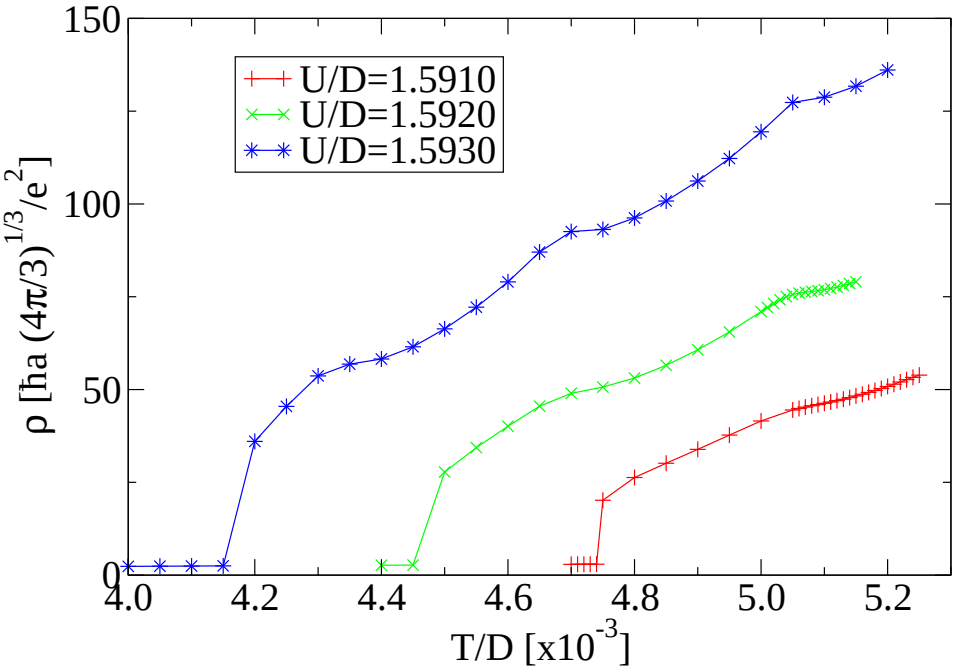

Figure 6.2.: $\rho(T)$ in insulating state.

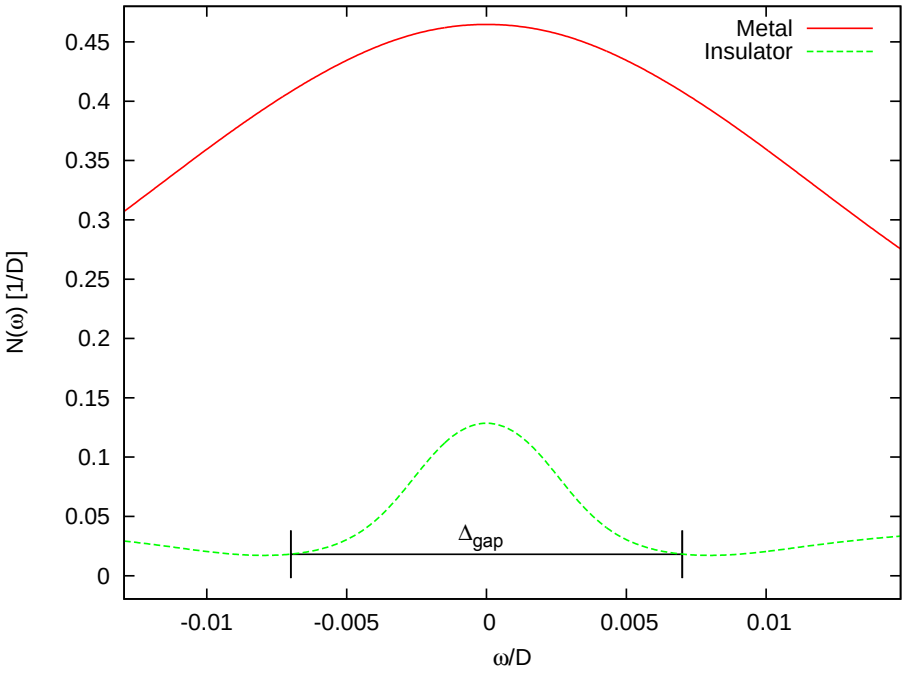

Figure 6.3.: This figure shows DOS $N(\omega)$ of metallic and insulating state around the Fermi energy with $\varepsilon_F = 0$, $U/D = 1.5930$, and $T/D = 0.0046$. When T is comparable to the energy gap Δ_{gap}, thermal excitations make the DOS of the insulating state (green dashed line) around the Fermi energy has a noticeable finite value. It shows also a peak around $\omega/D = 0$.

the Eq. (6.12), which explains the temperature dependence of the resistivity in the insulating phase in Fig. 6.2.

The Coulomb interaction U plays an important role in the bad metal resistivity. We find that the increase of U results in greater resistivity. In the metal resistivity calculation, if we increase U for 0.001D, the resistivity has a increase of $0.1Unit$, and the corresponding resistivity increase of the bad metal is about $25Unit$, which is 250 times larger than the metal resistivity increase (here $1Unit = \frac{\hbar a}{e^2}(\frac{4\pi}{3})^{1/3}$).

In Fig. 6.3, the red curve indicates the DOS of a metal, which shows a strong resonance peak on the Fermi energy. This resonance peak dominates the Fermi liquid behaviour of this metal and therefore we find $\rho \propto T^2$ for the metallic state. The green dashed line indicates the DOS of an insulator. This curve has a lower and upper Hubbard band (which extends to outside of this figure). In between of these two bands, $N(\omega)$ also shows a peak instead of a gap here, but this peak is much smaller than the metallic state DOS at the same parameters. This shape of an "insulating gap" results in the low resistivity of the non metallic state (here, the word "low" is used because it is lower than the usual insulator resistivity).

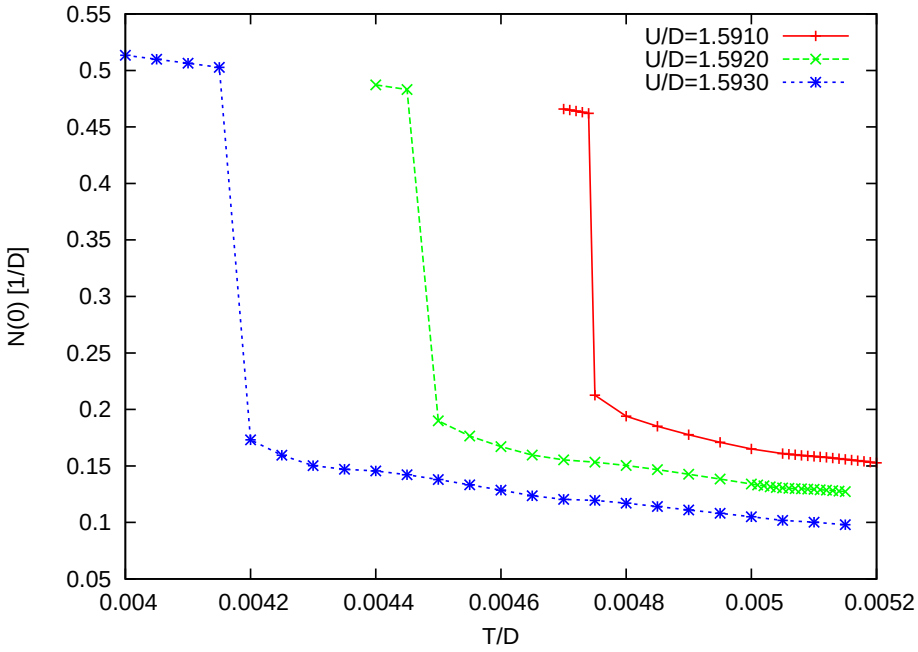

Figure 6.4.: Temperature dependence of $N(\omega = 0)$. The results are obtained by going from highto low temperatures.

6.3. Resistivity with Domains inside

In Chapter 5, we have proved that in the phase coexistence region, metallic/insulating domains can be thermally excited inside a bulk insulator/metal, and we can get the distribution function $P(R)$ based on the Boltzmann distribution function Eq. (5.4). The number of domains N_{domain} is determined by both Eq. (5.6) and Eq. (5.7). Since there exist domains inside the bulk material during the metal-insulator phase transition, and the resistivity of the insulating phase and the metallic phase are different, the system with domains inside forms a complex resistor network. The study of randomly distributed resistor network can be traced to early 1970's (Shante and Kirkpatrick (1971)). Kirkpatrick (1973) used extensions of percolation theory to study transport property (For introduction of percolation theory, please read the book by Stauffer and Aharony (2003)). They thought the percolation effects may play a role in the metal-semiconductor transitions in some disordered systems. In their study (and the references therein), they studied the resistivity as a function of filling number κ (defined in Eq. (5.7)). But since we know the distribution function $P(R)$ of this resistor network, we could follow their steps and calculate the resistivity of the system with domains which obey the distribution function $P(R)$.

To calculate the voltage on every site V_i, we use the iteration form of Kirchhoff

equation (Eq. 4.7 in Kirkpatrick (1973))

$$V_i = \frac{\sum_j g_{ij} V_j}{\sum_j g_{ij}}, \tag{6.13}$$

where $g_{ij} = a\sigma_{ij}$, a is the lattice constant, and σ_{ij} is the conductivity between site i and j. Fig. 6.5 shows the sketch of one domain bubble inside a bulk material. We connect every nearest site with a resistor, and the conductivity of this resistor is decided by its position. If this resistor lies inside the domain, it has the conductivity of the domain. If it lies outside of the domain, its conductivity equals the conductivity of the bulk material.

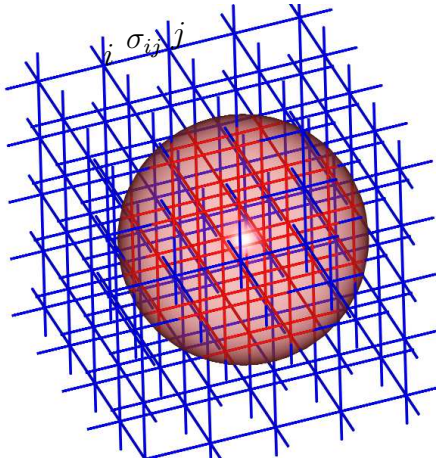

Figure 6.5.: Sketch of a resistor network. Red and blue color indicate different values of σ_{ij}. i, j goes over all the lattice sites, and j is the nearest neighbour of site i.

We have constructed a cubic resistor network [size($i \times j \times k$): $200 \times 200 \times 200$]. We set $V_{i,j,0} = 0$, and $V_{i,j,200} = 1$ as the boundary condition. For every distribution function $P(R)$, we use a random number generator to generate multiple configurations. Then we use Eq. (6.13) to calculate the V_i on each site. Here by, we can calculate the total resistivity of the system. The iteration of Eq. (6.13) converges very slowly, but it did converge without any tricks needed.

A by-product of this random resistor network calculation is the voltage distribution on each layer (see Fig. 6.6). The color stands for the voltage value. As we have discussed in Section 5.3, the size of the domain bubble increases as T increases in the case of a stable metallic state. The shadow in Fig. 6.6 reflects the domain size in this case. At $T/D = 0.0042$, the domain sizes are small and the number of domains are large. When T is increased to $T/D = 0.0048$, which is in the vicinity of the first order phase transition line, the domain sizes are very big and the number of domains decreases. And because the volume of insulator domains also increases with T, we find that the area of the blue color also increases by going from low to high temperatures (in the $F_M < F_I$ region).

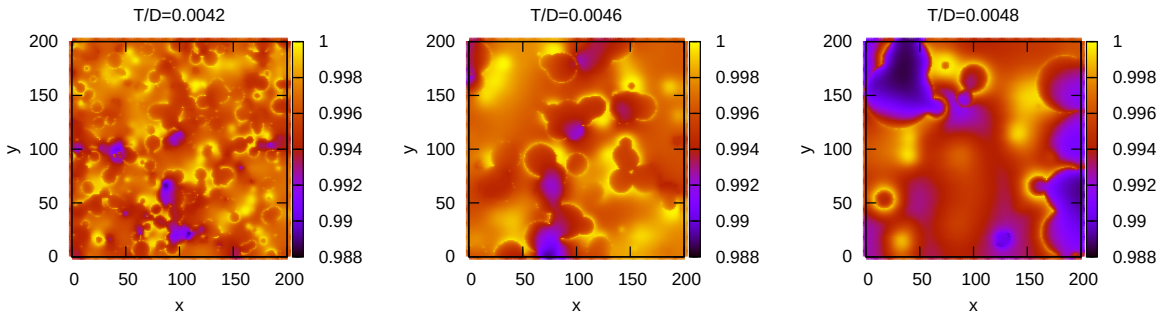

(a) (b) (c)

Figure 6.6.: The domains are profiled on the voltage distribution figure. We draw here the voltage distribution on layer $z = 199$. Here $U/D = 1.5930$, and the boundary condition is $V_{x,y,z=200} = 1$.

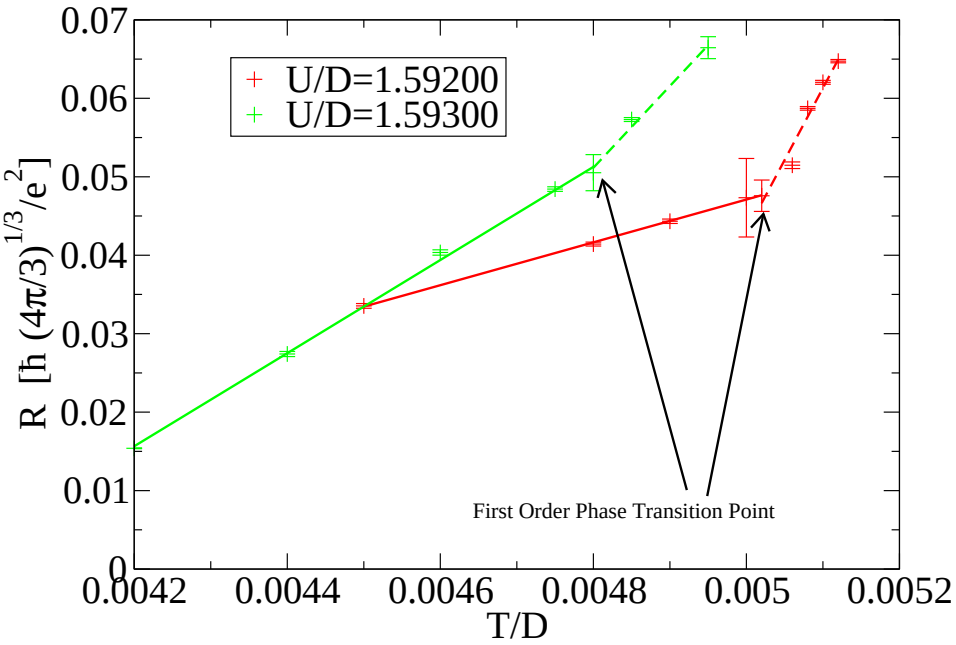

Figure 6.7.: The total resistivity of the cubic random resistor network shows a linear temperature dependence. The standard deviation of resistivity is very large when the system is very close to the first order phase transition point. The slope also changes at this point.

The total resistivity of the network with domains of a distribution $P(R)$ is shown in Fig. 6.7. It is obvious, that the resistivity increases linearly with temperature. This linear resistivity behaviour has a kink on the first order phase transition point. Below this point, the metallic state is the stable state, and above this point the insulating state is the stable state. Starting from this point, we can draw two lines towards the insulating side and the metallic side. And we find that stronger interaction U makes the linear resistivity range bigger. Smaller interaction U makes the kink more pronounced. The linear resistivity range depends on the interaction U. When U is small, this linear resistivity can extends from 0 to $0.004D$ (This range can be read from the phase diagram in Fig. 4.7). If we replace the half-bandwidth value D with the value of VO_2: $\sim 5\mathrm{eV}$ (this value can be read from the photo emission experiment in Shin et al. (1990)), this temperature ranges from $0\mathrm{K}$ to $230\mathrm{K}$. We think, this domain effect may be an origin of the problem of linear resistivity behavior which was introduced in Chapter 1.

Summary

In this thesis, we have investigated the micro-domain formation near the first order Mott-Hubbard metal-insulator phase transition. As this is a first order phase transition, we can always find a phase coexistence region in the phase diagram Fig. 1.3. The first order phase transition line divides this phase coexistence region into two parts. On the $U < U_{1st}$ side, the metallic state is stable and the insulating state is metastable. It is the contrary on the $U > U_{1st}$ side. It is quite possible that the high energy domains can be thermally excited from a low energy state to the metastable state. In between, there forms a domain wall. The formation of the domain wall is studied in Chapter 5 using the spatially resolved DMFT (or also called LDMFT, see Section 3.3). It is worth to emphasize that we start with a homogeneous model (the Hubbard model), and end with the non-homogeneous results (the domain walls). The size of the domain wall diverges as $\Delta F \to 0$ (Fig. 5.7). Besides this, we also find that because the high energy meta-stable state tends to transit to the low energy state, the domain wall looks like drifting to the side of the high energy states.

With the results of the DOS on the domain wall, we can calculate the domain size distribution function $P(R)$ based on the Boltzmann distribution function. The position of the $P(R)$ function's peak stands for the most possible domain size. If we keep U fixed and increase T from the metallic state to the first order phase transition point, we find the size of the insulating domain increases monotonically. When T is above the first order phase transition point, $P(R)$ describes the metallic domain inside an insulating bulk, and we find the size of the metallic domains decreases as an increasing T. This reveals the detail in the metal-insulator phase transition.

The conductivity in the metal-insulator phase transition is also studied. With the normal DMFT, we can calculate the DOS of the metallic phase and the insulating phase in the phase coexistence region. Therefore, we can calculate the conductivity. The resistivity in the metallic state (in the phase coexistence region) increases with temperatures as T^2, which is in accordance with the Fermi liquid theory. The resistivity in the insulating state increases also monotonically with T. When the excitation of domains is considered, we construct a $200 \times 200 \times 200$ lattice and use the random number generator to simulate the domain excitation. In this simulation, the domain size distribution function $P(R)$ is obeyed. This is different from the random resistor network problem that Kirkpatrick (1973) has studied within the percolation theory. The total resistivity of this random resistor network shows a linear T dependence (see Fig. 6.7). A kink is found in the first order phase transition point.

Appendix A.

Eigenvalues of tridiagonal matrices

Usually, it is very difficult to calculate the eigenvalues of a large matrix, but the structure of a hopping matrix is one kind of tridiagonal matrix. The structure of such matrices provides us with an easy way to calculate the eigenvalues. We have the $n \times n$ hopping matrix as

$$M_{n\times n} = \begin{pmatrix} 0 & t & & & \\ t & 0 & t & & \\ & t & 0 & t & \\ & & t & 0 & \ddots \\ & & & \ddots & \ddots \end{pmatrix}, \tag{A.1}$$

and we want to solve the eigenvalue problem defined by

$$M\,q = \lambda q, \tag{A.2}$$

where $\lambda \in \mathrm{R}$ and $q^{\mathrm{T}} = \begin{pmatrix} q_1, & \ldots, & q_n \end{pmatrix} \neq 0$. The multiplication of the matrix M and a vector q reads

$$t\,q_{j-1} + t\,q_{j+1} = \lambda q_j, \qquad j = 1, \ldots, n \tag{A.3}$$

$$q_0 = q_{n+1} = 0. \tag{A.4}$$

To solve such coupled equations, we should use the characteristic polynominal

$$p(r) = t\,r^2 - \lambda r + t. \tag{A.5}$$

If the roots of $p(r)$ are r_1 and r_2, the solutions of the above equations are

$$q_j = \alpha r_1^j + \beta r_2^j, \tag{A.6}$$

where $j = 0, \ldots, n+1$. The boundary condition (A.4) can be written as

$$q_0 = \alpha + \beta = 0 \mapsto \alpha = -\beta, \tag{A.7}$$

then we have

$$q_j = \alpha(r_1^j - r_2^j). \tag{A.8}$$

The condition $q_{n+1} = 0$ provides us

$$\alpha(r_1^{n+1} - r_2^{n+1}) = 0 \Leftrightarrow (\frac{r_1}{r_2})^{n+1} = 1. \tag{A.9}$$

And the algebra tells us that

$$r_1 r_2 = t/t = 1, \tag{A.10}$$

we can eliminate r_2 in (A.9) and we have

$$(r_1^2)^{n+1} = 1. \tag{A.11}$$

The root r_1 reads

$$r_{1,s} = e^{i\pi\frac{s}{n+1}}, \tag{A.12}$$

and $r_2 = r_1^*$

$$r_{2,s} = e^{-i\pi\frac{s}{n+1}}. \tag{A.13}$$

Finally, we get the corresponding eigenvalue

$$\lambda_s = t(r_{1,s} + r_{2,s}) \tag{A.14}$$

$$= 2t\cos\frac{s\pi}{n+1}, \quad s = 1, \ldots, n. \tag{A.15}$$

Appendix B.

Boltzmann Formulation

Consider a electron as a plain wave propagating in an electric field $\mathbf{E}$, the momentum $\mathbf{p} = \hbar\mathbf{k}$ changes according to the equation

$$\frac{d\mathbf{k}}{dt} = e\,\mathbf{E}/\hbar. \tag{B.1}$$

Thus, the electron distribution function changes from the equilibrium distribution $f_0(k)$ to a new state $f(k)$. The resistivity is finite when the electron is scattered by any impurities, phonons, or defects of lattice. This scattering effect makes the electron back towards the equilibrium distribution in a relaxation time τ. Thus, the disturbance of the distribution function $\delta f = f - f_0$ changes as

$$\frac{d\delta f}{dt} = -\frac{\delta f}{\tau}. \tag{B.2}$$

The right side of Eq. (B.2) can be written as

$$\frac{d(f - f_0)}{dt} = \frac{d\mathbf{k}}{dt} \cdot \nabla_k f(\mathbf{k}) = e\,\mathbf{E} \cdot \nabla_k f(\mathbf{k})/\hbar, \tag{B.3}$$

considering the right part of Eq. (B.2), we have

$$f = f_0 + \tau\, e\,\mathbf{E} \cdot \nabla_k f(\mathbf{k})/\hbar. \tag{B.4}$$

The current is defined by

$$\mathbf{j} = -e\langle \mathbf{v}_k \rangle = -2e \int f(\mathbf{k}) \frac{\hbar\mathbf{k}}{m} \frac{d\mathbf{k}}{(2\pi)^3}, \tag{B.5}$$

Here the number 2 is introduced because of the spin. With Eq. (B.4), we replace $f(\mathbf{k})$ in Eq. (B.5), and because the current is zero when there is no field, we have

$$\mathbf{j} = -2e^2 \int \tau \mathbf{v}_\mathbf{k} (\mathbf{E} \cdot \mathbf{v}_\mathbf{k}) \frac{\partial f_0}{\partial \epsilon_\mathbf{k}} \frac{d\mathbf{k}}{(2\pi)^3}. \tag{B.6}$$

Compairing Eq. (B.6) with the definition of conductivity

$$j_\alpha = \sum_\beta \sigma_{\alpha\beta} E_\beta, \tag{B.7}$$

we can write the conductivity as

$$\sigma_{\alpha\beta} = -2e^2 \int \tau v_\alpha(\mathbf{k}) v_\beta(\mathbf{k}) \frac{\partial f_0}{\partial \epsilon_\mathbf{k}} \frac{d\mathbf{k}}{(2\pi)^3}. \tag{B.8}$$

If we have a homogeneous Fermi system, the off-diagonal elements in conductivity tensor are zero, and all three diagonal elements are equal. The conductivity formula has a simpler form

$$\sigma = -\frac{2e^2}{3} \int v_\mathbf{k}^2 \tau \frac{\partial f_0}{\partial \epsilon_\mathbf{k}} \frac{d\mathbf{k}}{(2\pi)^3}. \tag{B.9}$$

If we insert the Fermi-Dirac distribution at $T = 0$ into Eq. (B.9), and assume free electrons, the conductivity reads

$$\sigma = \frac{ne^2\tau}{m}. \tag{B.10}$$

The problem is now to find an expression for the relaxation time τ. Since τ is defined as the time that the electrons take to be scattered back to the equilibrium state, we should calculate the collision rate of the distribution function df/dt. The change of the distribution is equal to the number of electrons which are scattered from $\mathbf{k}$ to $\mathbf{k}'$ minus the number of electrons which are scattered from $\mathbf{k}'$ to $\mathbf{k}$. As we have learned from quantum mechanics text books, the number of electrons scattered from $\mathbf{k}$ to $\mathbf{k}'$ is propertional to the scattering rate $W(\mathbf{k}, \mathbf{k}')$, $f(\mathbf{k})$, the average occupation of the state $\mathbf{k}$, and $1 - f(\mathbf{k}')$, the probability that $\mathbf{k}'$ is unoccupied. Thus, the number of electrons which are scattered from $\mathbf{k}$ to $\mathbf{k}'$ in time δt in unit volume is

$$\int_{k'} 2f(\mathbf{k}) \frac{d\mathbf{k}}{(2\pi)^3} W(\mathbf{k}, \mathbf{k}') [1 - f(\mathbf{k}')] \frac{d\mathbf{k}'}{(2\pi)^3} \delta t.$$

We can write down the number of electrons which are scattered from $\mathbf{k}'$ to $\mathbf{k}$ in time δt in unit volume with the same idea, just exchange $\mathbf{k}$ with $\mathbf{k}'$,

$$\int_{k'} 2[1 - f(\mathbf{k})] \frac{d\mathbf{k}}{(2\pi)^3} W(\mathbf{k}', \mathbf{k}) f(\mathbf{k}') \frac{d\mathbf{k}'}{(2\pi)^3} \delta t.$$

Therefore we get the total scattering rate equation as

$$2\delta f(\mathbf{k}) \frac{d\mathbf{k}}{(2\pi)^3} = -c_{imp} \int 2 \left\{ f(\mathbf{k}) \left[1 - f(\mathbf{k}')\right] - f(\mathbf{k}') \left[1 - f(\mathbf{k})\right] \right\} W(\mathbf{k}, \mathbf{k}') \frac{d\mathbf{k}}{(2\pi)^3} \frac{d\mathbf{k}'}{(2\pi)^3} \delta t, \tag{B.11}$$

here we used the property that $W(\mathbf{k}, \mathbf{k}')$ is symmetric, and the minus sign in front of the integration means that the number of electrons at state $\mathbf{k}$ decreases as electrons

are scattered out of state $\mathbf{k}$. Thus, we have

$$\left(\frac{df}{dt}\right)_s = -c_{imp}\int \{f(\mathbf{k})\left[1-f(\mathbf{k}')\right] - f(\mathbf{k}')\left[1-f(\mathbf{k})\right]\} W(\mathbf{k},\mathbf{k}')\frac{d\mathbf{k}'}{(2\pi)^3}. \tag{B.12}$$

With (B.3), we get

$$-c_{imp}\int \{f(\mathbf{k}) - f(\mathbf{k}')\} W(\mathbf{k},\mathbf{k}')\frac{d\mathbf{k}'}{(2\pi)^3} = e\,\mathbf{E}\cdot\nabla_k f(\mathbf{k})/\hbar. \tag{B.13}$$

Substituting (B.4) into (B.13), and keep only the first order of $\mathbf{E}$, we obtain an expression for τ

$$\tau^{-1} = \hbar c_{imp}\int W(\mathbf{k},\mathbf{k}')(1-\cos\theta')\frac{d\mathbf{k}'}{(2\pi)^3}. \tag{B.14}$$

The factor $1-\cos\theta'$ means that large angle scattering contributes more to τ. θ' is the angle between $\mathbf{k}$ and $\mathbf{k}'$. Since the relaxation time can be calculated from the scattering matrix, we can calculate the conductivity σ.

For example, if we consider only the scatter between electron and impurity (Hewson (1993)), we have

$$\tau^{-1} = \frac{3\pi c_{imp} n V^2}{2\hbar\varepsilon_F}, \tag{B.15}$$

and the resistivity R_{imp}reads

$$R_{imp} = \frac{3\pi c_{imp} m V^2}{2e^2\hbar\varepsilon_F}. \tag{B.16}$$

The resistivity R_{imp} is temperature independent.

B.1. Electron-Electron Scattering term τ_{ee}^{-1}

In a $3d$ system, an electron in state $\mathbf{k}_1$ is scattered to $\mathbf{k}_3$, and its energy is changed from $E(\mathbf{k}_1)$ to $E(\mathbf{k}_3)$. At the same time, another electron is also scattered from $\mathbf{k}_2$ to $\mathbf{k}_4$. According to the Fermi liquid theory, only electrons on the Fermi surface take part in this scattering. Therefore, the number of electrons on the Fermi surface is proportional to k_BT. The energy conservation law requires that

$$E(\mathbf{k}_1) + E(\mathbf{k}_2) = E(\mathbf{k}_3) + E(\mathbf{k}_4), \tag{B.17}$$

and the momentum conservation

$$\mathbf{k}_1 + \mathbf{k}_2 = \mathbf{k}_3 + \mathbf{k}_4 \tag{B.18}$$

must also be fullfilled.

Thus, the scattering rate in state $\mathbf{k}_1$is given by

$$\tau_{ee}^{-1}(\mathbf{k}_1) = \sum_{k_2,k_3,k_4} P(\mathbf{k}_1, \mathbf{k}_2; \mathbf{k}_3, \mathbf{k}_4). \tag{B.19}$$

Since we have four constraints, the summation on $\mathbf{k}_2$, $\mathbf{k}_3$, and $\mathbf{k}_4$ has only five independent variables. If we define $\mathbf{q} = \mathbf{k}_3 - \mathbf{k}_2$, we have

$$\tau_{ee}^{-1} = \sum_{\mathbf{q},E(\mathbf{k}_2),E(\mathbf{k}_3)} P(\mathbf{q}, E(\mathbf{k}_2), E(\mathbf{k}_3)). \tag{B.20}$$

Since $E(\mathbf{k}_2)$ and $E(\mathbf{k}_3)$ is proportional to k_BT/E_F, the resistivity term for $e-e$ scattering leads to

$$\tau_{ee}^{-1} \propto T^2. \tag{B.21}$$

B.2. Electron-Phonon Scattering term τ_{e-ph}^{-1}

The electron-phonon interaction Hamiltonian is written as

$$H_{e-ph} = \sum_{\mathbf{q},\mathbf{k},\mathbf{k}'} C_{\mathbf{q}} \Delta_{\mathbf{k}',\mathbf{k}+\mathbf{q}} c_{\mathbf{k}'}^{\dagger} c_{\mathbf{k}} b_{\mathbf{q}} + h.c., \tag{B.22}$$

where

$$\Delta_{\mathbf{k}',\mathbf{k}+\mathbf{q}} = \langle \mathbf{k}' | e^{i\mathbf{q}\cdot\mathbf{r}} | \mathbf{k} \rangle = \sum_{\mathbf{G}} \delta(\mathbf{k}' - \mathbf{k} \pm \mathbf{q} - \mathbf{G}), \tag{B.23}$$

$C_{\mathbf{q}}$ is the coefficient. The transition probability can be calculated by using Fermi's golden rule

$$W_{fi} = \frac{2\pi}{\hbar} |T_{fi}|^2 \delta(E_f - E_i), \tag{B.24}$$

where i and f stand for the initial and final state. We assume $\mathbf{G} = 0$, and obtain

$$W_{\mathbf{k}-\mathbf{q},\mathbf{k}} = \frac{2\pi}{\hbar} |C_{\mathbf{q}}|^2 \left\{ (N_q + 1)\delta\left[E(\mathbf{k}-\mathbf{q}) - E(\mathbf{k}) + \hbar\omega_{\mathbf{q}}\right] + N_{-q}\delta\left[E(\mathbf{k}-\mathbf{q}) - E(\mathbf{k}) - \hbar\omega_{\mathbf{q}}\right] \right\}. \tag{B.25}$$

If $k_BT \ll \hbar\omega_D$, the thermal phonons with energy $\hbar\omega_q \sim k_BT$ are most important, and the δ function in the bracket can be written as

$$\delta\left[\frac{(\mathbf{p}-\hbar\mathbf{q})^2}{2m} - \frac{\mathbf{p}^2}{2m} \pm \hbar\omega_{\mathbf{q}}\right] = \frac{m}{\hbar pq}\delta\left[\cos\theta - \frac{\hbar q}{2p} \pm \frac{ms}{q}\right], \tag{B.26}$$

where s is the speed of sound. The integration over q gives the contribution of q^3, and the integration over θ introduced a term $(1-\cos\theta)$. Moreover, when $\cos\theta \ll 1$, we

have $1 - \cos\theta \simeq \theta^2/2 \sim (\hbar q/p_F)^2$. Thus, the final τ_{e-ph}^{-1} is proportional to q^5, and reads

$$\tau_{e-ph}^{-1} \propto T^5. \tag{B.27}$$

List of Figures

Bibliography

A. A. Abrikosov, L. P. Gorkov, and I. E. Dzyaloshinski. *Quantum field theory in statistical physics*. 1965.

P. B. Allen, H. Berger, O. Chauvet, L. Forro, T. Jarlborg, A. Junod, B. Revaz, and G. Santi. Transport properties, thermodynamic properties, and electronic structure of $SrRuO_3$. *Phys. Rev. B*, 53(8):4393–4398, Feb 1996.

P. W. Anderson. Localized magnetic states in metals. *Phys. Rev.*, 124(1):41, 1961.

Gordon Baym. Self-consistent approximations in many-body systems. *Phys. Rev.*, 127 (4):1391, 1962.

Gordon Baym and Leo P. Kadanoff. Conservation laws and correlation functions. *Phys. Rev.*, 124(2):287, 1961.

H. Berger, L. Forro, and D. Pavuna. On linear resistivity from $1\mathrm{K} \sim 10^3 K\mathrm{K}$ in Sr_2RuO_4 single crystal. *Europhys. Lett.*, 41(5):531, 1998.

U. Brandt and C. Mielsch. Thermodynamics and correlation functions of the Falicov-Kimball model in large dimensions. *Z. Phys. B*, 75:365, 1989.

U. Brandt and C. Mielsch. Thermodynamics of the Falicov-Kimball model in large dimensions ii. *Z. Phys. B*, 79:295, 1990.

U. Brandt and C. Mielsch. Free energy of the Falicov-Kimball model in large dimensions. *Z. Phys. B*, 82:37, 1991.

W. F. Brinkman and T. M. Rice. Application of gutzwiller's variational method to the metal-insulator transition. *Phys. Rev. B*, 2(10):4302–4304, Nov 1970.

T. A. Costi, J. Kroha, and P. Wölfle. Spectral properties of the anderson impurity model: Comparison of nrg and nca results. *Phys. Rev. B*, 53:1850, 1996.

J. H. de Boer and E. J. W. Verwey. Semi-conductors with partially and with completely filled 3d-lattice bands. *Proc. Roy. Soc.*, 49:59, 1937.

D. M. Edwards and A. C. Hewson. Comment on Hubbard's Theory of the Mott Transition. *Rev. Mod. Phys.*, 40(4):810, 1968.

B. Fisher. Metal-semiconductor domain configurations during switching of VO_2 single crystals. *J. Phys. C*, 9:1201, 1976.

A. Georges and G. Kotliar. Hubbard model in infinite dimensions. *Phys. Rev. B*, 45 (12):6479, 1992.

A. Georges, G. Kotliar, and Q. Si. Strongly correlated systems in infinite dimensions and their zero dimensional counterparts. *Int. J. Mod. Phys. B*, 6:705, 1992.

A. Georges, G. Kotliar, W. Krauth, and M. J. Rozenberg. Dynamical mean-field theory of strongly correlated fermion systems and the limit of infinite dimensions. *Rev. Mod. Phys.*, 68(1):13, 1996.

M. Gurvitch and A. T. Fiory. Resistivity of $La_{1.825}Sr_{0.175}CuO_4$ and $YBa_2Cu_3O_7$ to 1100K: Absence of Saturation and Its Implications. *Phys. Rev. Lett.*, 59(12):1337, 1987.

Martin C. Gutzwiller. Correlation of electrons in a narrow s band. *Phys. Rev.*, 137: A1726–A1735, Mar 1965.

A. C. Hewson. *The Kondo Problem to Heavy Fermions*. 1993.

J. E. Hirsch and R. M. Fye. Monte Carlo Method for Magnetic Impurities in Metals. *Phys. Rev. Lett.*, 56(23):2521–2524, Jun 1986.

J. Hubbard. Electron correlations in narrow energy bands. *Proc. Roy. Soc. A*, 276:238, 1963.

J. Hubbard. Electron correlations in narrow energy bands iii. an improved solution. *Proc. Roy. Soc. A*, 281:401, 1964a.

J. Hubbard. Electron correlations in narrow energy bands ii. the degenerate band case. *Proc. Roy. Soc. A*, 277:237, 1964b.

M. Imada, A. Fujimori, and Y. Tokura. Metal-Insulator Transitions. *Rev. Mod. Phys.*, 70:1039, 1998.

L. B. Ioffe and G. Kotliar. Transport phenomena near the Mott transition. *Phys. Rev. B*, 42:10348, 1990.

L. B. Ioffe and A. I. Larkin. Gapless fermions and gauge fields in dielectrics. *Phys. Rev. B*, 39:8988, 1989.

L. B. Ioffe and P. B. Wiegmann. Linear temperature dependence of resistivity as evidence of gauge interaction. *Phys. Rev. Lett.*, 65:653, 1990.

V. Janiš. A new construction of thermodynamic mean-field theories of itinerant fermions: application to the falicov-kimball model. *Z. Phys. B*, 83:227, 1991.

V. Janiš and D. Vollhardt. Comprehensive mean field theory for the hubbard model. *Int. J. Mod. Phys. B*, 6(5):731, 1992a.

V. Janiš and D. Vollhardt. Coupling of quantum degrees of freedom in strongly interacting disordered electron systems. *Phys. Rev. B*, 46(24):15712–15715, Dec 1992b.

K. Kato, E. Nishibori, M. Takata, M. Sakata, T. Nakano, K. Uchihira, M. Tsubota, F. Iga, and T. Takabatake. The Metal Insulator Transition in $Y_{1-x}Ca_xTiO_3$ Caused by Phase Separation.

M. Kaveh and N. Wiser. Electron Electron-Scattering in Conducting Materials. *Adv. Phys.*, 33:257–372, 1984.

H. Keiter and J. C. Kimball. Diagrammatic approach to the anderson model for dilute alloys. *J. Appl. Phys.*, 42:1460, 1971.

S. Kirkpatrick. Percolation and conduction. *Rev. Mod. Phys.*, 45(4):574–588, Oct 1973.

. Kojima, Y. Kuramoto, and M. Tachiki. Self-consistent perturbation theory for dynamics of valence fluctuations ii. application to ce systems. *Z. Phys. B*, 53:293, 1984.

Gabriel Kotliar and Andrei E. Ruckenstein. New functional integral approach to strongly correlated fermi systems: The gutzwiller approximation as a saddle point. *Phys. Rev. Lett.*, 57(11):1362, 1986.

J. Kroha and P. Wölfle. Diagrammatic theory of anderson impurity models: Fermi and nonfermi liquid behavior. In *Open Problems in Strongly Correlated Electron Systems*, pages 101–10, 2001a.

J. Kroha and P. Wölfle. Fermi and non-fermi liquid behavior of quantum impurity models: A diagrammatic pseudo-particle approach. *cond-mat*, (105491):105491, 2001b.

J. Kroha, P. Wölfle, and T. A. Costi. Unified description of fermi and non-fermi liquid behavior in a conserving slave boson approximation for strongly correlated impurity models. *Phys. Rev. Lett.*, 79:261, 1997.

Y. Kuramoto. Self-consistent perturbation theory for dynamics of valence fluctuations i. single-site theory. *Z. Phys. B*, 53:37, 1983.

Y. Kuramoto. Self-consistent perturbation theory for dynamics of valence fluctuations iv. tm systems with two magnetic valence states. *Z. Phys. B*, 65:29, 1986.

Y. Kuramoto and H. Kojima. Self-consistent perturbation theory for dynamics of valence fluctuations iii. zero-temperature limit. *Z. Phys. B*, 57:95, 1984.

L. D. Landau and E. M. Lifshitz. *Statistical Physics Part 1*. 3 edition, 1980.

R. Lopez, L. C. Feldman, and R. F. Haglund. Size-dependent optical properties of VO_2 nanoparticle arrays. *Phys. Rev. Lett.*, 93(17):177403, Oct 2004.

A. P. Mackenzie, S. R. Julian, D. C. Sinclair, and C. T. Lin. Normal-state magneto-transport in superconducting $\mathrm{Tl_2Ba_2CuO_{6+\delta}}$ to millikelvin temperatures. *Phys. Rev. B*, 53:5848, 1996.

S. Martin, A. T. Fiory, R. M. Fleming, L. F. Schneemeyer, and J. V. Waszczak. Temperature Dependence of the Resistivity Tensor in Superconducting $\mathrm{Bi_2Sr_{2.2}Ca_{0.8}Cu_2O_8}$ Crystals. *Phys. Rev. Lett.*, 60:2194, 1988.

W Metzner. Correction. *Phys. Rev. B*, 39(16):12339, 1989.

W. Metzner and D. Vollhardt. Correlated Lattice Fermions in d=∞ Dimensions. *Phys. Rev. Lett.*, 62(3):324, 1989a.

W Metzner and D. Vollhardt. Ground-state energy of the d = 1, 2, 3 dimensional hubbard-model in the weak-coupling limit. *Phys. Rev. B*, 39(7):4462, 1989b.

Tôru Moriya, Yoshinori Takahashi, and Kazuo Ueda. Antiferromagnetic Spin Fluctuations and Superconductivity in Two-Dimensional Metals -A Possible Model for High T_c Oxides. *J. Phys. Soc. Jpn.*, 59:2905, 1990.

N. F. Mott. Metal-insulator transition. *Rev. Mod. Phys.*, 40(4):677–683, Oct 1968.

N.F. Mott. The basis of the electron theory of metals, with special reference to the transition metals. *Proc. Phys. Soc. A*, 62:416, 1949.

N.F. Mott. On the transition to metallic conduction in semiconductors. *Can. J. Phys.*, 34:1356, 1956.

N.F. Mott. The transition to the metallic state. *Phil. Mag. B*, 6:287, 1961.

N.F. Mott. *Metal-Insulator Transition*. 1990.

E. Müller-Hartmann. Fermions on a lattice in high dimensions. *Int. J. Mod. Phys. B*, 3: 2169, 1989a.

E. Müller-Hartmann. Correlated fermions on a lattice in high dimensions. *Z. Phys. B*, 74:507, 1989b.

E. Müller-Hartmann. The Hubbard model at high dimensions: some exact results and weak coupling theory. *Z. Phys. B*, 76(2):211–217, 1989c.

H. Nakao, S. Kodama, K. Kiyoto, D. Bizen, Y. Murkami, M. Tsubota, F. Iga, and T. Takabatake. Metal-insulator transition in $Y_{1-x}Ca_xTiO_3$ studied by X-ray scattering. *Journal of Magnetism and Magnetic Materials*, 310:895–897, 2007.

P. Nozières. A "fermi-liquid" description of the Kondo problem at low temperatures. *J. Low. Temp. Phys.*, 17:31, 1974.

D. Pavuna, H. Berger, and L. Forro. Linear resistivity from similar to 1 to 1050 K in $Sr_2RuO_{4-\delta}$ single crystals grown by the flux technique. *Journal of the European Ceramic Society*, 19:1515, 1999.

Th. Pruschke and N. Grewe. The Anderson model with finite Coulomb repulsion. *Z. Phys. B*, 74:439, 1989.

Th. Pruschke, D. L. Cox, and M. Jarrell. Hubbard model at infinite dimensions: Thermodynamic and transport properties. *Phys. Rev. B*, 47:3553, 1993.

M. J. Rozenberg, X. Y. Zhang, and G. Kotliar. Mott-Hubbard transition in infinite dimensions. *Phys. Rev. Lett.*, 69(8):1236, 1992.

M. J. Rozenberg, G. Kotliar, and X. Y. Zhang. Mott-Hubbard transition in infinite dimensions. II. *Phys. Rev. B*, 49(15):10181, 1994a.

M. J. Rozenberg, Goetz Moeller, and Gabriel Kotliar. The metal-insulator transition in the hubbard model at zero temperature ii. *cond-mat*, page 9402056, 1994b.

M.J. Rozenberg, G. Kotliar, H. Kajueter, G. A. Thomas, D. H. Rapkine, J. M. Honig, and P. Metcalf. Optical conductivity in mott-hubbard systems. *Phys. Rev. Lett.*, 75: 105, 1995.

J. R. Schrieffer, editor. *Handbook of High-Termperature Superconductivity*. Springer, 2007.

Vinod K. S. Shante and Scott Kirkpatrick. An introduction to percolation theory. *Adv. Phys.*, 20:325, 1971.

S. Shin, S. Suga, M. Taniguchi, M. Fujisawa, H. Kanzaki, A. Fujimori, H. Daimon, Y. Ueda, K. Kosuge, and S. Kachi. Vacuum-ultraviolet reflectance and photoemission study of the metal-insulator phase transition in VO_2, V_6O_{13}, and V_2O_3. *Phys. Rev. B*, 41:4993, 1990.

Dietrich Stauffer and Amnon Aharony. *Introduction to Percolation theory*. Taylor & Francis, 2nd edition, 2003. ISBN 0-7484-0253-5.

C. M. Varma, P. B. Littlewood, S. Schmitt-Rink, E. Abrahams, and A. E. Ruckenstein. Phenomenology of the normal state of Cu-O high-temperature superconductors. *Phys. Rev. Lett.*, 63:1996, 1989.

C. M. Varma, P. B. Littlewood, S. Schmitt-Rink, E. Abrahams, and A. E. Ruckenstein. Erratum: Phenomenology of the normal state of Cu-O high-temperature superconductors. *Phys. Rev. Lett.*, 64:497, 1990.

A. H. Wilson. the theory of electronic semi-conductors. *Proc. Roy. Soc. A*, 133:458, 1931.

K. G. Wilson. The renormalization group: Critical phenomena and the kondo problem. *Rev. Mod. Phys.*, 47(4):773, 1975.

Junqiao Wu, Qian Gu, Beth S. Guiton, Nathalie P. de Leon, Lian Ouyang, and Hongkun Park. Strain-induced self organization of Metal-Insulator domains in single-crystalline VO_2 nanobeams. *NANO LETTERS*, 6:2313–2317, OCT 11 2006.

Kei Yosida and Kosaku Yamada. Perturbation Expansion for the Anderson Hamiltonian. *Prog. Theor. Phys. Supp.*, 46:244, 1970.

X. Y. Zhang, M. J. Rozenberg, and G. Kotliar. Mott transition in the d= ∞ Hubbard model at zero temperature. *Phys. Rev. Lett.*, 70(11):1666, 1993.

Publication

- *Micro domain formation near the first-order Mott-Hubbard metal-insulator transition*, Qinyong Liu and Johann Kroha, submitted to *Nature Materials*.

Acknowledgements

First I want to thank Prof. Kroha for his nice direction and discussion during my Ph.D. studies. Hundreds of times I was frustrated by the calculations in the domain wall problem. His encouragement helps me keep going until today. Second I want to thank Dr. Andreas Lubatsch. He gave me a lot help in writing this thesis. He looked through my thesis and gave me a lot suggestions: from the grammatical problem to the writing skills. I want to thank Katinka Ballmann, Mauricio Trujillo Martinez, Roman Katzer, Tobias Stollenwerk, and Zhongyuan Lai sincerely. They helped me to correct my thesis in details, from word to word. I also want to thank our cluster Administrator: Evaristus Fuh Chuo. This cluster really accelerates my calculation. My colleagues also gave me this family like environment and I really had a happy time during my Ph.D. studies. I want to give a special thank to my wife Xiaomeng. Without her understanding and supporting, I can not finish this work. I want also to thank my parents, because the love they gave me.